

**EXPLORING APPLICATION OF REMOTE
SENSING IN ESTIMATING CROP
EVAPOTRANSPIRATION:
Comparison of S-SEBI Algorithm and adapted FAO 56
Model using Landsat TM 5 and MODIS**

STEPHEN MAINA KIAMA
MARCH, 2008

Exploring Application of Remote Sensing in Estimating Crop Evapotranspiration: Comparison of S-SEBI Algorithm and Adapted FAO 56 Model using Landsat TM 5 and MODIS

by

Stephen Maina Kiama

Thesis submitted to the International Institute for Geo-information Science and Earth Observation in partial fulfilment of the requirements for the degree of Master of Science in Geo-information Science and Earth Observation, Specialisation: Planning and Coordination in Natural Resources Management

Thesis Assessment Board

Chairman

Prof. Dr. Ir. E. M. A. Smaling, NRS Department, ITC

External Examiner

Prof. Dr. H. Van Keulen, Wageningen University

Internal Examiner

Valentijn Venus (MSc.), NRS Department, ITC

Primary Supervisor

Dr. M. A. Sharifi, Associate Professor, ITC

Second Supervisor

Gabriel Norberto Parodi (MSc. Ir.), WREM Dept. ITC



**INTERNATIONAL INSTITUTE FOR GEO-INFORMATION SCIENCE AND EARTH
OBSERVATION
ENSCHEDE, THE NETHERLANDS**

DEDICATION

I dedicate this work:

To my mother Irene, for her unconditional sacrifice towards my studies;

To my wife Charity and son Wesley, from whom I find reasons for toiling; and

To James my brother.

Disclaimer

This document describes work undertaken as part of a programme of study at the International Institute for Geo-information Science and Earth Observation. All views and opinions expressed therein remain the sole responsibility of the author, and do not necessarily represent those of the institute

Abstract

Current Irrigation Advisory Services (IAS) are based on the FAO 56 methodology, relying on 'traditional' (non-remote-sensing) data sources. The main challenge is in obtaining accurate and up-to-date information on the spatial and temporal distribution of crop water requirement. Majority of existing remote sensing-based methods are very sophisticated, their implementation not directly matching the IAS operations. The aim of this study was to develop an operational method of estimating crop water use by integrating remotely sensed data into current operational advisory service procedure. In addition, the study aimed to evaluate the quality and success of spatial information enhancement obtained by disaggregation of derived MODIS evapotranspiration data. Series of MODIS data and two Landsat TM 5 of Roxo watershed in Alentejo region, Southern Portugal were processed together with soil and meteorological data. By application of three variants of reflectance-based approaches, NDVI-to-Kc models were formulated and respective crop coefficient (Kc) and crop evapotranspiration (ETc) estimated. 'Universal Triangle' model was employed to estimate evaporative fraction, in turn input into a statistical model to generate soil moisture availability maps. Soil moisture stress factor (Ks) was then evaluated taking into account the total available water (TAW) and depletion factor (ρ), both spatially mapped. For comparison purposes, S-SEBI algorithm and FAO 56 model were implemented to estimate ET. Disaggregation of selected outputs derived from MODIS data employed weighted ratio maps obtained from Landsat TM 5 data of 9th March 2007 (JD 68). Comparison of S-SEBI ET and net radiation against corresponding calculations based on in situ weather data yielded respectively low RMSE (1.32 mm/day) and moderate relative error (19 %). Compared to S-SEBI ET, 'traditional' FAO 56 model underestimated during initial and end phases and overestimated during mid phase. Estimates of the three variants deviated from S-SEBI ET estimates with varying degree. Of the three variants, Procedure 1 (based on phase-averaged S-SEBI Kc) seemed more reliable in tracking the dynamics of evapotranspiration. Procedure 1 (FAO 56 Kc-NDVI time series approach) was less reliable, but quite better than Procedure 2 (Per image NDVI-histogram approach). The quality of disaggregation procedure in terms of weighted ratio map was good. Increase of spatial variability was evident in all disaggregated MODIS products as measured by coefficient of variation. The study showed that the proposed scheme is not appropriate in condition with adequate moisture availability and should therefore not be judged on the basis of this pilot test. Rather, similar investigation is recommended in conditions occasioned by moisture stress and with careful choice of Kc. Further, accuracy of product derived from both low and high resolution satellite data is crucial in benefiting from disaggregation operation.

Key words: Irrigation Advisory Services; evapotranspiration; disaggregation; reflectance-based crop coefficients; soil moisture stress factor; FAO 56 model; S-SEBI algorithm; 'Universal Triangle' model.

Acknowledgements

Finalization of the MSc thesis is a milestone in my professional career and I thank Almighty God for that. I must acknowledge the support rendered to me towards this.

I would like in particular to thank the people and Government of The Netherlands, who made it possible for me to pursue higher education through the award of NUFFIC scholarship. I acknowledge the support of the Coordinator of Kenya Forests Working Group regarding the opportunity for further studies. Sincere gratitude is to the staff of ITC, from whom I have gained rich academic experience. Michael Weir, the Director of NRS Department was always keen to see the program running smoothly. My supervisors Dr. Ali Sharifi and Gabriel Parodi (MSc, Ir) were supportive and have induced new skills in me. It would have been difficult to continue was it not for the interest that Dr. Sharifi showed in this work. Further, Parodi tirelessly shared his technical knowledge which was very crucial. The insights from Dr. Luke Boerboom and Dick van der Zee were instrumental in motivating the study.

I thank the Director and staff of Centro Operative de Technological de Regadio (COTR), Beja City, Portugal, for their support during my field work in September 2007. The information and data I obtained from them constituted primary input into this study. I acknowledge the support from my colleagues in the field including Dr. Maciek, Parodi, Alain GB and Tanvir who were very collaborative. I gained a lot of experience from them.

I appreciated the academic exchanges I had with my colleagues during taught modules and thesis phase. The discussions especially with Wilber and Harvei were very beneficial. My colleagues in Planning and Coordination made the experience in that specialization insightful and enjoyable. Many thanks are to Edward, Seta, Kwasi, Elifas, Ine, Tarun, Sarah, Maureen, Marion, Margaret and Poling. I also acknowledge the academic interaction with Manyenye, Miza, Madyaka, Jennifer Kinoti and Msana.

I thank the ITC Library staff especially Carla and Petry for their assistance in availing literature whenever I made request. Mr. Reink was supportive in acquisition of remote sensing data and I appreciate his help. I also acknowledge the support of Bettine Geerdink of the student Affairs Desk. The staff of ITC Dish Hotel made my stay in Enschede hospitable and I appreciate their effort. ITC Christian Fellowship was a home away from home and I appreciate the support of the patrons, including Jan Vervoot, Dr. Paul, Rev. Josine and Winnie Krens. I also appreciate the effort of ITC Kenyan community in organising social gatherings that made it possible to overcome loneliness.

Without undue emphasis, I acknowledge the support and encouragement from my family members back in Kenya. The initial inspiration from my mother and the support from my sisters and brothers gave me momentum to continue my studies and I thank them for that. Most of all, I thank my wife Charity and son Wesley for remaining steadfast, for their prayers and for bearing my long absence. Her special emotional support was most appreciated. To them all, I pray for God's blessings.

Table of contents

1.	Introduction	1
1.1.	Water Use in Agriculture	1
1.2.	Methods of determining crop and irrigation water requirement	1
1.2.1.	Application of remote sensing in crop and irrigation water management.....	2
1.3.	Research Problem	3
1.4.	Research Objectives.....	4
1.5.	Research Hypotheses	4
1.6.	Research Questions	4
1.7.	Research Approach	4
1.8.	Structure of the Thesis	5
2.	Definition of terminologies and Review of existing remote sensing-based ET estimation methods	6
2.1.	Definition of Terminologies	6
2.2.	Remote sensing-based methods of estimating Evapotranspiration	7
2.3.	Dissaggregation.....	9
3.	Study area and Data Description	10
3.1.	Description of the Study Area.....	10
3.1.1.	Physiography and hydrography.....	10
3.1.2.	Climate	10
3.1.3.	Soils.....	12
3.1.4.	Landuse and irrigation.....	12
3.2.	Description of soil related data	12
3.2.1.	Soil water holding characteristics	12
3.2.2.	Secondary soil moisture data.....	12
3.3.	Description of Meteorological Data.....	12
3.4.	Description of Remote Sensing Data.....	13
4.	Estimation of Crop Evapotranspiration (ET _c) based on Traditional FAO 56 Procedure.....	14
4.1.	Introduction.....	14
4.2.	Implementation of ‘Traditional’ FAO 56-based model	14
4.2.1.	Estimation of reference ET for selected days of interest (DOI).....	14
4.2.2.	Crop coefficient curve	15
4.2.3.	Estimation of Crop Evapotranspiration (ET _c).....	16
4.2.4.	Assessment of the results of ‘Traditional’ FAO-56 approach.....	16
5.	Estimation of Evapotranspiration using Simplified Surface Energy Balance Index (S-SEBI)	18
5.1.	Introduction.....	18
5.2.	Model Implementation	20
5.2.1.	Pre-processing of Remote Sensing data	21
5.2.2.	Processing of MODIS NDVI and MSAVI.....	23
5.2.3.	Processing Landsat TM 5 NDVI and MSAVI	23
5.2.4.	Computing Input Parameters.....	24
5.3.	Evaporative fraction.....	24
5.4.	Daily Evapotranspiration	25
5.5.	S-SEBI-based K _c	25

5.6.	Dissaggregation of S-SEBI ET data based on weighted ratio.....	25
5.7.	Assessment of selected S-SEBI outputs.....	25
5.7.2.	Evaluation of dissaggregation procedure based on S-SEBI ET	40
6.	Proposed Method of integrating remote sensing in Estimation of Reflectance-based Crop Coefficients and Soil Moisture Stress factor in Mapping Crop Evapotranspiration	42
6.1.	Introduction.....	42
6.2.	Spatial and temporal characterization of NDVI in selected wheat area.....	43
6.3.	Relationship between crop coefficient (Kc) and NDVI.....	44
6.3.1.	FAO-56 Kc-NDVI time series modelling approach.....	44
6.3.2.	Per-image NDVI-histogram-FAO Kc modeling approach.....	45
6.3.3.	Relationship of NDVI and S-SEBI-based crop coefficient.....	47
6.4.	Estimation of NDVI-based Kcr and crop evapotranspiration (ETc).....	48
6.4.1.	Kcr and ETc estimates based on application of FAO 56 Kc-NDVI time series approach	48
6.4.2.	Kcr and ETc estimates based on application of per-image NDVI-histogram approach	49
6.4.3.	Kcr and ETc estimates based on application of S-SEBI Kc-NDVI model.....	50
6.5.	Comparison of Kcr and ETc estimates from the three procedures	51
6.6.	Remote sensing-based estimation of soil moisture stress factor (Ks).....	52
6.6.1.	Theoretical basis of estimation of Ks	52
6.6.2.	Implementation of the Ks estimation scheme	56
6.7.	Dissaggregation of selected products of proposed method using weighted ratio approach.	59
6.7.1.	Comparison of ETc estimates derived from (aggregated) Landsat TM 5 with corresponding estimate from MODIS	59
6.7.2.	Evaluation of weighted ratio derived from Landsat TM estimates of reflectance-based ETc (FAO 56-Kc-NDVI time series procedure), JD 68.....	59
6.7.3.	Dissaggregation of original MODIS estimates of ETc and evaluation of spatial variability enhancement	60
7.	Cross Analysis of the ET estimates of the different approaches	61
8.	DISCUSSION	64
8.1.	Performance of ‘traditional’ FAO 56 Approach and S-SEBI algorithm vis-à-vis the Proposed Method in estimation of Evapotranspiration	64
8.2.	Evaluation of weighted ratio approach in dissaggregation of MODIS ET data and enhancement of spatial variability.....	69
9.	CONCLUSIONS AND RECOMMEDATIONS.....	71
9.1.	Conclusions.....	71
9.2.	Recommendations.....	72
10.	References	74
11.	Appendices	79

List of figures

Figure 1: Flowchart of proposed research approach	5
Figure 2: Location of the study area	11
Figure 3: Location of the three meteorological stations (Background map adapted from COTR SAGRA.NET WEBSITE)	13
Figure 4: Wheat area delineated for analysis of ET. The background is Aster image of June 2, 2007.	14
Figure 5: Generalized crop coefficient curve, Adapted from [9].....	16
Figure 6: Profile of ETo and ETc based on FAO 56 Kc (tabulated) along the winter wheat growth period (Oct 2006-Aug. 2007), Pisos, Portugal.	17
Figure 7: Schematic representation of the relationship between surface reflectance and temperature together with the basic principles of S-SEBI (Adapted from [22])	19
Figure 8: Flowchart of implementing S-SEBI algorithm to obtain evapotranspiration from MODIS and Landsat TM.....	21
Figure 9: Selected zones over the Pisos & Roxo study block to analyze spatial distribution and temporal evolution of evapotranspiration data from October 2006 to September 2007.....	26
Figure 10: Landsat TM estimate of net radiation, JD 244	26
Figure 11: Temporal variation of net radiation in Pisos and Roxo area, (Oct. 2006-Sep. 2007).....	27
Figure 12: Landsat TM estimate of daily evapotranspiration map, JD 244	27
Figure 13: Mean Temporal variation S-SEBI ET and standard deviation and Penman-Monteith for the whole study block, (Oct 2006-Sept. 2007).	28
Figure 14: Temporal variation of daily evapotranspiration in Pisos and Roxo area, (Oct. 2006-Sep. 2007).	28
Figure 15: Correlation between NDVI and S-SEBI ET in winter wheat area in Pisos between October 2006-September 2007.....	29
Figure 16: Relationship between S-SEBI ET and NDVI in wheat field in Pisos (early May to Late July 2007).....	30
Figure 17: Relationship between S-SEBI ET and NDVI in maize field in Pisos (early May to Late July 2007).....	31
Figure 18: Relationship between S-SEBI ET and soil moisture (surface layer: 0-10 cm) in maize field in Pisos (mid April to Late July 2007).....	31
Figure 19: Relationship between S-SEBI ET and soil moisture (depth-averaged: 0-70 cm) in maize field in Pisos (mid April to Late July 2007).....	32
Figure 20: Calculated ratio (Cdi) between daily net radiation (Rnd) and instantaneous (Rni) net radiation (Cdi= Rnd / Rni) versus the day of the year. The calculation was based on sinusoidal equation derived by [61] based on net radiation fluxes measured in a met ...	33
Figure 21: Correlation between S-SEBI instantaneous net radiation estimates against estimates based weather station measurements (COTR near Beja City) between October 2006-September 2007.....	33
Figure 22: Comparison between S-SEBI instantaneous net radiation estimates against estimates based weather station measurements (COTR near Beja City) between October 2006-September 2007.....	34

Figure 23: Comparison of S-SEBI ET estimates (in Roxo Dam) with meteorological estimates of simulated PAN ET.....	34
Figure 24: Landsat TM estimate of S-SEBI Kc, JD 244	35
Figure 25: Profile of S-SEBI Kc in Pisos and Roxo area, (Oct. 2006-Sep. 2007).....	36
Figure 26: Comparison of profiles of S-SEBI Kc and NDVI in wheat area in Pisos, (Oct. 2006- Sep. 2007).	36
Figure 27: Relationship between S-SEBI Kc and NDVI in maize field, Pisos (early May to late July 2007)	37
Figure 28: Relationship between S-SEBI Kc and NDVI in beterraba field, Pisos (early May to late July 2007).....	37
Figure 29: Relationship between S-SEBI Kc and soil moisture (surface layer: 0-10 cm) in maize field, Pisos, (mid April to late July 2007).	37
Figure 30: Temporal profile of Penman-Monteith ETo and S-SEBI ET (and associated standard deviation) in selected wheat field, Pisos, (October 2006- September 2007).	38
Figure 31: Temporal profile of S-SEBI Kc and associated spatial variation (CV) for selected wheat area, Pisos, (Oct. 2006-Sep. 2007).	39
Figure 32: Temporal variation of phase-averaged S-SEBI Kc of winter wheat in Pisos, (October 2006-late July 2007)	39
Figure 33: Temporal profile of ETc estimated based phase-averaged S-SEBI Kc applied into FAO 56 approach for winter wheat in Pisos, (October 2006-September 2007).	40
Figure 34: Flowchart of proposed scheme to obtain actual evapotranspiration	42
Figure 35: Temporal variation of NDVI for selected wheat area, Pisos, (Oct. 2006-Sep. 2007).....	43
Figure 36: Within-phase averaged NDVI values for selected winter wheat area in Pisos....	44
Figure 37: FAO 56 Kc-NDVI relationships based on NDVI time series approach.....	45
Figure 38: Histogram of NDVI values for a segment of the PVID showing crop coefficient labels at initial value and crop peak, based on 1988 data, (Adapted from [18]).....	46
Figure 39: FAO 56 Kc-NDVI relationships based on per image histogram approach	46
Figure 40: Relationship between S-SEBI Kc and NDVI in selected wheat area , Pisos (early May to late July 2007).....	47
Figure 41: Kcr based on FAO 56-NDVI time series: MODIS, JD 184	48
Figure 42: ETc based on FAO 56-NDVI time series: MODIS, JD 184.....	48
Figure 43: Kcr based on Per-image approach: MODIS, Kcr, JD 68.....	49
Figure 44: ETc based on Per-image approach: MODIS, ETc, JD 68.....	49
Figure 45: Kcr based on S-SEBI Kc-NDVI model: MODIS, JD 184	50
Figure 46: ETc based on S-SEBI Kc-NDVI model: MODIS, JD 184	50
Figure 47: Comparison of Kcr estimates obtained from the three variants of reflectance-based approach.	51
Figure 48: Comparison of ETc estimates obtained from the three variants of reflectance-based approach.	52
Figure 49: Universal Triangle relationship between soil moisture, temperature and NDVI, source[38].	53
Figure 50: Maps of Evaporative Fraction, estimated using Universal Triangle model (equation 27 and Table 16).....	56
Figure 51: Comparison of EF estimated by 'Universal Triangle' model against estimates of S-SEBI model.....	56

Figure 52: Depth-averaged soil moisture (mm/cm^3), MODIS, JD184 57

Figure 53: Comparison of depth-averaged soil moisture estimated by ‘Universal Triangle’ model against ground-based measurements 57

Figure 54: Actual ET based on FAO 56 Kc-NDVI time series: MODIS, JD68 59

Figure 55: Profiles of S-SEBI ET, crop evapotranspiration (ET_c) estimated using FAO 56 Kc and phase-averaged S-SEBI Kc and Penman-Monteith ET_o , (Oct. 2006-Sep. 2007). P1, P2 and P3 are respectively FAO 56 Kc-NDVI time series approach, per image NDVI histogram approach and S-SEBI Kc-NDVI model. 61

Figure 56: Comparison of crop ET_c estimated by the approaches investigated. P1, 2 and 3 refer to respectively FAO 56 Kc-NDVI time series approach, per image NDVI histogram approach and S-SEBI Kc-NDVI model..... 62

Figure 57: Comparison of crop coefficient employed/ obtained by the ET estimation approaches investigated. P 1, 2 and 3 refer to respectively FAO 56 Kc-NDVI time series approach, per image NDVI histogram approach and S-SEBI Kc-NDVI model..... 63

List of tables

Table 1: Lists of climatic variables employed in this study and the source station	13
Table 2: Comparison of emissivity range used in the study against the range reviewed in literature.	22
Table 3: Landsat Thematic Mapper band specific constants ([22] and [45]).....	22
Table 4: Summary data of atmospheric condition for the two days during Landsat TM overpass.....	23
Table 5: Analysis of spatial variability of S-SEBI ET estimates for original and disaggregated MODIS.....	41
Table 6: Regression coefficients a and b of per-image FAO-56 Kc-NDVI relationship	46
Table 7: Summary statistics and spatial variability in reflectance-based crop coefficient (Kcr) in selected wheat field (based on FAO-56 Kc –NDVI time series approach).....	48
Table 8: Summary statistics and spatial variability in ETc in selected wheat field (based on FAO-56 Kc –NDVI time series approach).....	49
Table 9: Summary statistics and spatial variability in reflectance-based crop coefficient (Kcr) in selected wheat field (based on per-image NDVI-Histogram approach).....	49
Table 10: Summary statistics and spatial variability ETc in selected wheat field (based on per-image Histogram approach).....	50
Table 11: Summary statistics and spatial variability in reflectance-based crop coefficient (Kcr) in selected wheat field (based on S-SEBI Kc-NDVI model).....	50
Table 12: Summary statistics and spatial variability in crop ETc in selected wheat field (based on S-SEBI Kc-NDVI model)	51
Table 13: Coefficients of the polynomial relationship for EF between T* and Fr as specified in equation 27	54
Table 14: Analysis of spatial variability of ETc estimates (based on FAO 56 Kc-NDVI time series) for both original and disaggregated MODIS.....	60

1. Introduction

1.1. Water Use in Agriculture

Improving water use efficiency is a primary challenge that many countries are trying to address. It is acknowledged that water resources are becoming constrained to meet the growing demand, especially food production. The growing world human and livestock population puts a direct demand on agriculture to supply food, fiber and fodder, implying consumption of huge volume of water to meet this demand.

While rain-fed agriculture continues to be an important contributor to food demand, irrigation is commanding a substantial share, (Bastiaanssen 2000). It is projected that for the world to feed itself in 2025, 17% more irrigation water will be needed (Bastiaanssen, Molden et al. 2000; English 2002).

In arid and semi-arid regions, surface and groundwater resources are naturally limited, and the challenge to produce more food under increasing water scarcity is real, (Bouman 2007). For instance, Alentejo region, Portugal, with Mediterranean and continental climate, has long and dry summers, and agriculture is primarily irrigation dependent. Management of crop water use is therefore a real concern.

Crop water management requires accurate scheduling of irrigation (Bausch 1995). Optimum irrigation strategies can be identified by use of detailed models relating applied water, crop production, and irrigation efficiency (English 2002). In this context, relationship between estimated crop yield and hydrological parameters (Bastiaanssen and Ali 2003) should be assessed to enable management to predict the resulting water productivity of a given irrigation intervention,(Lorite).

Several indicators have proved successful in assessing water use efficiency in crop production. Crop water requirement (CWR) is the amount of water that need to be supplied to compensate evapotranspiration,(Allen and Fao 1998). In standard condition, potential evapotranspiration (ET_c) correspond to CWR, (Allen and Fao 1998; Bochenek 2007). In case of water stress, actual evapotranspiration is below ET_c . Time series of actual evapotranspiration are successfully being used to indicate crop water consumption (Akbari 2007). Irrigation water requirement represent the difference between the CWR and effective precipitation(Allen and Fao 1998). Crop water productivity is important in evaluating good management practices,(Zwart and Bastiaanssen 2004; Zwart and Bastiaanssen 2007).

Estimation of these indicators requires methods that can yield reliable results and yet be feasible to implement practically to support crop water management. Several methods exist but differ in their operational limitation.

1.2. Methods of determining crop and irrigation water requirement

Traditional method for managing water use efficiency used by majority of Irrigation Advisory Services (IAS) is based on crop coefficient approach (Allen 2000). This requires the determination of reference evaporation (ET_0) from IAS meteorological stations and crop

coefficient (k_c) (Allen 2000) from the look-up table. Potential evapotranspiration is then determined as a product of the ET_0 and k_c . Irrigation water requirement is derived by subtracting potential evapotranspiration from precipitation.

Point data k_c from reference table assumes homogeneity over the respective area and may contribute to error in estimating crop water requirement due to their empirical nature, (Ray and Dadhwal 2001). In view of this limitation, new techniques for estimating actual evaporation and transpiration have been developed that would potentially contribute to spatial and temporal information needed for crop water management. In their review, (Kite and Droogers 2000) has categorized these techniques into field-based, hydrological models and remote sensing methods, each fit for different circumstances.

1.2.1. Application of remote sensing in crop and irrigation water management

Remote sensing allows for independent observation of actual situation and easy access to information on spatial variability of vegetation (de Wit and Boogaard 2001), (Wesseling and Feddes 2006) and (Seevers 1994). The basis of its application in quantifying spatio-temporal variation in water use is in its ability to discriminate land features and also variations in important crop parameters such as evapotranspiration (Bandara, Bos et al. 2006) and crop coefficients.

Although many research have demonstrated potential application of remote sensing in enhancing efficient water use in irrigated agriculture, it has unfortunately remained mainly a research tool (Bastiaanssen, Molden et al. 2000), and has not been widely used operationally to support Irrigation Advisory Services as would have been envisaged.

According to (Calera 2003), remote sensing products that are developed do not match the need of IAS. Also, aspects of adequacy and easy-to-use information by the farmers have limited the propagation of these techniques. Ideally, integration of remote sensing in their operation would greatly enhance the performance of advisory service, but achieving this goal warrant keen focus on suitability of methods to the circumstances of IAS.

Existing methods applied to derive parameters and performance indicators from spectral reflectance measurements vary in data requirements, ease or constraints related to their use, (Kite and Droogers 2000). Advanced remote sensing flux algorithms developed over the last few decades to estimate actual crop evapotranspiration differ in the procedure employed to resolve the energy balance equation; some calculate the sensible heat flux first and then obtain the latent heat flux as the residual of energy balance equation while others estimate the relative evaporation by means of an index using a combination equation. They include Surface Energy Balance Algorithm for Land (SEBAL), Crop Water Stress Index, Surface Energy Balance Index (SEBI), Surface Energy Balance System (SEBS) (Su 2003), Simplified Surface Energy Balance Index (S-SEBI), (Roerink, Su et al. 2000), and have been tested successfully.

Besides the flux algorithms, canopy reflectance-based approach has proved to be rather simple and straightforward technique in estimation of evapotranspiration. It has great feasibility for practical application beside research, and its potentials should be explored further, (Jayanthi, Neale et al. 2007).

In (Martin de Santa Olalla, Calera et al. 2003), Normalized Difference Vegetation Index (NDVI) was related with water status in semi-arid conditions. It was observed that a large supply of water in these conditions entails a better growth of the actual crop resulting in a greater degree of land cover correlating with higher NDVI.

Spatially distributed crop coefficient can be derived by developing and applying a linear relationship with NDVI. In (Rossi 2007), reflectance-based coefficients (k_{cr}) was derived by relating maximum and minimum values of Terra /Moderate Resolution Imaging Spectroradiometer (Terra /MODIS) NDVI time series with the FAO tabulated K_c . The k_{cr} maps were finally combined with reference evapotranspiration (ET_0) to compute potential crop evapotranspiration.

In (Bausch 1993) and (Bausch 1995) soil adjusted vegetation index (SAVI) was used to evaluate the performance of canopy reflectance-based crop coefficient as an effective indicator for irrigation scheduling for corn. A linear transformation between basal crop coefficient (k_{cb}) and the SAVI was used to convert SAVI into crop coefficient (k_{cr}). In (Ray and Dadhwal 2001) SAVI derived from multi-date remote sensing data was used to spatio-temporally extrapolate (point-data) crop coefficient (k_{cr}).

As noted from the foregoing, existing canopy reflectance-based crop coefficient methods offer exciting opportunities for IAS to incorporate remote sensing into their day-to-day operations. In their review, (Moran, Inoue et al. 1997) concluded that this approach is one of the most promising for operational application as it requires minimum adjustment of the current operating procedures of IAS. These methods have yielded satisfactory results when applied to medium and high spatial resolution satellite imageries. In view of availability of public domain remote sensing data, then IAS can benefit from them using these canopy reflectance-based crop coefficient methods.

Some aspects of these methods, however, still can be improved. There is the need to account for the differential spectral reflectance between wet and dry soil, a limitation of canopy reflectance-based crop coefficient method cited by (Choudhury 1994). Another challenge relate to the assumption by the method, of standard condition when deriving evapotranspiration rates. Sub-optimal field conditions may, however, be the reality. According to (Scott, Bastiaanssen et al. 2003), difference between potential and actual evapotranspiration is caused by soil moisture stress. As soil water content in root zone progressively drops below a certain threshold, evapotranspiration begins to decrease in proportion to the amount of water remaining in the root zone, (Allen and Fao 1998). The other challenge relates to resolution of the available remote sensing data. High temporal resolution sensors have coarse spatial resolution that does not fit the application of field level irrigation scheduling.

1.3. Research Problem

Improved operational and low cost methods will enable IAS to cost-effectively monitor crop and irrigation water requirement of each field in extended areas. Practical application of remote sensing to estimate and assess irrigation performance indicators is coupled with methodological challenges in terms of their operability and reliability. Most methods and algorithms developed are computationally complicated and expensive to make them operational.

Existing canopy reflectance-based crop coefficient methods have proved successful in estimating crop water use for several crops (Jayanthi, Neale et al. 2007). They are one of the most promising ways for operational application (Belmonte, Jochum et al. 2003). While using these methods, up-to-date monitoring of spatially distributed actual crop coefficient (k_c) and actual crop evapotranspiration for irrigation scheduling can potentially be improved by accounting for soil moisture availability and disaggregation of low spatial but high temporal resolution remote sensing evapotranspiration (ET) data.

Whereas vegetation indices have adequately been applied to distribute and obtain reflectance-based crop coefficients, incorporation of soil moisture availability function modelled spatially using remotely sensed data in evaluating actual crop evapotranspiration has not been tested and the reliability of final actual ET derived in this manner not proved. Similarly, regarding disaggregation of MODIS ET data based on weighted ratio approach, the quality and success of spatial information enhancement has not been evaluated for ET data derived from either S-SEBI algorithm or reflectance-based crop coefficient scheme.

1.4. Research Objectives

The overall objective of the study was to formulate a remote sensing-based method of estimating actual evapotranspiration that is operational and requiring minimal adjustment of the current operational procedure of irrigational advisory services (IAS). In addition, the study aimed to evaluate the quality and success of spatial information enhancement potentially rendered by disaggregation of derived MODIS ET data based on weighted approach.

Specific objectives were:

1. To understand existing remote sensing-based methods and how they can be used to estimate crop and irrigation water requirement.
2. To develop an operational method to estimate actual evapotranspiration.
3. To implement and evaluate the method.
4. To evaluate the practical performance of the method.
5. To evaluate the reliability of the estimates obtained from the method against corresponding estimates derived from surface energy balance approach.

1.5. Research Hypotheses

The study formulated and tested these hypotheses:

1. The proposed method where soil moisture availability function modelled spatially using remotely sensed data would allow the estimation of spatially distributed actual crop evapotranspiration comparable to that derived from energy balance approaches.
2. Weighed ratio-based disaggregation procedure applied to derived MODIS ET data and using corresponding ratio maps obtained from Landsat TM 5, is of good quality and yield increased spatial information.

1.6. Research Questions

In line with the objectives, the research questions investigated were:

1. What are the existing remote sensing-based methods of estimating actual evapotranspiration?
2. How can an operational method of estimating actual evapotranspiration be developed?
3. What would be the results of the operational method and its practical performance?
4. How reliable are the estimates derived from the operational method relative to estimates derived from energy balance approaches?

1.7. Research Approach

The approach followed in this study is shown in Fig. 1. Crop evapotranspiration (ET) was estimated based on three approaches respectively: traditional FAO 56 approach (Process 1);

Simplified Surface Energy Balance Index (the selected energy balance algorithm as the standard) (Process 2); and the proposed scheme (Process 3). The results of each process were analysed separately followed by cross analysis that involved comparison of obtained outputs. Conclusions were drawn on the basis of these analyses.

1.8. Structure of the Thesis

The remainder of the thesis is organized in further chapters:

Chapter 2 presents definitions of terminologies and review of existing remote sensing-based ET estimation methods.

Chapter 3 describes the study area, the input data used and exploratory analysis considered.

Chapter 4 describes the traditional FAO-56 based approach.

Chapter 5 presents implementation of S-SEBI approach and evaluation of disaggregation procedure of S-SEBI ET.

Chapter 6 describes the proposed scheme and evaluation of disaggregation procedure of some selected outputs.

Chapter 7 presents cross analysis of evapotranspiration estimates from investigated approaches.

Chapter 8 presents discussion of the whole study

Chapter 9 presents conclusions and recommendations drawn from the study.

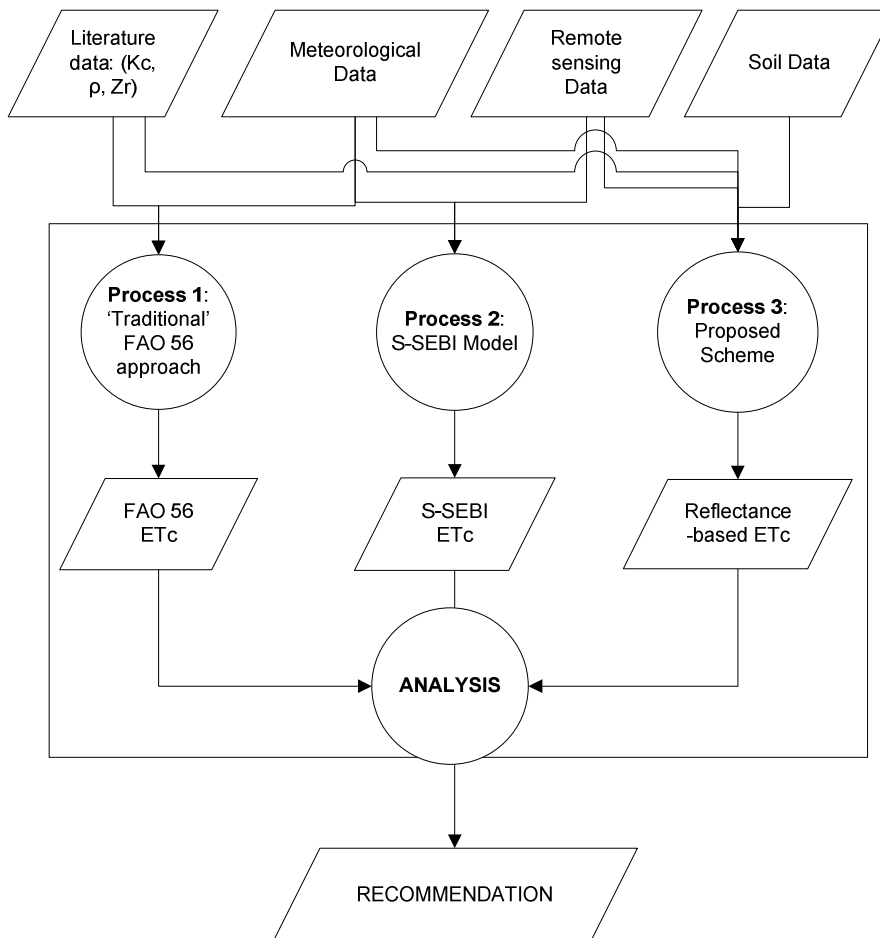


Figure 1: Flowchart of proposed research approach

2. Definition of terminologies and Review of existing remote sensing-based ET estimation methods

2.1. Definition of Terminologies

Evapotranspiration process

Evapotranspiration is a key factor for determining proper irrigation scheduling and for improving water use efficiency in irrigated agriculture, (Er-Raki 2007). It combines two separate processes: evaporation and transpiration, (Allen and Fao 1998). Both of these processes entails vaporization which in turn requires energy provided by direct solar radiation and partially by ambient temperature of air. According to (Stisen), the rate of evapotranspiration is mainly controlled by the available energy, the availability of water, the humidity gradient away from the surface and the wind speed at the surface. In general, weather parameters, crop characteristics, management and environmental aspects are factors affecting evapotranspiration, (Allen and Fao 1998).

Reference crop evapotranspiration (ET_o)

ET_o is a climatic parameter expressing the evaporation power of the atmosphere. The reference surface is a hypothetical grass reference crop with specific characteristics. According to (Allen and Fao 1998; Beyazgul, Kayam et al. 2000), ET_o is defined as “the rate of evapotranspiration from an extensive surface of 5-15 cm tall, green grass cover of uniform height, actively growing, completely shading the ground and not short of water”. It allows study of evaporative demand of the atmosphere independent of crop type, crop development and management practices.

There are several methods for computing ET_o and in their intercomparison study on evapotranspiration, (Beyazgul, Kayam et al. 2000) applied six methods of estimating ET_o on a cotton field. This and other studies have proven a global validity of the FAO Penman-Monteith method for predicting the ET_o. The method is elaborated in (Allen and Fao 1998).

Crop evapotranspiration (ET_c)

ET_c is “ the rate of evapotranspiration from a disease-free crop, growing in large fields under non-restricting soil water and fertility conditions and achieving full production potential under the given growing environment”, (Beyazgul, Kayam et al. 2000). In such conditions, the water required to compensate the evapotranspiration loss from the cropped field is defined as crop water requirement, referring to amount of water that needs to be supplied.

Crop coefficients

Crop coefficients (K_c) are ratios determined experimentally between E_t and ET_o. Application of crop coefficients follows two approaches; single and dual crop coefficients. In the single approach, the effect of crop transpiration and soil evaporation are combined into a single K_c. The dual approach consists of two coefficients: a basal crop coefficient (k_{cb}) and a soil evaporation coefficient (k_e). The latter approach is mainly used in research and real-time irrigation scheduling for high frequency water application,(Allen and Fao 1998) and (Er-Raki 2007).

2.2. Remote sensing-based methods of estimating Evapotranspiration

Evapotranspiration varies in time and space and is difficult to estimate as it depends on many interacting variables (Stisen). Most conventional techniques which use discrete point measurements to estimate the evaporative flux, LE, are only representative of local areas, including Bowen ratio, eddy correlation, soil water balance among others. They cannot be extended to large areas because of the dynamic nature and regional variation of LE (Li and Lyons 2002).

For operational purposes, the method recommended by FAO (FAO 56 method) is used in many countries. It consists of estimating the crop evapotranspiration (ET_c) for a crop canopy using reference evapotranspiration (ET_o) and crop coefficient (K_c). According to (Courault, Seguin et al. 2003), the crop type, variety and development stage should be considered when assessing evapotranspiration from crops. Differences in resistance to transpiration, crop height, ground cover, roots among other factors result in different ET levels.

Quantification of evapotranspiration over large areas is operational and cost-effective with the incorporation of Earth Observation techniques (Belmonte, Jochum et al. 2003). Remote sensing has proven to be the only suitable approach for large-area estimates of LE because satellite remote sensing is the only technology that can provide representative parameters such as radiometric surface temperature, albedo and vegetation index in a globally consistent and economically feasible manner (Li and Lyons 2002), (Seevers 1994) and (Stisen).

Several schemes estimating evapotranspiration based on remote sensing data have been developed and can be put into three categorizations by (Courault, Seguin et al. 2003): empirical, residual methods of energy balance, and indirect methods.

Empirical methods allow the characterization of crop water use both at local scale from ground measurements and at the scale of large irrigation areas from satellite data using cumulative temperature difference. The application of empirical relationships requires two variables, for instance the minimum air temperature and the daily net radiation. The latter can be obtained from remote sensing data. However, the problem of spatial representativity of the air temperature is more debatable and particularly acute for regional studies (Courault, Seguin et al. 2003).

An approach based on empirical relation between sensible heat flux and surface-air temperature difference was also proposed by (Dunkel and Grob-Szenyan 2002). Similarly, other authors have explored simple remote sensing methods, not dependent on ancillary data, is the contextual spatial information based on the surface temperature-vegetation index space ($T_s - NDVI$). This method, known as "the triangle" method, has been applied successfully in certain applications for estimation of both evapotranspiration and soil moisture (Gillies, Kustas et al. 1997), (Wang 2007), (Jiang and Islam 2001) and (Carlson 2007). The rationale is that the amount of vegetation cover affects transpiration. Vegetation indices like NDVI are also related to surface temperature, i.e. more evapotranspiration tends to be associated with lower temperature. A trapezoid scheme (or a triangular shape) appears in which the different soil moisture conditions can be classified, (see Fig.50).

Definition of reflectance-based crop coefficients is based on similar principles. Relational models are developed by relating vegetation indices and observed crop-soil parameters from selected training pixels. The model is then applied to remote sensing images to determine the spatial conditions of the crops in the region, (Doraiswamy, Hatfield et al. 2004).

In (Courault, Seguin et al. 2003), residual methods are described as combining empirical relationships and physical components. According to (Stisen), the residual methods utilize remote sensing data in combination with ancillary data to estimate sensible heat flux H and through that evapotranspiration. These methods vary in complexity, but usually estimate surface resistances from radiometric surface temperatures. Within this class some most current methods (SEBAL, S-SEBI) use remote sensing data directly to estimate input parameters and ET. Some methods calculate the sensible heat flux first and then obtain the latent heat flux as the residual of energy balance equation, (SEBAL); other methods estimate the relative evaporation by means of an index using a combination equation, (SEBI, S-SEBI).

Methods in former group compute the sensible heat flux (H), defined as a function of temperature gradient and aerodynamic resistance,(Bastiaanssen 1998). In Surface Energy Balance Algorithm for Land (SEBAL), H is computed from flux inversion at dry non-evaporating land units and at wet surfaces types,(Bastiaanssen 1998). SEBAL utilizes semi-empirical relationships and simplifications of the energy balance formulation over dry and wet areas to accomplish 25 computation steps. It is designed to calculate the energy partitioning at the regional scale with minimum ground data,(Courault, Seguin et al. 2003). Atmospheric variables (air temperature and wind speed) are estimated from remote sensing data, considering the spatial variability induced by hydrological and energetic contrasts. The determination of wet and dry surfaces on the studied area is necessary to extract threshold values. Key input data are spectral radiances in the visible, near infrared and thermal infrared of the spectrum. Maps of incoming radiation, surface temperature, NDVI and albedo are required. Semi-empirical relationships are used to estimate emissivity, roughness length and soil heat flux from NDVI. In addition, the algorithm requires instantaneous and daily averaged weather data on wind speed, relative humidity, solar radiation and air temperature near the Earth surface. It finally estimates on pixel-basis, the spatial variation of actual ET rates as well as other surface exchanges between land and atmosphere as the residual of energy balance.

The second group of residual method is also based on the contrast between wet and dry areas. According to (Courault, Seguin et al. 2003),the earlier model Surface Energy Balance Index (SEBI) determines evapotranspiration from evaporative fraction. The concept is included in the more complex framework, Surface Energy Balance System (SEBS) that allows the determination of the evaporative fraction by computing the energy balance in limiting cases. Simplified Energy Balance Index (S-SEBI) is a simplified method derived from SEBI,(Roerink, Su et al. 2000). It estimates surface flux from remote sensing data. It determines a reflectance dependant maximum temperature for dry condition and reflectance dependant minimum temperature for wet conditions. The major advantage is that no additional meteorological data is needed if the surface extremes are present on the images studied. Further, in the model implementation, the extreme temperatures for the wet and dry conditions vary with changing reflectance values, in contrast to other methods that try to determine a fixed temperature for wet and dry conditions for the whole image and /or for each land use class. The model is only feasible in cases where the atmospheric conditions are constant over the image and sufficient wet and dry pixels are present throughout the reflectance spectrum. Otherwise when these terms are not met, the complete SEBI version has to be used,(Roerink, Su et al. 2000).

Other methods avoid the difficult of obtaining meteorological variables on large areas by integrating planetary boundary layer models to simulate the evolution of the parameters like air temperature, wind speed among other variables,(Courault, Seguin et al. 2003). Radiosoundings are then necessary to initialize the atmosphere. Accuracy of these methods is difficult to estimate.

Indirect methods generally use complex models (usually deterministic SVAT models) simulating the different terms of the energy budget, (Courault, Seguin et al. 2003). Remote sensing data can be incorporated at different levels, in the input parameters to characterize the surface and/or using assimilation procedure to get more adequate parameters to compute ET. Advantage of these indirect methods is that they allow getting intermediate variables linked to the crop development (like Leaf Area Index, LAI) or the soil water status. According to (Stisen), these methods are still dependant on key parameters like wind speed and air temperature which usually are not available on a regional scale or from remote sensing data.

2.3. Dissaggregation

The spatial resolution of the ET data obtained from Terra MODIS data is low and limits their application in spite of the adequate temporal resolution. According to (Hong, Hendrickx et al. 2005), scaling transfer means changing data or information from one scale to another. Upscaling consists of taking information at smaller scales to derive processes at larger scales, while downscaling consists of decomposing information at one scale into its constituents at smaller scales.

Several approaches have been formulated to effect scale transfer. In (Hong, Hendrickx et al. 2005), scaling transfer procedure have been experimented, both upscaling and downscaling. The procedure is based on resampling process, breaking pixels into high resolution components. The averaging process (aggregation) includes calculating arithmetic and geometric means.

Linear mixing approaches ((Vazifedoust 2007)) assumes that each image pixel contains information about the proportion and the response of each component. Thus, the responses of each pixel are considered as a linear combination of the responses of all components in the mixed target.

In weighted ratio-based approaches ((Chemin 2004) and (Vazifedoust 2007)), a detailed ET^{HIGH} data map from higher spatial resolution satellite image is used as a weight to spatially redistribute the $ET_s(t)$ calculated from coarse resolution satellite images on the t^{th} day, using the formula:

$$ET_s(t) = ET_s(t) * \frac{ET_{HIGH}(t-n)}{ET_{HIGH}(t-n)} \quad 1$$

where $\overline{ET_{HIGH}(t-n)}$ is the average of the values of $ET^{HIGH}(t-n)$ that occupy a pixel of ET_s (course resolution) on the $(t-n)^{th}$ day. Using this proportional distribution method, the total ET_s value calculated for each area course resolution pixel size is preserved but redistributed according to the detailed pattern of ET data derived from the ET^{HIGH} .

3. Study area and Data Description

The study area was based in Alentejo region, southern Portugal, from which field campaign data were collected, including ground-measured soil moisture, spectral-measurements and surface temperature, soil water-holding characteristics, soil texture, crop types and management information. Remotely sensed data used was acquired from one Landsat 5 Thematic Mapper and time series of high temporal resolution Moderate Resolution Imaging Spectroradiometer (MODIS) for selected days of interest (DOI) over the 2006/2007 cropping season. Secondary data from literature was also used.

Section 3.1 provides background information about the study area. Description of the field and soil related data is given in section 3.2. The meteorological data and remotely sensed data are described in sections 3.3 and 3.4 respectively.

3.1. Description of the Study Area

Within Alentejo region, Roxo watershed was selected as study area. It is located in the Beja district with an area of 353 km², (geographical bounding coordinates, 37°46'44" N to 38 ° 02'39" N latitude and 7 ° 5'47" E to 8 ° 12'24" E longitude). Two sites were particularly of interest, Pisos and Roxo area, both having irrigation command area requiring attention with regard to water resources management. According to (Sen and Gieske 2005), the district's population is 161,200, of which 40,000 live in the Beja town. Fig. 2 shows the study area, including the selected sites.

3.1.1. Physiography and hydrography

The catchment is dominated by rolling plains and arable lands. The altitude of the watershed varies from 123 to 280 m. It is the major food producing region of Portugal. The Alentejo province alone yields 75 per cent of the country's total wheat production, (Sen and Gieske 2005).

"Ribeira da Chamine", which has its source in Beja, is the main perennial river in the Pisos catchment. This river together with seasonal tributary streams, depend on springs and drains the aquifer. The water produced in the catchment is accumulated in an artificial reservoir covering an average area of 1,378 ha, (Sen and Gieske 2005). The construction of reservoir dam was started in 1963 and was completed in 1968. The reservoir water is used mainly for irrigation and domestic purposes. It is also used by some local industries.

3.1.2. Climate

The climate of the study area is Mediterranean, semi-arid and dry with oceanic characteristics, with large temperature intervals between summer and winter and cyclical droughts. The annual average temperature is 16 °C and according to (Sen and Gieske 2005), it reaches a maximum of 40 °C in summer (i.e., July or August) and a minimum of 5 °C in winter (i.e., December).

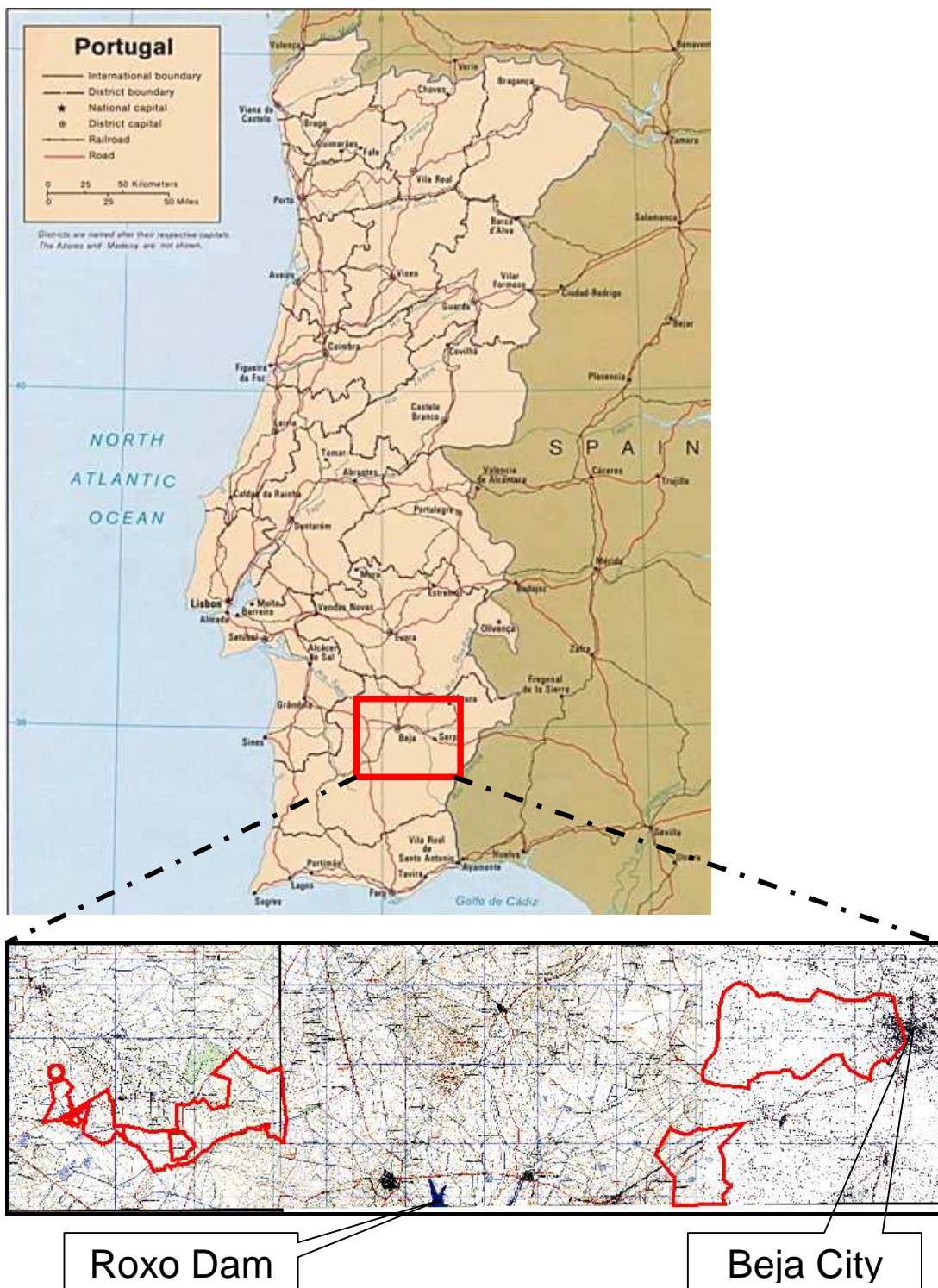


Figure 2: Location of the study area

Average rainfall is about 500-600mm/year. There are two distinct periods: a warm dry summer that occurs between June and September and a wet period occurring between October and March with 75% of total annual rainfall.

The study area is located in the second highest potential evapotranspiration area in Portugal with median values ranging between 1267 to 1376 mm/year. With such high moisture deficit relative to precipitation, agriculture is evidently posed to be dependent of irrigation.

3.1.3. Soils

In (Sen and Gieske 2005), a brief description of soils in the Roxo watershed has been presented based on the soil map of Europe prepared by the European Environmental Agency. The soil types of luvisol, planosol, vertisol, and rendzina are present in the catchment. The vertisol and rendzina dominate the soils of Pisos site. They are deep, clay-rich soils, and can hold moisture up to 200 mm/m. The planosol has a coarse texture and are mainly in Roxo site and can hold moisture up to 60 mm/m. The rice fields are mainly concentrated in these soils. The luvisol is a deep, loamy soil with total available soil moisture (TAM) of 140 mm/m. Map of soils for Pisos site is illustrated in Appendix 1.

3.1.4. Landuse and irrigation

The study sites are mainly agricultural areas with dependency on irrigation. Within Pisos, land-use is mainly cereals (wheat) and sunflower or corn as alternative crops. Other annual crops include beterraba (sugar beet) and cevada. In the Roxo site, the main annual crops are rice, sunflower, corn/maize and tomato. Olive grooves are being established in former annual crop fields.

According to (Paralta 2005), ground water pumping for irrigation is important in Pisos site and is in the range of 4000-5500m³/ha/yr. In Roxo site, Irrigation water is sourced from nearby Roxo Dam and is distributed by canals. Irrigation and mechanized agricultural technology are well established in this region,(Sen and Gieske 2005). In Pisos, centre-pivot system is very common. In Roxo site, apart from rice which is flooded during its growing season, drip irrigation is common in tomato and olive grooves, while traditional spray irrigation system is common in maize fields.

3.2. Description of soil related data

Secondary field data were obtained from Centro Operative de Technological de Regadio (COTR) including soil moisture collected over cropping season and soil water holding characteristics data.

3.2.1. Soil water holding characteristics

Soil water holding characteristics data including field capacity and wilting point were obtained from COTR. Soil samples were collected in eight points, sampled over different soil types shown in Appendix 1. Laboratory measurements of these soil parameters were determined and are tabulated in Appendix 2 and 3. Available water storage capacity was calculated as the residual of field capacity and wilting point.

3.2.2. Secondary soil moisture data

Secondary soil moisture data were obtained from COTR, which were collected on a weekly basis during the irrigation season from selected fields in Pisos, (see Appendix 4 for location of these fields). Exploratory analysis was performed to establish the variation of physical parameters and their effect to soil water holding characteristics, (see Appendix 5.1-5.4).

3.3. Description of Meteorological Data

There are three automatic weather stations in the vicinity of the study area. ADAS station, owned and maintained by ITC is located in Pisos (38° 01' 5.45"N, 07° 54' 36.30"W (altitude 220 m). The other two stations owned by COTR are located in near Beja City (38° 02' 15"N, 07° 53' 06"W (altitude 206m)) and near Roxo Dam (37° 58' 17"N, 08° 11' 25" W (altitude 104 m)). These weather stations were selected due to their close proximity to the catchment area.

The three stations as shown in Fig. 3 are close to each other (especially ADAS and COTR) and therefore measured climatic variables would be expected to correlate as the climatic conditions are the same over the small study area.

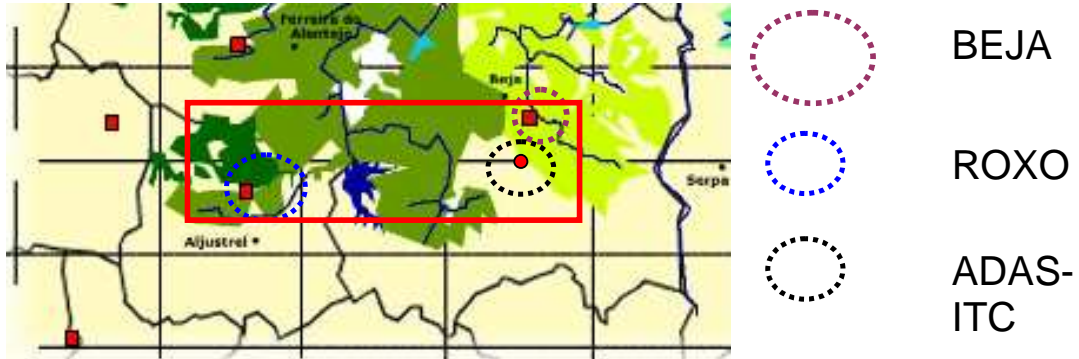


Figure 3: Location of the three meteorological stations (Background map adapted from COTR SAGRA.NET WEBSITE)

Meteorological data (Table 1) was employed as input in implementation of the evapotranspiration procedures investigated but also in validation exercise as detailed in later chapters. Exploratory analysis is presented in Appendix 5.5.

Table 1: Lists of climatic variables employed in this study and the source station

Climatic variable	Weather station
Shortwave radiation	COTR
Daily Reference ET	COTR & ROXO
Temperature data	ADAS
Relative Humidity data	ADAS
Precipitation	COTR
Soil heat flux	ADAS
Daily net radiation	ADAS

3.4. Description of Remote Sensing Data

Remote sensing data were the primary input data in this study, and data sets were obtained from the MODIS sensor. Twenty four sets of MODIS products were acquired for selected days of interest through out the 2006/2007 growing season. Two images of Landsat 5 TM were also acquired on 9th March and 1st September 2007. See Appendices 6.1 and 6.2 for description.

4. Estimation of Crop Evapotranspiration (ET_c) based on Traditional FAO 56 Procedure

4.1. Introduction

FAO-56 methodology was employed to predict crop potential evapotranspiration (ET_c). The method is very common among Irrigation Advisory Services as it is straightforward to implement and with only two terms to consider. According to (Allen and Fao 1998), potential evapotranspiration is estimated as:

$$ET_c = k_c \cdot ET_o \quad 2$$

where ET_o is reference evapotranspiration (mm/day), k_c is single crop coefficient that averages crop transpiration and soil evaporation. Actual evapotranspiration is evaluated from potential evapotranspiration by accounting for soil water content in root zone as (Allen and Fao 1998):

$$ET_a = k_s \cdot k_c \cdot ET_o \quad \text{or} \quad ET_a = k_s \cdot ET_c \quad 3$$

Where k_s is water stress coefficient or soil water availability function (Kotsopoulos 2003). Its magnitude is related to the available soil water in the root zone, the crop species and the prevailing weather conditions

4.2. Implementation of 'Traditional' FAO 56-based model

In this study implementation of the traditional FAO-56 approach was based on equation 2, with Kc obtained from FAO-56 tables for specified crop(s) of interest and reference ET obtained from weather stations. The definition of Kc in this study is the 'single Kc'. The approach avoids the complexity of determining soil evaporation. For the analysis, implementation of this method was limited to winter wheat crop single crop cover (wheat), delineated in a selected site in Pisos catchments, (see Fig. 4). It is a contiguous polygon about 461 Ha comprised of adjacent wheat fields. It was considered large enough to allow comparison with estimates obtained from other approaches.

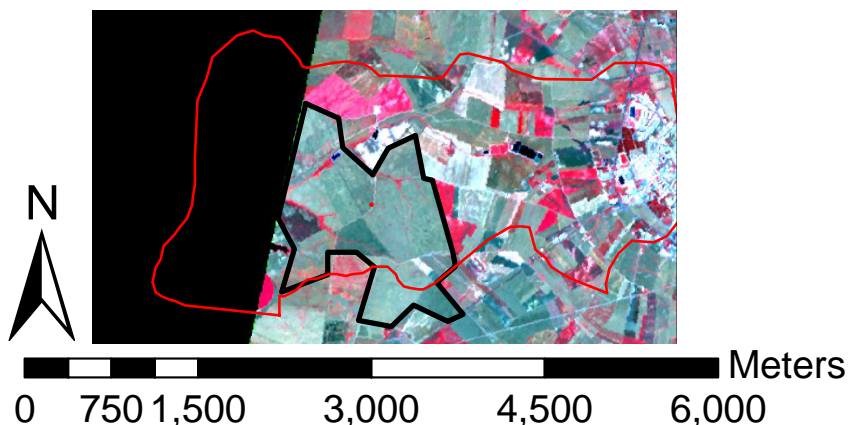


Figure 4: Wheat area delineated for analysis of ET. The background is Aster image of June 2, 2007.

4.2.1. Estimation of reference ET for selected days of interest (DOI)

Reference evapotranspiration data were obtained from COTR and ROXO stations, which were already calculated based on Penman-Monteith equation. This method gives accurate estimate of reference evapotranspiration compared to other methods. It suits well for areas

with readily available meteorological data. The calculation of FAO Penman-Monteith combination equation is defined by (Allen and Fao 1998) as:

$$ET_0 = \frac{0.408\Delta(R_n - G) + \gamma(900/(T + 273))u_2(e_s - e_a)}{\Delta + \gamma(1 + 0.34u_2)} \quad 4$$

where ET_0 reference evapotranspiration (mm day^{-1})
 R_n net radiation at the crop surface ($\text{MJ m}^{-2} \text{day}^{-1}$)
 G soil heat flux density ($\text{MJ m}^{-2} \text{day}^{-1}$)
 T mean daily air temperature at 2 m height ($^{\circ}\text{C}$)
 u_2 windspeed at 2m height (m s^{-1})
 e_s saturation vapour pressure (kPa)
 e_a actual vapour pressure (kPa)
 $e_s - e_a$ saturation vapour pressure deficit (kPa)
 Δ slope vapour pressure curve ($\text{kPa } ^{\circ}\text{C}^{-1}$)
 γ psychrometric constant ($\text{kPa } ^{\circ}\text{C}^{-1}$)

The equation uses standard climatological records of solar radiation (sunshine), air temperature, humidity and windspeed. It predicts the evapotranspiration from a hypothetical grass reference surface that is 0.12 m in height with a surface resistance of 70 s m^{-1} and an albedo of 0.23. The equation provides a standard for comparing evapotranspiration during various periods of the year, in different regions, and for different crops. Standardized equations for computing all parameters in equation 4 are given in (Allen and Fao 1998).

For each day of interest (DOI), input value of reference evapotranspiration (ET_0) was calculated as mean of estimates COTR stations in Beja City and near Roxo, and the output taken as the representative value of the study area.

4.2.2. Crop coefficient curve

Crop coefficient (K_c) varies during the growing period due to changes in vegetation and ground cover (Allen and Fao 1998). The trends in K_c are represented in the crop coefficient curve. As in Fig. 5, only three values for K_c are required to describe and construct the crop coefficient curve: during the initial stage ($K_{c \text{ ini}}$), the mid stage ($K_{c \text{ mid}}$) and at the end of the late season stage ($K_{c \text{ end}}$). In this study, the three K_c s for winter wheat were obtained from tables, (Allen and Fao 1998), (see Fig. 11). Appropriate lengths were obtained from local information and also by characterization of the NDVI profile described later.

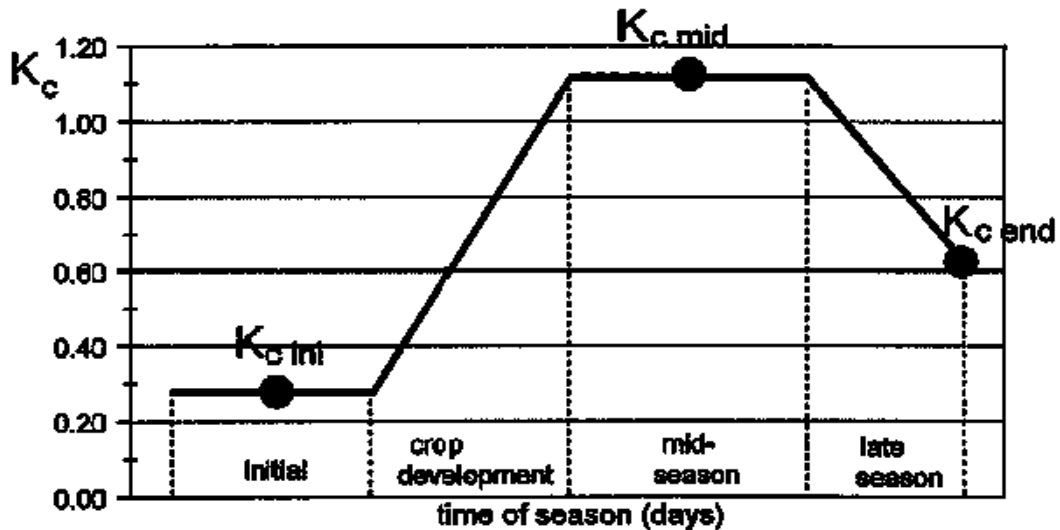


Figure 5: Generalized crop coefficient curve, Adapted from [9]

4.2.3. Estimation of Crop Evapotranspiration (ET_c)

Crop evapotranspiration (ET_c) was obtained by resolving equation 2, where daily ET_o was multiplied by phase-specific K_c for wheat crop. In this study, three days were selected for evaluation of ET_c to provide basis for subsequent analysis-JD 334, 68 and 184 respectively during initial, mid and end phases.

4.2.4. Assessment of the results of 'Traditional' FAO-56 approach

Fig.6 show the temporal variation of ET_o and estimated ET_c based on tabulated FAO-56 based K_c along wheat crop calendar. The averaged ET_o is a good representation of both Pisos and Roxo area, reflected by the degree of similarity of temporal variation in between individual station's values and averaged values (see Appendix 5.5). The low deviation from individual station's values in terms of low mean absolute bias (0.03 mm/day) and root mean square error (RMSE) (0.03 mm/day) for both stations further support this.

The variation of ET_o tends to conform well with variation of mean air temperature and relative humidity during the same period as illustrated in (Appendix 5.5). Air temperature and relative humidity are major factors determining the atmospheric water demand and their fluctuation may explain the observed variation of reference ET.

ET_c estimated based on equation 2 was apparently resonating with ET_o profile during initial and mid phases of winter wheat crop. Low values during initial phase were occasioned by slightly lower ET_c than ET_o. High values during mid season were occasioned by slightly higher ET_c than ET_o. Overall deviation between ET_c and ET_o during initial and mid phases was quite low in terms of bias, mean absolute bias and RMSE (-0.10 mm/day, 0.56 mm/day, and 0.63 mm/day respectively). During end phase, ET_c was very low relative to ET_o attributed to senescence of leaves that constrained transpiration process (estimated 1.69 mm d⁻¹ for JD 184).

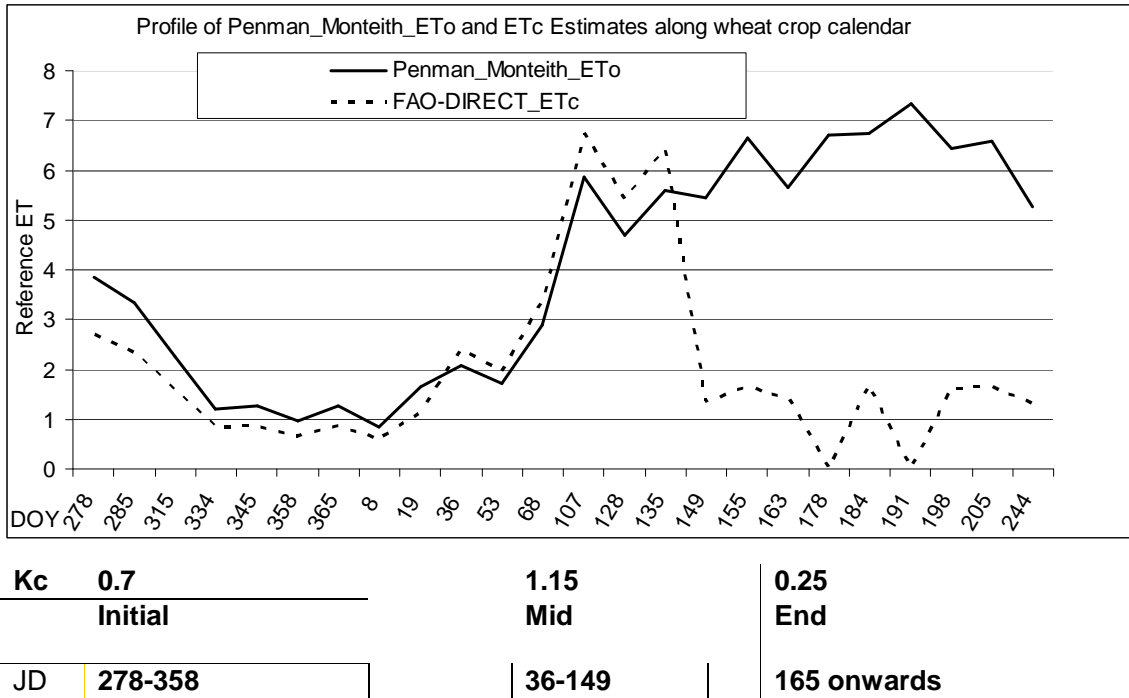


Figure 6: Profile of ETo and ETc based on FAO 56 Kc (tabulated) along the winter wheat growth period (Oct 2006-Aug. 2007), Pisos, Portugal.

Given the high value of tabulated Kc during mid phase, ETc is ideally expected to be high under standard condition. However, it is important to note that the fixed/tabulated Kc may fail to track the dynamic nature of evapotranspiration as influenced by intermittent wet and dry events,(Paco, Ferreira et al. 2006). They noted that crop coefficients vary significantly during the growth season being impossible to assume a constant.

5. Estimation of Evapotranspiration using Simplified Surface Energy Balance Index (S-SEBI)

Scientific community has become interested in estimating evapotranspiration by remote sensing, since it's a unique way to retrieve ET at several temporal and spatial scales. Thus, several remote sensing-based methods have been developed to derive surface fluxes from remote sensing observations (see Chapter 2).

In this study, the focus was on application of Surface Energy Balance Algorithm (S-SEBI) to derive evapotranspiration from evaporative fraction based on the contrast between dry and wet areas. It was chosen as it is simple to implement. Major advantages over other remote sensing flux algorithms are:

1. No addition meteorological data is needed to calculate the fluxes if the surface hydrological extremes are present, and
2. The extreme temperatures for the wet and dry conditions vary with changing reflectance values, while other methods try to determine a fixed temperature for wet and dry conditions for the whole image and /or for each land use class.

Crop classification information was not used by S-SEBI in deriving ET, and this is a positive benefit of such an approach, as accurate crop classification can require much time and expense as the energy balance determination itself, (Tasumi and Allen 2007).

A short introduction of the algorithm is presented in section 5.1. Section 5.2 presents the implementation of the algorithm, focusing on the retrieval of net radiation. Derivation of evaporative fraction, daily evapotranspiration and S-SEBI Kc is described in sections 5.3, 5.4 and 5.5 respectively. Section 5.6 presents evaluation of disaggregation procedure of S-SEBI ET data. Assessment of selected S-SEBI outputs is presented in Section 5.7.

5.1. Introduction

Detailed information on S-SEBI are provided by (Roerink, Su et al. 2000), and only the core elements are considered here. S-SEBI solves the surface energy balance with remote sensing techniques on a pixel-by-pixel basis, following the normal surface energy balance equation:

$$R_n = G_o + H + \lambda E \quad 5$$

Where R_n is net radiation (Wm^{-2}); G_o is soil heat flux (Wm^{-2}); H is sensible heat flux (Wm^{-2}), and λE is latent heat flux (Wm^{-2}). Constitutive parameters for S-SEBI, including surface reflectance, surface temperature and vegetation index that are model input for solving the energy budget equations above, are determined by scanned spectral radiances under cloud-free conditions in the visible, near infra-red and thermal infra-red range.

The net radiation is calculated as residual of all incoming and outgoing shortwave and long-wave radiation, some of which can be detected by remote sensing techniques. The instantaneous soil heat flux (G_o) is derived with an empirical relationship of the vegetation and surface characteristics. The sensible (H) and latent heat flux (λE) are calculated as the evaporative fraction, Λ .

$$\Lambda = \lambda E / (\lambda E + H) = \lambda E / (R_n - G_o) \quad 6$$

To refer to instantaneous dimension corresponding to time of remote sensing data acquisition, then part of this equation is rephrased as:

$$\Lambda_i = \lambda E_i / (R_{ni} - G_i)$$

In S-SEBI algorithm, definition of evaporative fraction is based on the interpretation of the scheme relating surface temperature and reflectance/albedo. Accordingly, partitioning of surface energy fluxes is based on determination of reflectance-dependant extreme temperatures from the remote sensing image. It has been observed that surface temperature and reflectance of areas with constant atmospheric forcing are correlated, allowing the relationships to be applied to determine the effective land surface properties (Roerink, Su et al. 2000).

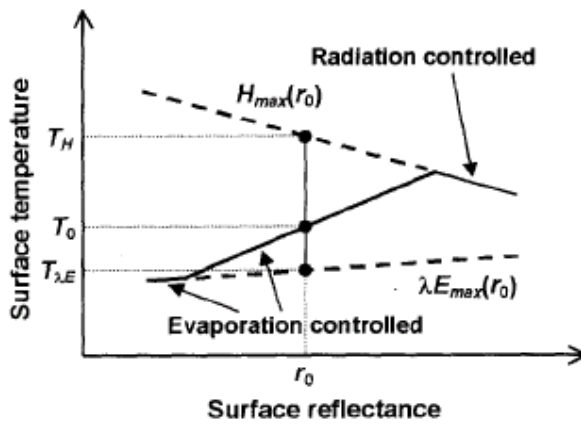


Figure 7: Schematic representation of the relationship between surface reflectance and temperature together with the basic principles of S-SEBI (Adapted from [22])

From the analysis of Fig. 7, at low albedo values, which mainly concern water saturated areas like open water, irrigated lands (where all available energy is used in evaporation process), surface temperature changes less with increasing reflectance, (Roerink, Su et al. 2000) and (Sobrino, Gomez et al. 2005). On the other hand, for higher albedo values, surface temperature increases with albedo. Here, change in temperature is as a result of the decrease of the evaporation with decreasing soil moisture, and may be termed as 'evaporation controlled'. The increase in excess sensible heat flux exceeds the decrease in net radiation due to increase of reflectance. However, beyond a certain threshold albedo value, surface temperature decreases with increasing albedo, as a result of the decrease of net radiation (more is reflected away), (Roerink, Su et al. 2000). Here, change in temperature is said to be 'radiation controlled'.

For a given albedo ($r_0 = \alpha$) value, the variation of surface temperature between the wet and dry lines is mainly related to variations in land surface water availability. For cases where the extreme temperature $T_{\lambda E}$ and T_H can be determined from the image itself and atmospheric conditions are constant over the image and sufficient wet and dry pixels are present throughout the reflectance spectrum, then according to (Gomez 2005), it is possible to define:

- a wet temperature $T_{\lambda E}$, when instantaneous sensible heat flux $H_i = 0$ which induces $\lambda E_{max i}(\alpha) = R_{ni} - G_i$, and
- a dry temperature T_H , when instantaneous latent heat flux $\lambda E = 0$ which induces $H_{max i}(\alpha) = R_{ni} - G_i$.

According to (Roerink, Su et al. 2000), evaporative fraction is then calculated as the ratio of:

$$\Lambda = \frac{T_H - T_0}{T_H - T_{\lambda E}} \quad 7$$

According to (Sobrino, Go'mez et al. 2005), evapotranspiration can easily be obtained from equation 5 once the net radiation, the soil heat flux and the evaporative fraction are known. Estimation of daily evapotranspiration values ET_d (mm day^{-1}) requires the integration of the latent heat flux over the whole day and accounting for the latent heat of vaporization ($L=28.4 \text{ Wm}^{-2} = 2.45 \text{ MJkg}^{-1}$). Since latent heat flux is obtained once a day from remote sensing data, the assumption applied by (Sobrino, Go'mez et al. 2005) and (Gomez 2005) holds, that evaporative fraction at daily scale is similar to the instantaneous values derived from equation 7 at the time of remote sensing data acquisition.

In this way, for daily and instantaneous values, equation 6 is re-written as:

$$\lambda E_d / \lambda E_i = \Lambda_d / \Lambda_i * (R_{nd} - G_d) / (R_{ni} - G_i) \approx (R_{nd} - G_d) / (R_{ni} - G_i) \quad 8$$

These allow expression of daily values ET_d as a function of instantaneous values according to:

$$ET_d = \lambda E_i * R_{nd} / (L * \{R_{ni} - G_i\}) \quad 9$$

where the soil heat flux at daily scale has been assumed close to zero ($G_d = 0$) and R_{nd} and R_{ni} are daily and instantaneous net radiation flux respectively. The conversion may be performed using the ratio between both values as $C_{di} = R_{nd} / R_{ni}$. In (Sobrino 2007), sinusoidal equations defining this ratio as a function of day of the year (DOY) had been formulated using net radiation fluxes measured at a meteorological station in Iberian Peninsula. It was assumed that the atmospheric conditions at that station were similar as in the study area. The equation at 12h GMT was used to calculate the ratio (C_{di}) in this study, (see Fig. 25). In this way, the above equation is re-written as:

$$ET_d = \Lambda_d R_{nd} / L = \Lambda_i C_{di} R_{ni} / L \quad 10$$

5.2. Model Implementation

Implementation of S-SEBI algorithm followed the procedure shown in Fig.8. Pre-processing of remote sensing data was performed followed by computation of model inputs. In a series of calculations employing these inputs, daily evapotranspiration (S-SEBI ET) and then S-SEBI Kc were obtained. Dissaggregation based on weighted ratio approach was then performed and evaluated.

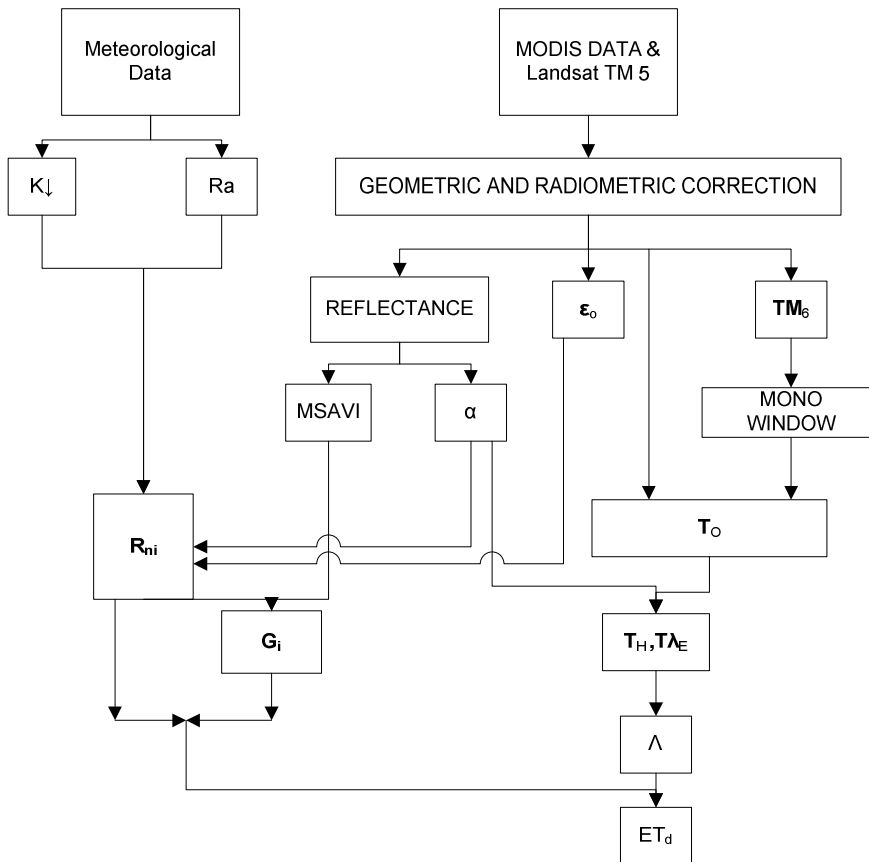


Figure 8: Flowchart of implementing S-SEBI algorithm to obtain evapotranspiration from MODIS and Landsat TM

5.2.1. Pre-processing of Remote Sensing data

Remotely sensed data acquired from Moderate Resolution Imaging Spectroradiometer (MODIS) were the primary inputs employed to implement the model. In total, 24 series of MOD11 Daily Land Surface Temperature (LST) and Emissivity products and Daily Surface Reflectance Products were processed, covering the entire winter wheat growing period. In addition, two Landsat TM 5 images were acquired.

5.2.1.1. Pre-processing of MODIS data

Pre-processing of MODIS data involved reprojection from Sinusoidal projection to UTM projection- Zone 29 N (WGS 84 datum) - fit for the study area. This was carried out using MODIS Reprojection Tool™, free software developed by the MODIS Team (<http://edcdaac.usgs.gov/modis/mod09gav5.asp>). It handles well the reprojection from Sinusoidal projection. Subsetting was also carried out using this tool, by specifying the bounding coordinates of the study area. The raw data were then re-scaled using ArcMap™ and ILWIS™, employing scaling factor for each parameter (0.02 for LST, 0.002 for emissivity and 0.0001 for reflectance data) to obtain final values of LST in Kelvin and dimensionless emissivity and reflectance maps.

Table 2 compares the rescaled emissivity values used in this study with those reviewed from literature.

Table 2: Comparison of emissivity range used in the study against the range reviewed in literature.

Range of emissivity values used in this study		Values employed (Conrad 2007)		by	Values reviewed (Conrad 2007)	by
Min	Max	Max	Min		Range	
0.49	0.99	0.980	0.005		0.981-0.986; 0.976	

Appendix 6.3 present temporal variation of rescaled MODIS LST between October 2006 and September 2007 for selected cover types (see Fig. 9). Appendices 6.4 and 6.5 present the results of investigation of its relationship with shortwave radiation and ground-measured soil moisture.

5.2.1.2. Pre-processing of Landsat TM data and Atmospheric Correction

The acquired Landsat TM data was already geo-referenced in Geographical Coordinate System by the provider. The data was re-projected from geographic coordinates (WGS 84) to UTM projection and then subset to fit the study area, both tasks handled by ArcMap™.

Six TM bands (1, 2, 3, 4, 5, & 7) measures in the visible and near and middle infra-red part of the electro-magnetic spectrum. The DN values of these bands were first converted to radiance, using equation applied by (Roerink, Su et al. 2000).

$$\text{Rad}_{\text{out}\lambda_i} = [a + (b-a) \cdot \text{DN}/255] \quad 11$$

where DN, original digital number recorded for the pixels of each band (λ_i) in satellite image, and a and b are calibration constants in, (see Table 3).

Table 3: Landsat Thematic Mapper band specific constants ([22] and [45])

	Band 1	Band 2	Band3	Band4	Band 5	Band 7
Wavelength (nm)	490+-60	575+-75	670+-70	837+-107	1692+-178	2190+-215
Gsc (mW/cm ² /μm)	195.7	182.9	155.7	104.7	21.93	7.452
a (mW/cm ² /star/μm)	-0.15	-0.28	-0.12	-0.15	-0.037	-0.015
b (mW/cm ² /star/μm)	15.21	29.68	20.43	20.62	2.72	1.44
Weighting coefficient	0.293	0.274	0.233	0.157	0.033	0.011

The corresponding at-satellite reflectance (TOA) for each band ($\text{Ref}_{\text{toa } \lambda_i}$) was calculated using equation applied by (Roerink, Su et al. 2000) expressed as:

$$\text{Ref}_{\text{toa } \lambda_i} = (\pi \cdot \text{Rad}_{\text{out}\lambda_i} \cdot d^2) / (\text{Gsc} \cdot \text{Cos}(\varnothing)) \quad 12$$

where Gsc is the solar constant for the band (table above), \varnothing is the solar zenith angle and d is the relative distance from the earth to the sun, which corrects for the earth's elliptical orbit. A spreadsheet was available for calculation of this parameter.

Once the spectral radiance was estimated for each band, it was possible to proceed with atmospheric correction. Simplified method for atmospheric correction in the solar spectrum (SMAC) was applied. This algorithm converts the TOA reflectivity to at-surface reflectivity. Implementation of SMAC required making explicit the atmospheric conditions present at time of the Landsat TM satellite overpass, including water vapour, aerosols content, ozone etc.

In this study, Ozone thickness was obtained from Ozone data measured by Ozone Mapping Instrument (<http://aura.gsfc.nasa.gov/instruments/omi/>). Aerosol Optical Thickness Data measured by Total Ozone Mapping Spectrometer were obtained from Aerosol Robotic Network (AERONET) program (<http://aeronet.gsfc.nasa.gov/>) for a station located at Evora City, Portugal (N38° 34' 04", W 07° 54' 43"). AERONET is a ground-based remote sensing aerosol network established by NASA. AOD is measured for various wavelengths. Since SMAC algorithm requires AOD at 550nm, the above values were plotted in a feature space and a regression analysis performed. The evaluation yields a fitted equation (referred as Angstrom equation) was obtained, expressed as:

$$AOD_{\lambda_i} = \beta \lambda_i^x \quad 13$$

where λ_i is any specified wavelength. AOD at 550 nm wavelength at time of satellite overpass. For the same day and time, atmospheric water vapour amount were obtained from AERONET, Evora station, Portugal. Table 4 summarizes the data about atmospheric conditions employed in SMAC to perform atmospheric correction of the two Landsat TM images.

Table 4: Summary data of atmospheric condition for the two days during Landsat TM overpass.

Parameter	JD 68 (09-Mar-2007)	JD244 (01-Sep-2007)
AOD (550nm)	0.047	0.298
Water Vapor (gcm ⁻²)	1.31	2.28
Ozone Thickness (DBU)	300-325	300-325

Once the parameters were assembled, SMAC program was run. The output, atmospherically corrected TM Band3 and Band 4 images, for limited number of pixels, were then crossed and regressed with their corresponding at-TOA reflectance. Following inversion procedures, the regression equations were fitted into the TOA reflectance of the corresponding bands to obtain at-surface reflectances of band 3 ($ref_{3\ surf}$) and band 4 ($ref_{4\ surf}$), located in the red and near infrared.

Processing of land surface temperature from Landsat TM band 6 applied mono-window algorithm (Sobrino, Jimenez-Munoz et al. 2004) and (Qin, Karnieli et al. 2001), (see detail in Appendix 7.1). Processing of Landsat TM 5 emissivity maps followed an empirical approach applied by (Roerink, Su et al. 2000), (see detail in Appendix 7.2).

5.2.2. Processing of MODIS NDVI and MSAVI

Normalized Difference Vegetation Index (NDVI) and Modified Soil Adjusted Vegetation Index (MSAVI) are constructed from a normalized difference and therefore low difference between at-sensor and at-the-surface values are expected. For MODIS, the rescaled surface reflectance in red (0.648 μ m) and near-infrared (0.858 μ m) (at 250m resolution) were combined to yield per-pixel NDVI and MSAVI values based on equation 14 and 15 respectively. 24 MODIS NDVI and MSAVI time series were processed, covering the entire period of winter wheat growth period.

5.2.3. Processing Landsat TM 5 NDVI and MSAVI

While many authors including (Tasumi 2005) and (Tasumi and Allen 2007) have used at-satellite NDVI of Landsat TM, it is more accurate to atmospherically correct the TOA values in order to obtain at-surface reflectivities, and in this way, estimate NDVI values more representative of the natural surfaces, called NDVI_{surf}, (Sobrino, Jimenez-Munoz et al. 2004). In this study, at-surface reflectances of band 3 ($ref_{3\ surf}$) and band 4 ($ref_{4\ surf}$) located in the red and near infrared (already atmospherically corrected) were used to construct atmospherically corrected NDVI and MSAVI, (equation 14 and 15).

$$NDVI_{SURF} = (\text{near-infrared}_{surf} - \text{red}_{surf}) / (\text{near-infrared}_{surf} + \text{red}_{surf}) \quad 14$$

For Landsat TM NDVI_{SURF}, estimates for JD 68 and 244 were compared with at-TOA counterpart showing slight bias (-0.29 and 0.06 respectively). For JD 68, substantial improvement of NDVI was rendered by atmospheric correction.

MSAVI was estimated based on method applied by (Huete 1988), expressed as:

MSAVI

$$= \frac{2\rho_{NIR} + 1 - \sqrt{(2\rho_{NIR} + 1)^2 - 8(\rho_{NIR} - \rho_{RED})}}{2} \quad 15$$

Temporal variation of MODIS NDVI and MSAVI are illustrated in Appendices 8.1 and 8.2 respectively.

5.2.4. Computing Input Parameters

For both MODIS and Landsat TM data, net radiation was the primary input term in equation 5 employed. It was obtained by adding net short- and long-wave radiation images, expressed as:

$$\begin{aligned} R_n &= K_{net} + L_{net}, \text{ further decomposed as:} \\ R_n &= K_{\downarrow} - K^{\uparrow} + L_{\downarrow} - L^{\uparrow} \\ &= (1-\alpha) K_{\downarrow} - \sigma \varepsilon_0 T_0^4 + \varepsilon_0 R_a \end{aligned} \quad 16$$

Where K_{\downarrow} is the incoming shortwave radiation, K^{\uparrow} reflected shortwave radiation, α is the surface albedo, L^{\uparrow} is the emitted long-wave radiation, and L_{\downarrow} is the incoming long-wave radiation, and R_a is the incoming atmospheric long-wave radiation at the surface. Net shortwave radiation was calculated from meteorological data of solar global radiation and the albedo map, while the long-wave net radiation from the emissivity and temperature maps and using meteorological data of air temperature and vapor pressure. Procedure to derive these parameters and eventually net radiation employed series of expressions as applied by (Roerink, Su et al. 2000), (Hurtado and Sobrino 2001), (Sobrino, Go'mez et al. 2005) and (Gomez 2005), elaborated in Appendix 9.

5.3. Evaporative fraction

Determination of pixel-wise evaporative fraction employed the surface albedo (α) (see Appendix 9.A) and surface temperature T_0 ; where temperature is related to soil moisture and thus fluxes. Using ILWIS, the two variables were plotted in a feature space plot. Through graphical procedures, toggling between ExcelTM and TECDIGTM softwares, the two extreme reflectance-to-temperature relationships were revealed as per (Roerink, Su et al. 2000) and (Sobrino, Go'mez et al. 2005) and (Gomez 2005). These two relationships for $\lambda E_{max}(r_o)$ and $H_{max}(r_o)$ illustrated in Fig. 7 were defined together with their respective regression variables (see Appendix 10.1) as:

$$\begin{aligned} T_H &= a_H + b_H \cdot \alpha && \text{for upper limit, and} \\ T_{\lambda E} &= a_{\lambda E} + b_{\lambda E} \cdot \alpha && \text{for lower limit} \end{aligned} \quad 17$$

Instantaneous evaporative fraction (λ_i) was then calculated based on the method applied by (Roerink, Su et al. 2000), expressed as:

$$\lambda_i = (a_H + b_H \cdot \alpha - T_0) / (a_H - a_{\lambda E} + \alpha (b_H - b_{\lambda E})) \quad 18$$

Appendices 10.2 and 10.3 present respectively the temporal analysis over selected cover types and results of investigation of relationship between evaporative fraction and with soil moisture. Other intermediate derivatives of instantaneous fluxes of soil heat, latent heat and sensible heat flux were also processed, (see Appendix 11).

5.4. Daily Evapotranspiration

In this study, daily evapotranspiration maps for both MODIS and Landsat TM were obtained from net radiation, the soil heat flux and the evaporative fraction based on Equation 10. Daily evapotranspiration estimates were derived from the 26 MODIS time-series as well as the two Landsat TM 5 remotely sensed data.

5.5. S-SEBI-based K_c

Actual evapotranspiration already processed from MODIS time series and Landsat images using SSEBI algorithm were employed in the derivation of SSEBI-K_c. The procedure applied by (Tasumi and Allen 2007) was followed. Accordingly, pixel-wise single crop coefficient images (K_c) were created by dividing the SSEBI-derived ET images by reference evapotranspiration (ET_o) based on the Penman-Monteith method, expressed as:

$$K_c = ET / ET_o \quad 19$$

Daily ET_o was the average of two COTR weather stations, at Beja City and near ROXO dam, similar to application in the previous 'traditional' FAO 56 approach.

5.6. Dissaggregation of S-SEBI ET data based on weighted ratio

Dissaggregation procedure based on weighted ratio approach was implemented between respective S-SEBI ET estimates from MODIS and Landsat TM based on equation 1, (see dissaggregation flow diagram adapted from (Vazifedoust 2007) in Appendix 25). First, S-SEBI ET of Landsat TM generated on JD 68 based on S-SEBI algorithm and reflectance-based approach was aggregated linearly, to yield respective average values that occupy a pixel of MODIS. Since only slight difference exists between arithmetic and geometric means, the latter was employed and the outputs were simulated MODIS products maps.

Then, the corresponding products derived from Landsat TM generated on JD 68 and simulated MODIS images were used to characterize the proportion ratios of pixels within one single large MODIS pixel in form of a ratio map. In turn, the ratio map was then stretched into original MODIS S-SEBI ET as expressed in equation 1, first in JD 68 and then in selected Julian Days, (334 and 184).

The similarity between S-SEBI ET derived from Landsat TM 5 with corresponding products from MODIS was evaluated. The former were aggregated to allow comparison. Accuracy of derived disaggregated maps was assessed both qualitatively and quantitatively in terms of spectral and spatial quality. According to (Chemin 2004), spectral quality is the level at which the produced images/maps retain the pixel values of the corresponding original images. Spatial quality is the level at which the produced images retain the spatial information of the corresponding high resolution images. Evaluation of improvement of spatial resolution over the selected days was analysed by comparing the disaggregated products with the original products directly derived from MODIS in terms of the measures of spatial variability.

5.7. Assessment of selected S-SEBI outputs

As earlier indicated, the focus of implementing S-SEBI model was to obtain key ET data for comparison with outputs of other approaches. It is important to stress the following features:

1. Several intermediate outputs were processed as maps allowing quick visual monitoring;
2. Tracking of pixel-wise temporal variation of the estimated parameters between October 2006 to September 2007 was possible since time series of MODIS estimates

were available. For the purpose of this study, temporal analysis was limited to selected crop cover types over Pisos and Roxo area, (olive grove, beterraba, maize (Roxo), maize (Pisos), rice and wheat), (see Fig. 9).

Appendix 24 elaborates more on the analytical techniques and definitions of expressions applied in this study.

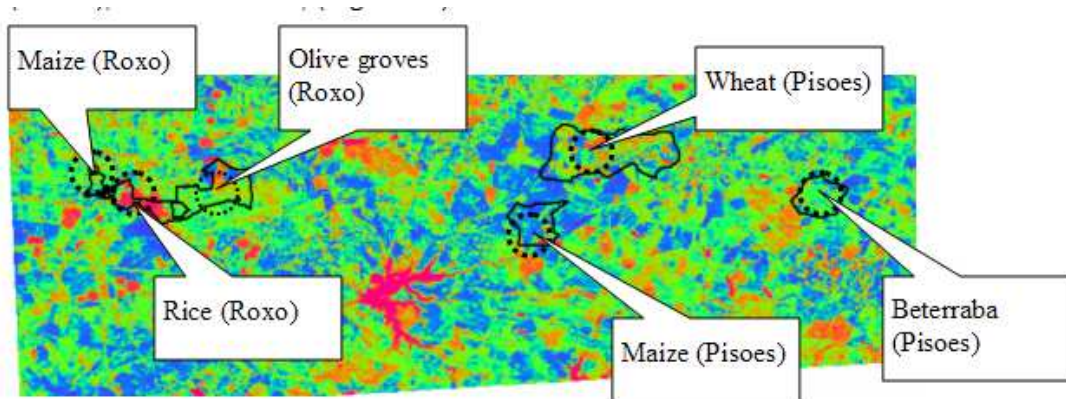


Figure 9: Selected zones over the Pisos & Roxo study block to analyze spatial distribution and temporal evolution of evapotranspiration data from October 2006 to September 2007.

5.7.1.1. Net radiation

Typical net radiation map of 1st September 2007 is shown in Fig. 10. From Fig. 11, it's observed that the net radiation profile was positive over the whole period (October 2006 to September 2007), apparently lowest in winter (335 W/m²), gradually rising there after, and stabilized as summer began (around 630 W/m²). This general trend is expected, given the seasonal cycle and position of the sun that influences much of the incoming shortwave radiation.

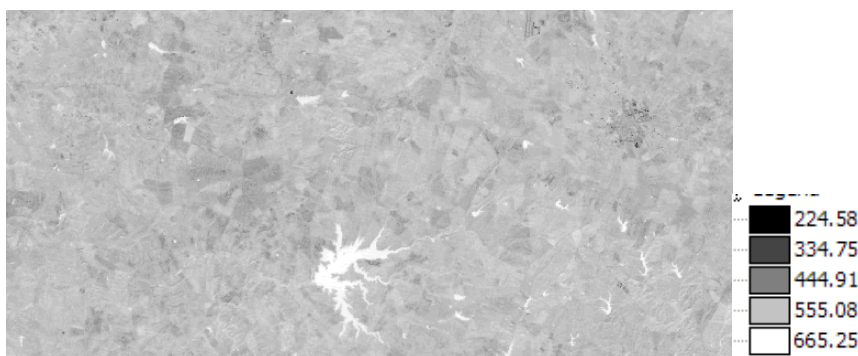


Figure 10: Landsat TM estimate of net radiation, JD 68

Apparently, rice field maintained relatively high net radiation than other crop fields during the later part of the profile. Again, net radiation being the residual of energy absorbed, reflected and emitted energy meant that cover types like rice paddies that were watery during the later part of the profile would reflect and emit less thus retaining high net radiation.

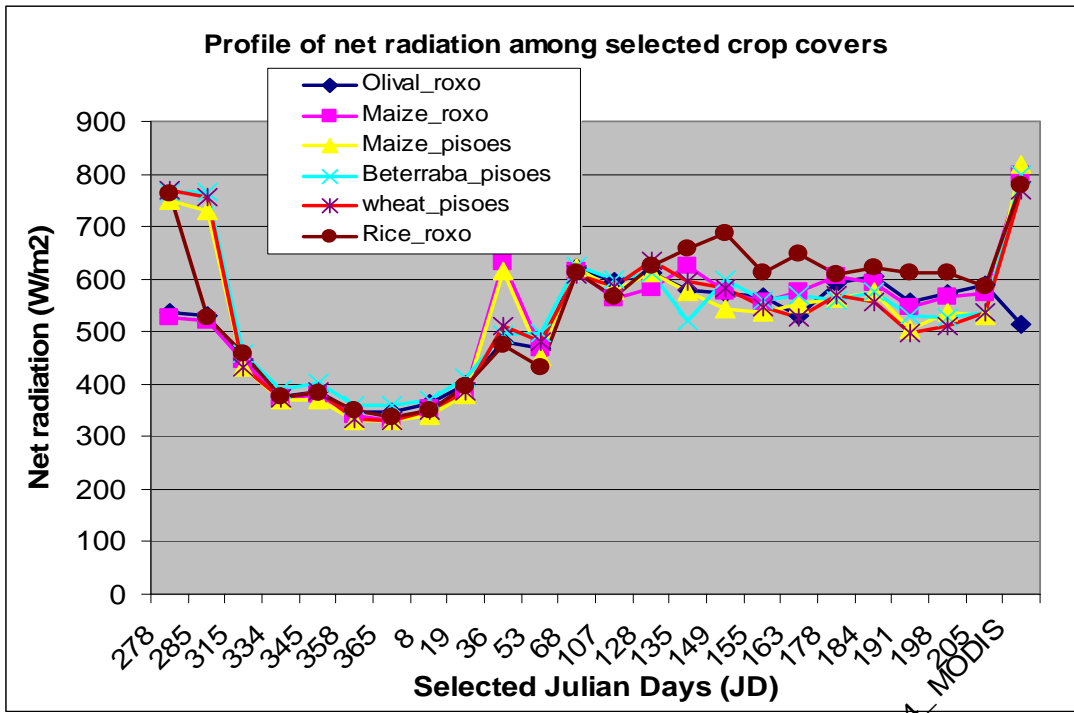


Figure 11: Temporal variation of net radiation in Pisoes and Roxo area, (Oct. 2006-Sep. 2007).

5.7.1.2. Daily evapotranspiration

Fig. 12 display map of daily evapotranspiration for 1st September 2007 (derived from Landsat TM). Temporal variation of mean S-SEBI ET for the whole study block is shown in Fig. 13. Variation between selected crop cover types is shown in Fig. 14. For JD 68, estimates of MODIS were substituted by Landsat TM estimates.

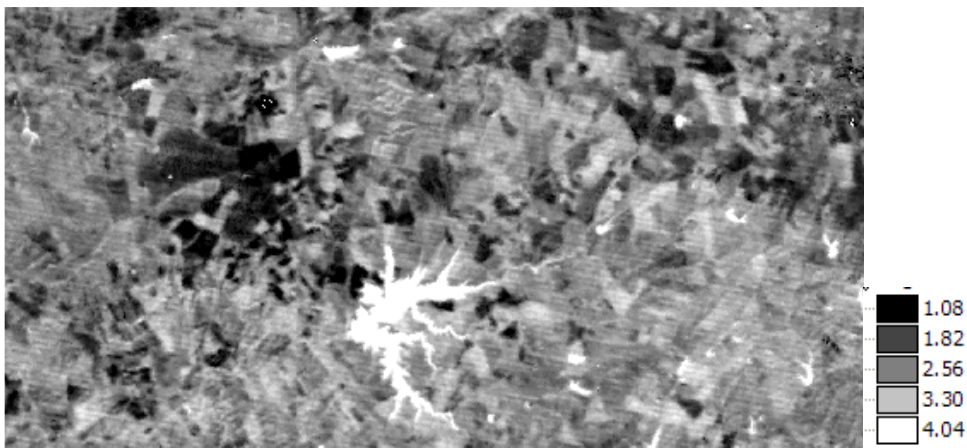


Figure 12: Landsat TM estimate of daily evapotranspiration map, JD 68

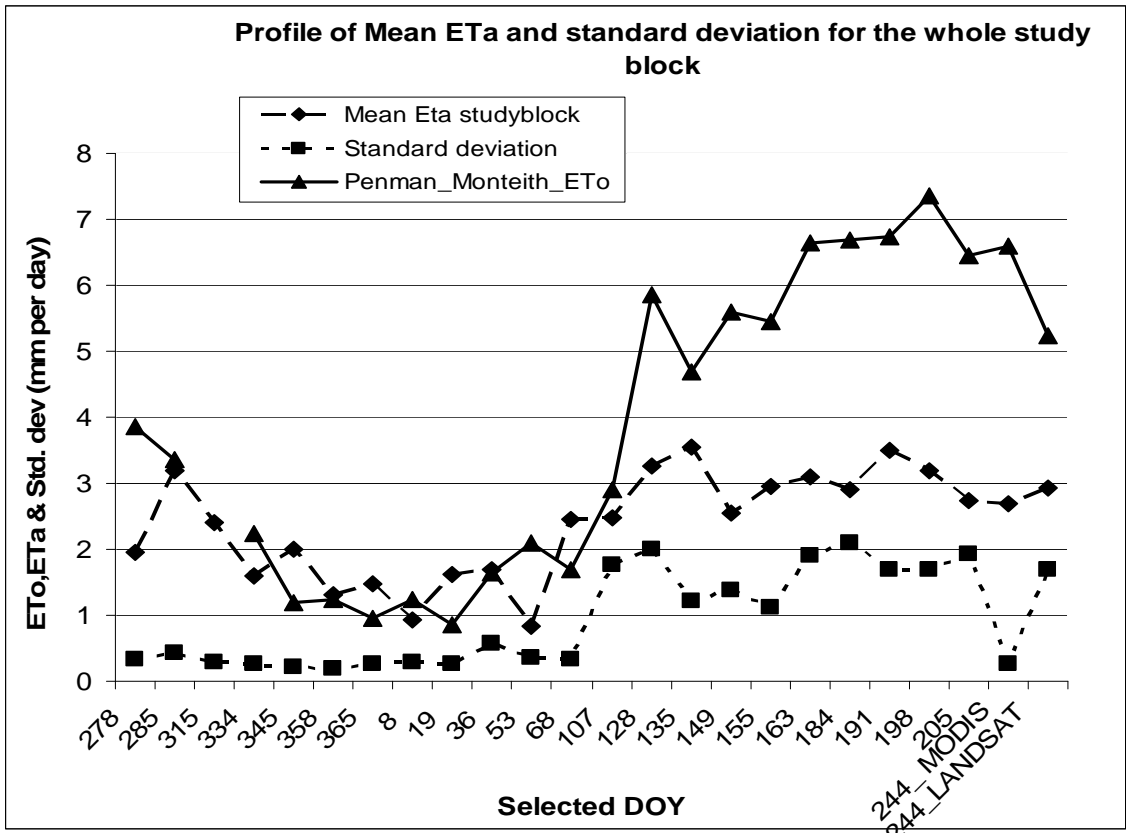


Figure 13: Mean Temporal variation S-SEBI ET and standard deviation and Penman-Monteith for the whole study block, (Oct 2006-Sept. 2007).

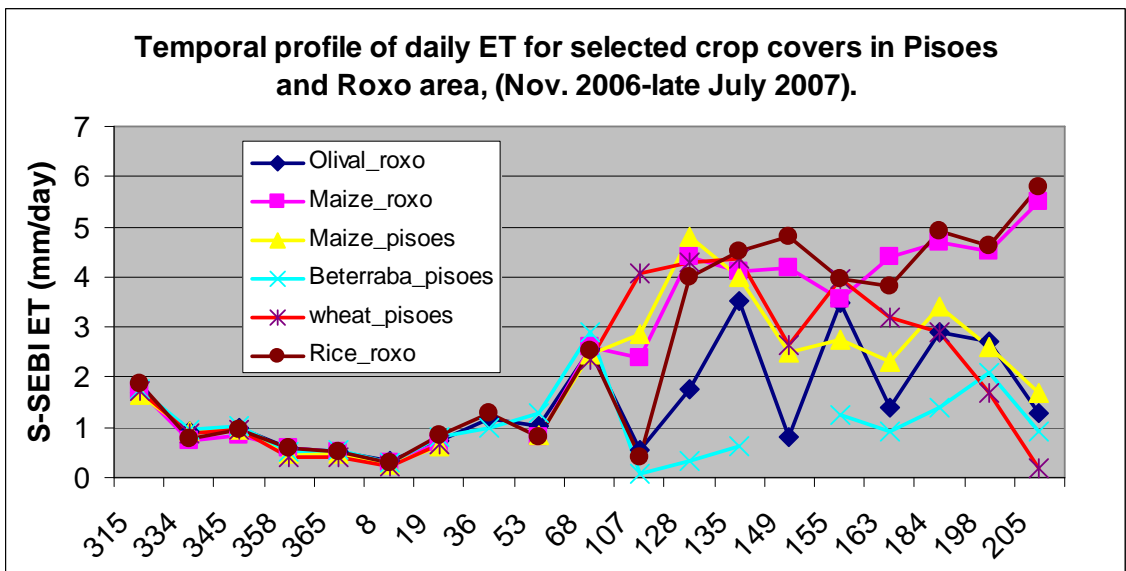


Figure 14: Temporal variation of daily evapotranspiration in Pisos and Roxo area, (Oct. 2006-Sep. 2007).

Estimates of S-SEBI ET during the first period (November-end December) were relatively low and generally in a declining mode for most crop cover types, (2.5 mm/day-1 mm/day). Variation between crop cover types was also low.

According to (Choudhury 1994), at low values of leaf area index (LAI), soil evaporation is the main determinant of evapotranspiration rates. In (Duchemin 2006), it was observed that instances of high evapotranspiration rates and low LAI and NDVI values correspond to periods where soil evaporation was predominant. This is further supported by lack of correlation between the profiles of S-SEBI ET and NDVI (see Fig. 15) during the first period. ET was relatively high when NDVI was low. Since precipitation was frequent and more or less uniform in Pisos and Roxo (see Appendix 5.5.1), soil evaporation was expected to be more or less uniform, explaining the observed low variation (low standard deviation) of S-SEBI ET between the crop types during this period before March.

In subsequent crop development stages as vegetation cover developed, this trend was expected to change following the interaction between soil evaporation and transpiration, such that a decrease in soil evaporation can get compensated by an increase in transpiration to maintain a conservative total evaporation, (Choudhury 1994). After mid-January (JD 19), estimates of S-SEBI ET were relatively higher compared to estimates of previous period for most crop covers and associated with increased variation between crop covers. Significant deviation was observed in end February and March and among some crop covers (beterraba field) which may be attributed to stress events.

In Roxo, the selected rice and maize fields tended to have similar profile of ET, apparently rising fast after mid-January through May and then taking a gradual rise, peaking at about 5.5mm/day. In Pisos, ET profiles of selected wheat and Pisos maize fields were apparently similar, rising fast after March through April (peaking at about 4.5 mm/day) before taking a gradual decline.

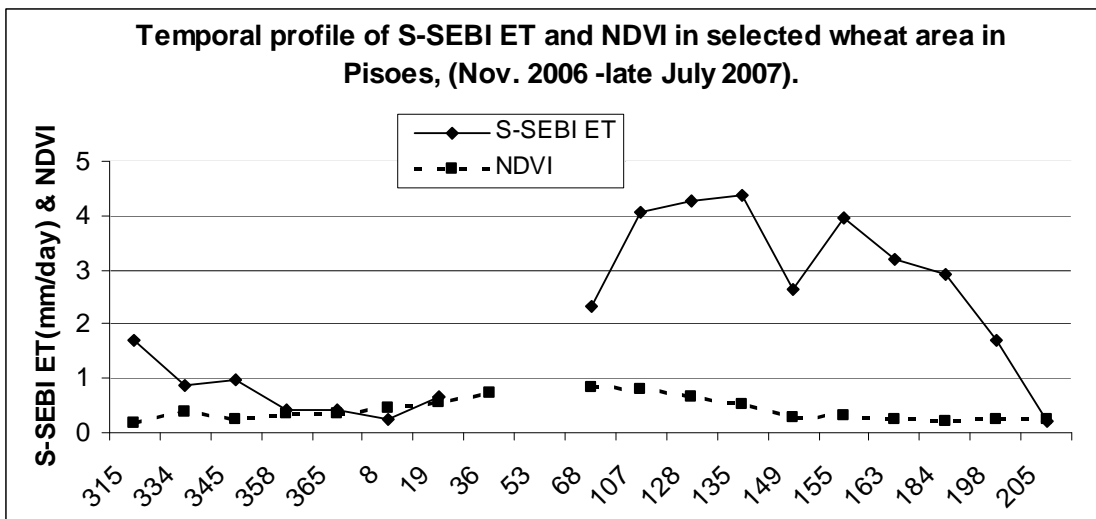


Figure 15: Correlation between NDVI and S-SEBI ET in winter wheat area in Pisos between October 2006-September 2007.

These observations may suggest that the variability between crop covers and moisture availability was influencing the variability of evapotranspiration rates/profiles. The contribution of crop variability, represented by NDVI, has been reported by (Tasumi 2005). They observed that fields having high NDVI values also had high transpiration rates and reduced rates for direct soil evaporation. Contribution by changes in soil moisture regime is implied given the expected variability from field to field on the basis of irrigation practices of individual fields. In the case of Pisos, for instance, irrigation only commenced after March and the rate of application varied across fields. Maize field experienced more irrigation events than beterraba. In Roxo, rice paddies were watery during the second period through March onwards. Coupling of frequent irrigation with high transpiration rates was reported by (Tasumi 2005).

To verify this proposition, relationship between temporal variation of the crops/fields (expressed as NDVI) and S-SEBI ET was investigated for the period through March onward. Similarly relationship between the estimated evapotranspiration and soil moisture was also investigated for the same period.

With respect to NDVI and S-SEBI ET relationship, (see figures 16 and 17), weak positive linear and moderate polynomial relations were obtained in maize (Pisoes) and wheat fields, ($R^2= 0.24$ and 0.61) while in beterraba and maize (Roxo) fields, moderate negative correlations were obtained ($R^2=0.52$ and 0.48 respectively). In olive grooves and rice field, no correlation was observed.

The negative (and lack of) correlations observed in some cases deviates from what was reported by other researchers for instance (Martyniak 2007), where a strong correlation between evapotranspiration and NDVI of spring cereals was observed. Possible explanation of the unexpected observations may be attributed to potential lag of NDVI to register change in evapotranspiration rates. In (Duchemin 2006), it was noted that drop in actual evapotranspiration during stress events may not immediately impact NDVI which may still be high and stable during some days after the beginning of stress. They noted that water shortage does not affect considerably and immediately neither the capacity of canopies to absorb photosynthetically active radiation nor the structural properties of the plant. This limits ability of NDVI to distinct variation of ET across crop cover types. Another possible explanation may be the strong influence of complex vegetation and environmental features on NDVI and ET due to coarse resolution as suggested by (Martyniak 2007).

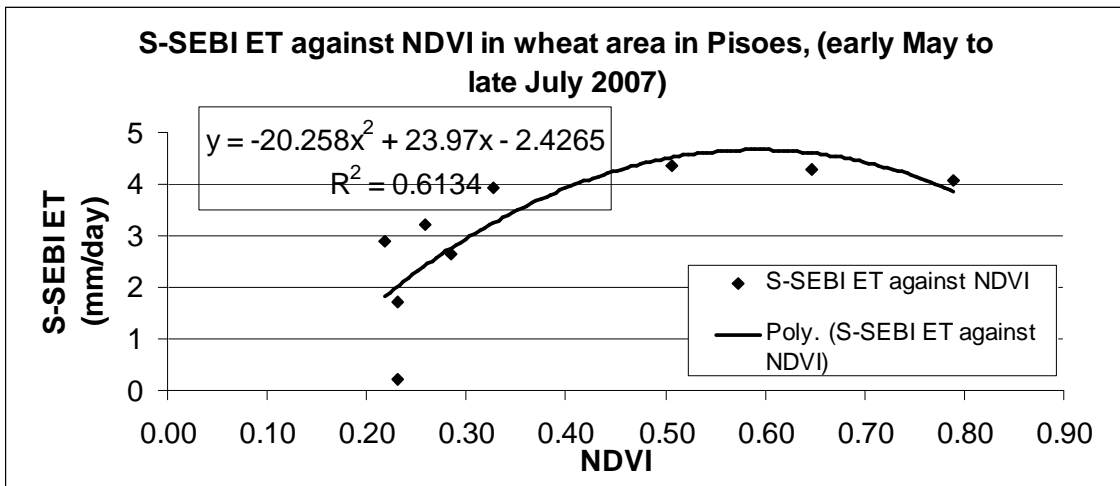


Figure 16: Relationship between S-SEBI ET and NDVI in wheat field in Pisoes (early May to Late July 2007)

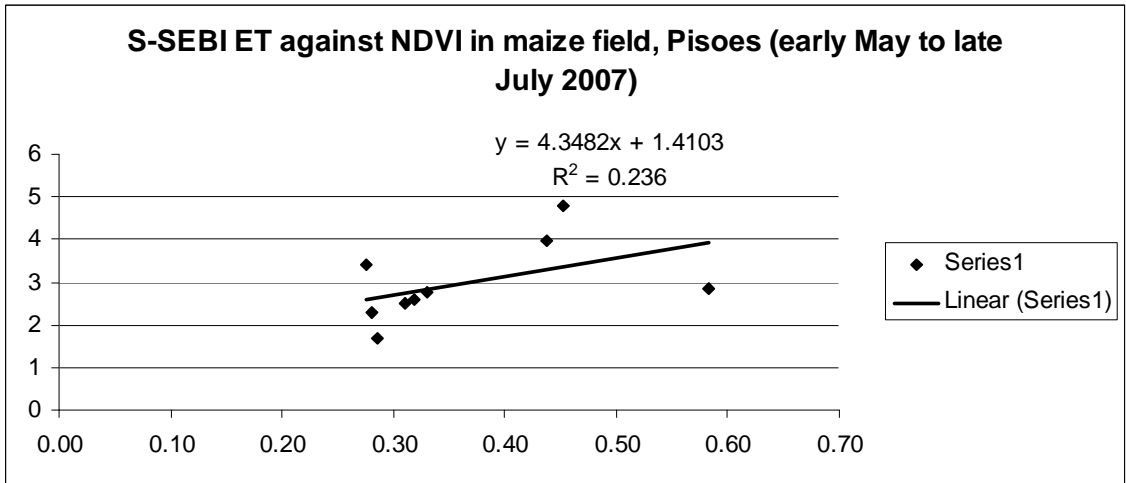


Figure 17: Relationship between S-SEBI ET and NDVI in maize field in Pisos (early May to Late July 2007)

With respect to soil moisture (see figures 18 and 19), there was apparently no relationship with S-SEBI ET in beterraba and maize (Pisos) fields, both for surface layer and depth-averaged moisture. The observed lack of relationship between evapotranspiration and soil moisture availability was not expected and deviates from the direct relationship from theoretical derivation. (Su 2003) also reported similar unexpected observations. These observations may be attributed to the inherent nature of course resolution of MODIS ET estimates when related to the few ground-based soil measurements within the 1 square km of MODIS pixel may naturally introduce scatter in the relationship. It should also be noted that temporal variation of soil moisture status was very low between monitoring events. As such, changes in S-SEBI ET could not be adequately reflected by soil moisture regime.

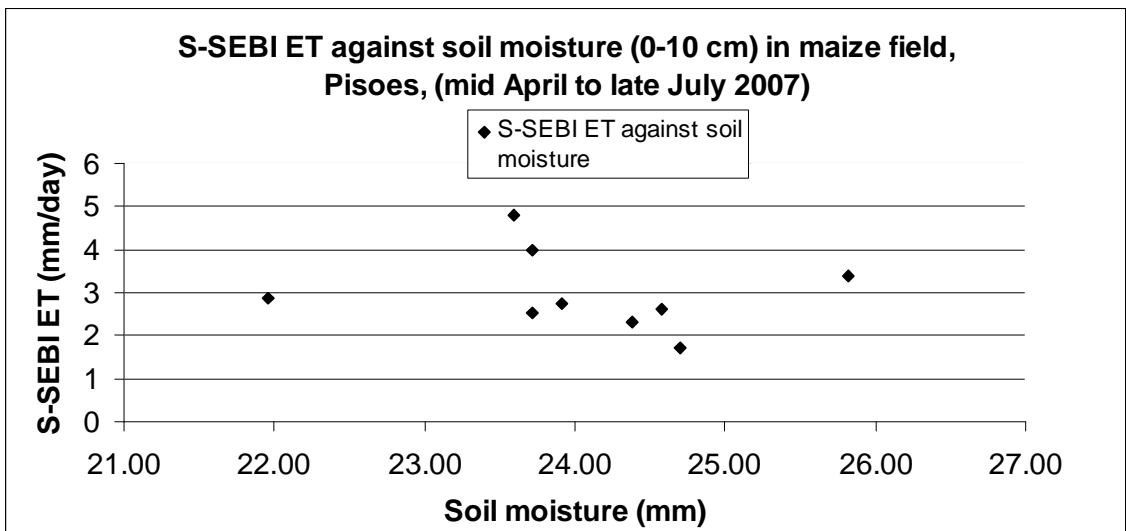


Figure 18: Relationship between S-SEBI ET and soil moisture (surface layer: 0-10 cm) in maize field in Pisos (mid April to Late July 2007)

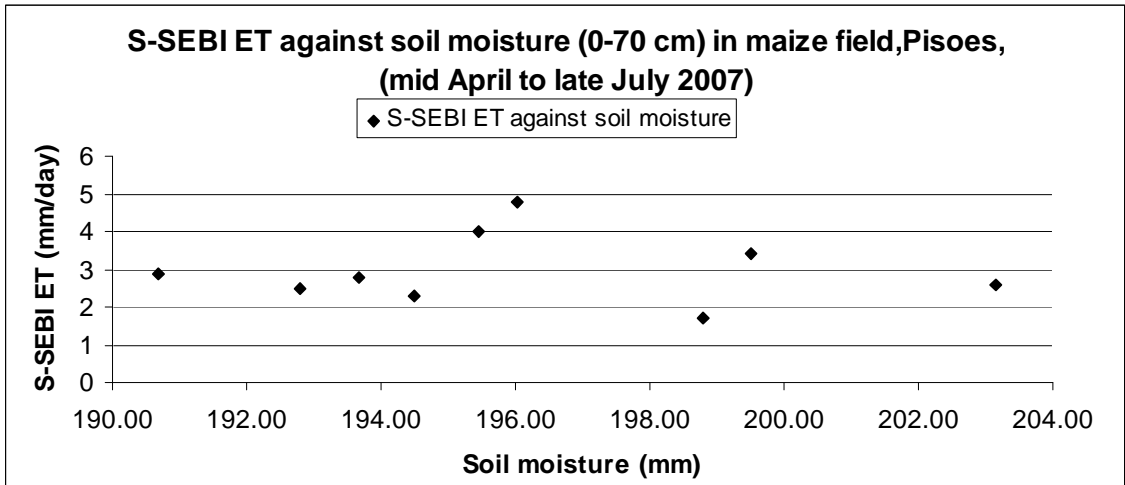


Figure 19: Relationship between S-SEBI ET and soil moisture (depth-averaged: 0-70 cm) in maize field in Pisos (mid April to Late July 2007)

5.7.1.3. Results of validation of estimates derived from S-SEBI Algorithm

Validation of the outputs from S-SEBI algorithm was constrained due to absence of the conventional validation schemes, namely lysimeters, scintillometers or eddy covariance systems, (Roerink, Su et al. 2000) and (Sobrino, Go'mez et al. 2005). The approach followed by (Conrad 2007) was employed in this study, comparing S-SEBI estimate of actual evapotranspiration extracted over water surfaces with ET calculated using AWSETTM, but adjusted for water surface to simulate Pan-ET. In this study, the S-SEBI-ET was extracted from Roxo Dam. Another validation element involved comparison of S-SEBI estimate of instantaneous net radiation with corresponding values from COTR weather station (near Beja City). Values for the weather station were calculated by implementation of equations 38, 39 and 40 of (Allen and Fao 1998). For conversion to instantaneous values, the sinusoidal equation at 12h GMT derived by (Sobrino 2007) was used to calculate the ratio (cdi) between daily (R_{nd}) and instantaneous net radiation (R_{ni}), (see Fig. 20).

From the correlation plot of instantaneous net radiation (see Fig.21), estimates obtained from the two sources were correlating. However, S-SEBI overestimated during the initial period when net radiation was generally low, and underestimated during period of high net radiation. The scatter plot (see Fig.22) also indicate a strong positive correlation ($R^2=0.74$). Statistical measure of deviation in terms of BIAS/ME, mean absolute bias (MAB) and RMSE for the period between November 2006 and late July 2007 are -20 W/m^2 , 91 W/m^2 and 98 W/m^2 respectively. Relative error (RE) was about 19 % of the calculated mean based on weather data. Other researchers working with S-SEBI like (Sobrino, Go'mez et al. 2005) and (Gomez 2005) had obtained a RE = 7%.

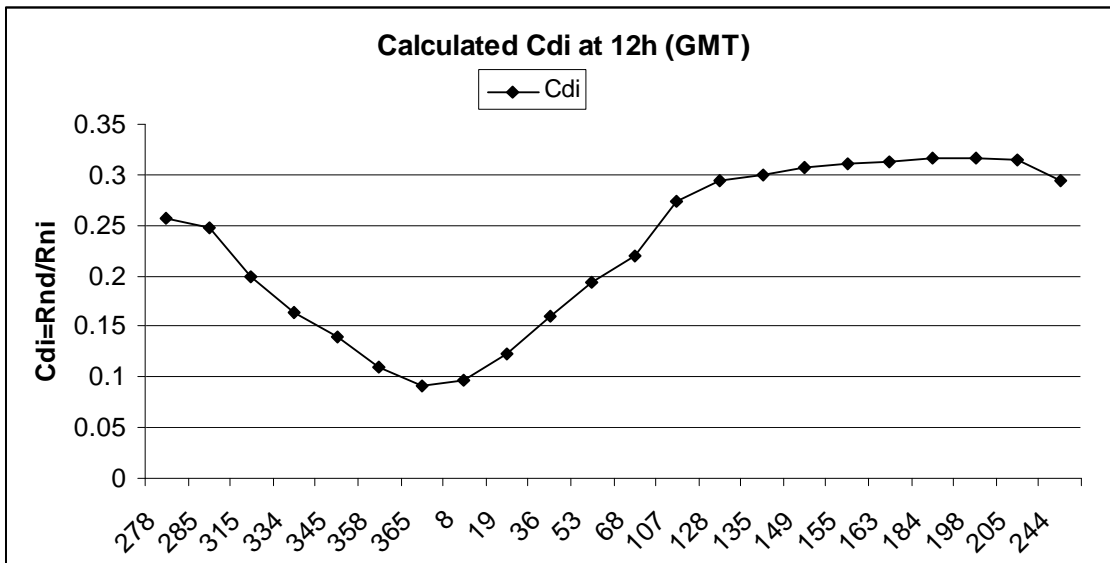


Figure 20: Calculated ratio (Cdi) between daily net radiation (Rnd) and instantaneous (Rni) net radiation ($Cdi = Rnd / Rni$) versus the day of the year. The calculation was based on sinusoidal equation derived by [61] based on net radiation fluxes measured in a met

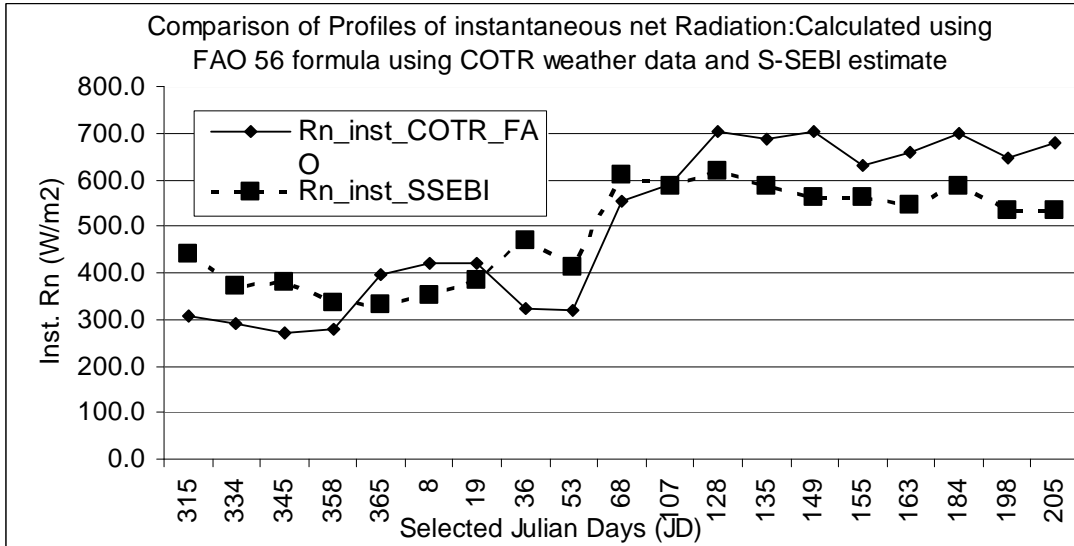


Figure 21: Correlation between S-SEBI instantaneous net radiation estimates against estimates based weather station measurements (COTR near Beja City) between October 2006-September 2007.

The slightly larger deviation observed in these study in comparison to similar studies, may be attributed to errors propagated by the input parameters for estimation of net radiation, although it was difficult to establish the accuracy of the magnitude of errors contributed by each, including albedo, emissivity and surface temperature. It was noted that albedo values, though were underestimated towards the minimum tail, were generally in good agreement with the values in the literature (see Appendix 9.A.3), while averaged MODIS emissivity data in the early part of the growing season was underestimated compared to values suggested in the literature, (see Table 2). (Gomez 2005) reported that underestimation of albedo result in

net radiation overestimation. The accuracy of validation dataset should also not be overlooked as it can as well contribute to such deviations. According to (Bisht 2005), ground observation data are discrete and limited in number and also the measurement error associated with such measurements should be kept in mind while performing comparison. Again, the observed deviation may be due to the coarse resolution of a square km pixel of MODIS sensor where the averaged value is a representation of spatially varied variable within the pixel, (Su 2003). Correlation with few discrete ground measurements, in this case taken from only one weather station in the pixel, is severely constrained.

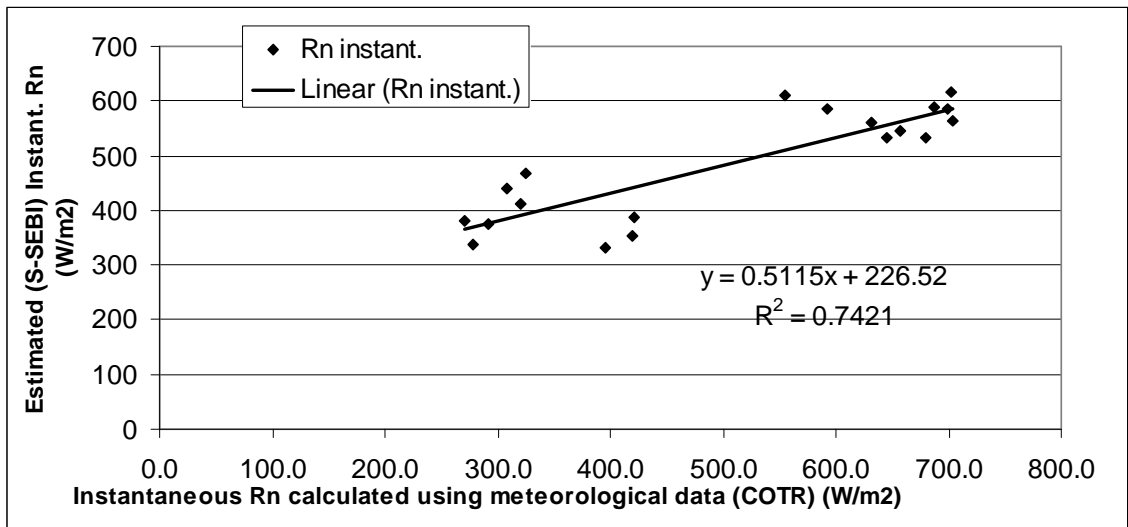


Figure 22: Comparison between S-SEBI instantaneous net radiation estimates against estimates based weather station measurements (COTR near Beja City) between October 2006-September 2007.

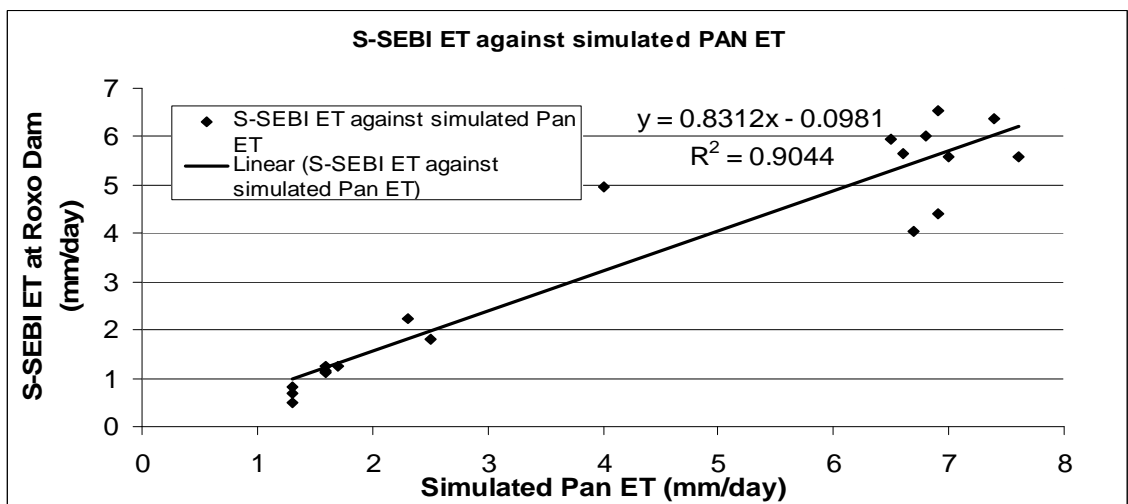


Figure 23: Comparison of S-SEBI ET estimates (in Roxo Dam) with meteorological estimates of simulated PAN ET.

The result of validation of actual evapotranspiration following the method of (Conrad 2007) indicated that the model outputs were plausible. Comparison of S-SEBI ET with simulated PAN ET showed good agreement, (see linear correlation in Appendix 10.4). This was further

supported by high coefficient of determination ($R^2=0.90$), (see Fig. 23), low bias, MAB, RMSE and RE, (-0.82 mm/day, 0.93 mm/day and 1.16 mm/day respectively). Relative error was about 27%. The RMSE was not very different from that obtained by (Sobrino, Go'mez et al. 2005).

5.7.1.4. S-SEBI-based crop coefficient (S-SEBI-Kc)

Typical map of S-SEBI Kc for 1st September 2007 (derived from Landsat TM) is shown in Fig. 24). Profiles of selected crop covers are displayed in Fig. 25. Correlation of S-SEBI Kc and NDVI is also shown in Fig. 26. S-SEBI Kc was high during the initial period when vegetation cover was low. Further, the variation was relatively low between crop covers. This may be attributed to influence of soil evaporation which was expected to be high as a result of frequent precipitation events more or less uniform over the surface during that period, (see Appendix 5.5.1). In (Duchemin 2006), high values of Kc were observed in condition of low vegetation cover and attributed to significant impact of soil evaporation component at low levels of vegetation covers, (Tasumi 2005). Also, (Choudhury 1994) commented that changes in soil evaporation significantly affect Kc for low values of leaf area index, and introduces considerable scatter in the relation between the crop coefficient and leaf area index.

In subsequent period (during full cover), the two variables were expected to relate directly. In (Tasumi 2005), a strong relationship between NDVI and Kc was observed during mid-season; with fields having high NDVI values associated high Kc. Relationship between temporal variation of the crops covers (expressed as NDVI) and S-SEBI Kc was investigated for the period after March onward, (see figures 27 and 28). Again, the relationship between estimated S-SEBI Kc and soil moisture availability was also investigated in the same period, (see Fig. 29).

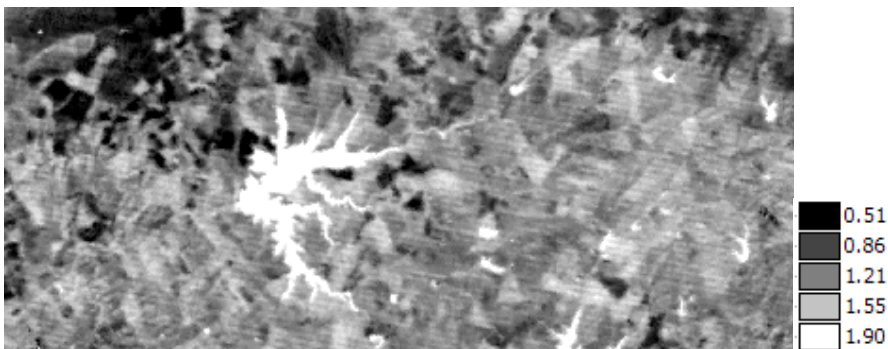


Figure 24: Landsat TM estimate of S-SEBI Kc, JD 68

With respect to NDVI and Kc, positive correlations were obtained in wheat and maize (Pisoes) fields, ($R^2= 0.54$ and 0.26 respectively). In beterraba and maize (Roxo) fields, negative correlations were obtained ($R^2=0.52$ and 0.17). However, there were no correlation in rice field and olive grooves.

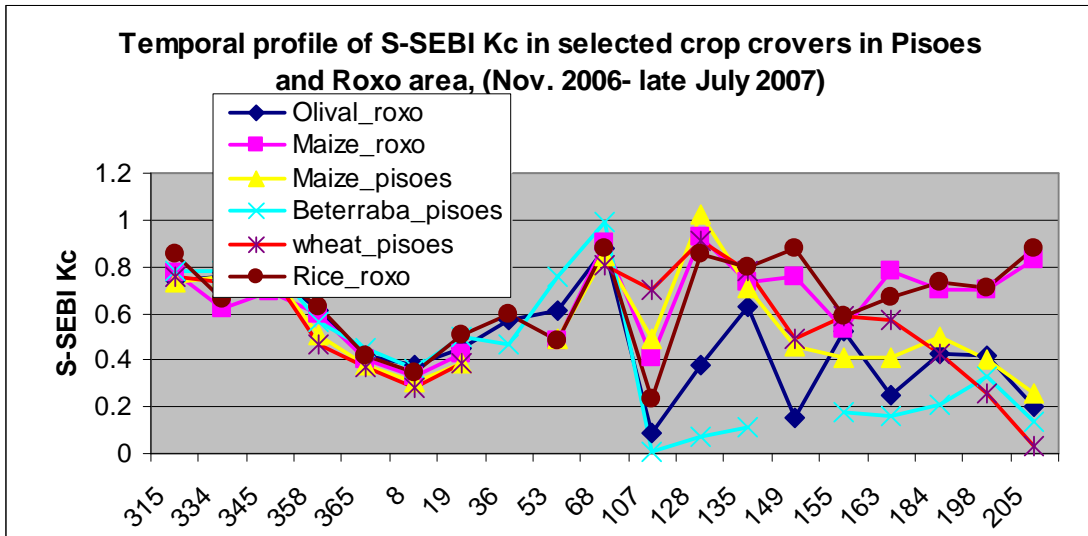


Figure 25: Profile of S-SEBI Kc in Pisos and Roxo area, (Oct. 2006-Sep. 2007).

The unexpected observations of lack of (and in some cases negative) NDVI and S-SEBI Kc relationships may be attributed to potential lag of NDVI to register drop of evapotranspiration, similar to the explanation noted earlier for S-SEBI ET. In (Duchemin 2006), instances with low Kc versus high NDVI / LAI values was observed to be associated with stress events. Lack of immediate response on the part of NDVI to changes of S-SEBI Kc introduced unexpected scatter and possibility for inverse relationship as was observed.

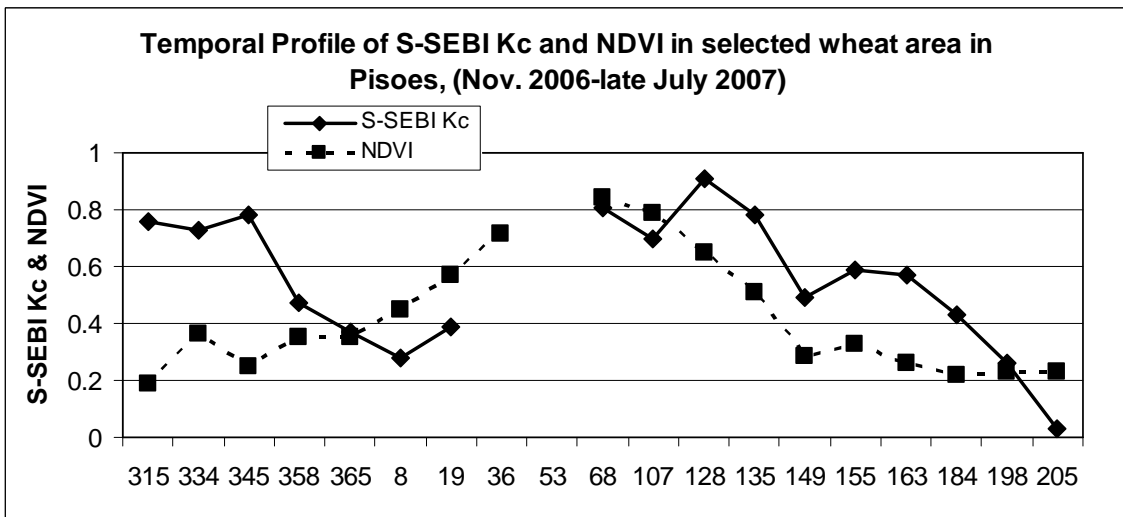


Figure 26: Comparison of profiles of S-SEBI Kc and NDVI in wheat area in Pisos, (Oct. 2006- Sep. 2007).

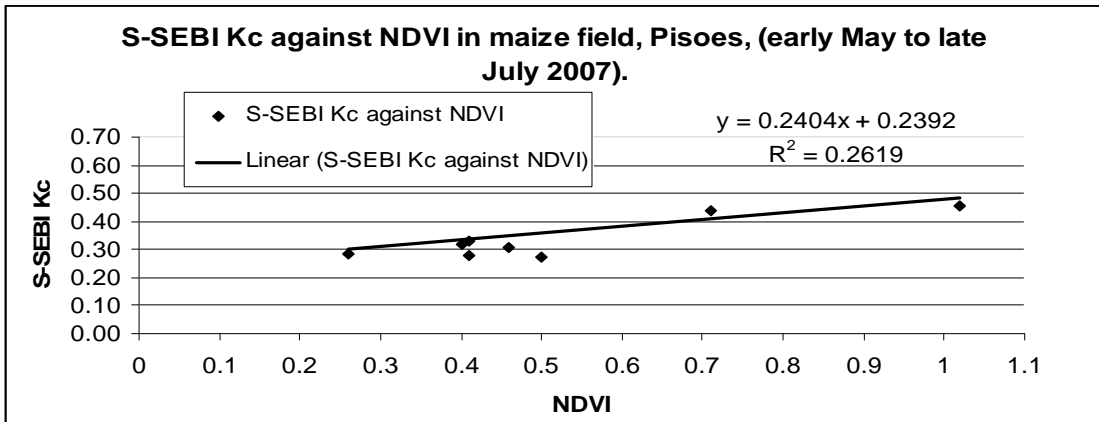


Figure 27: Relationship between S-SEBI Kc and NDVI in maize field, Pisoes (early May to late July 2007)

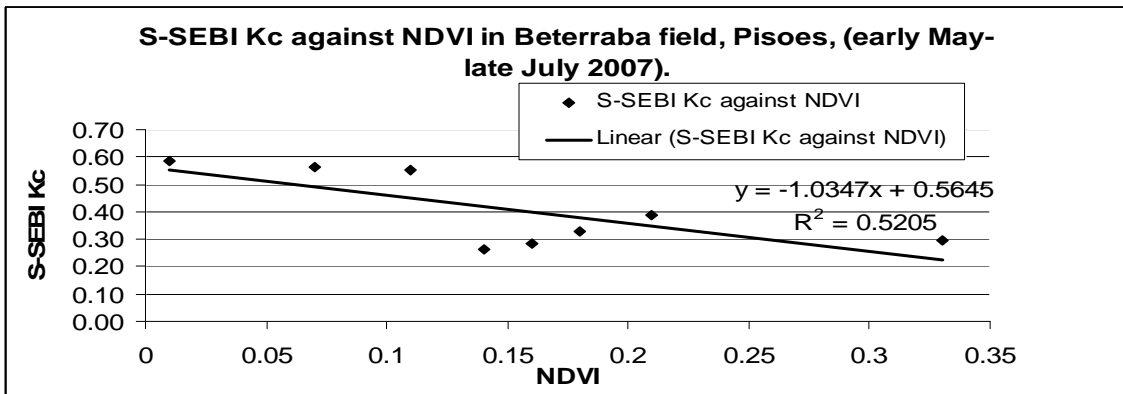


Figure 28: Relationship between S-SEBI Kc and NDVI in beterraba field, Pisoes (early May to late July 2007)

With respect to S-SEBI Kc and soil moisture, (see figures 28 and 29), no relationship was obtained in beterraba and maize (Pisoes) fields both in surface layer and depth averaged soil moisture. These unexpected observations are similar to those earlier observed between soil moisture with S-SEBI ET, and the same explanation suffices.

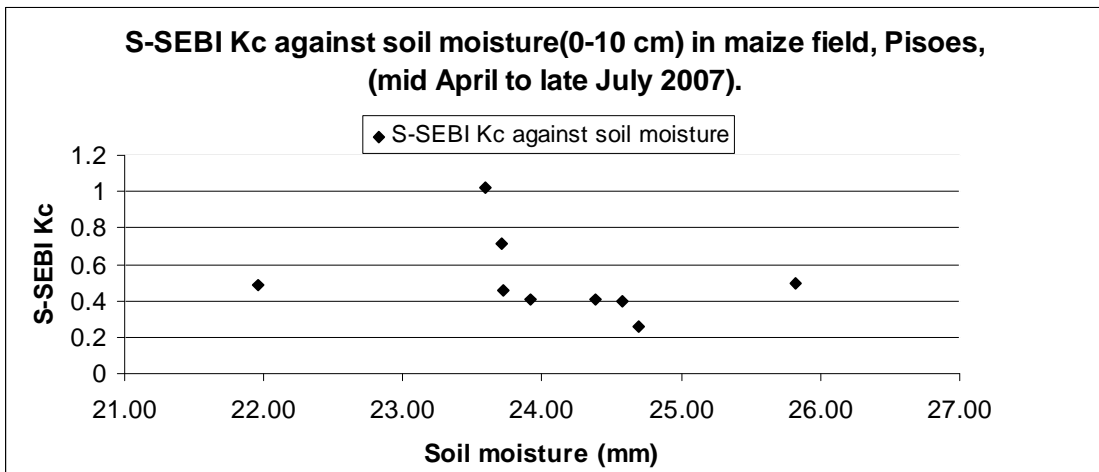


Figure 29: Relationship between S-SEBI Kc and soil moisture (surface layer: 0-10 cm) in maize field, Pisoes, (mid April to late July 2007).

5.7.1.5. Results of the analysis of practical application of S-SEBI evapotranspiration and crop coefficient products

Practical application of S-SEBI estimates of ET and Kc were investigated in a selected wheat area, (see Fig. 4), with regard to spatial variability of the variable estimated, (see Fig. 30). During the period before January 2007, both ETo and S-SEBI ET estimates were low and resonating and the spatial variability expressed by coefficient of variation (CV) was moderate (CV about 56 % or $s=0.33$). According to (Duchemin 2006), when vegetation is unstressed, the ratio of actual evapotranspiration and reference evapotranspiration is on average 1 and can reach 1.2 and that actual ETa can exceed ETo as observed in Fig. 30. In (Allen and Fao 1998), its noted that during frequent wettings, the ratio may increase substantially, being a function of wetting interval and potential evaporation rate during initial and development. Moderate spatial variability during this period may possibly indicate the indiscriminate nature of evapotranspiration process when the vegetation cover is minimal and coupled by adequate moisture.

During subsequent period, S-SEBI ET increased steadily parallel to ETo peaking in mid-May. In this period the spatial variation increased to about 60% ($s=1.99$). In the period that followed, S-SEBI ET declined relative to ETo, (Mean Absolute Bias = 2.2mm/day). The spatial variation of S-SEBI ET was however very erratic during this period.

Although the relationship between S-SEBI ET on one hand and NDVI and soil moisture availability on the other hand had not adequately demonstrated the influence of the variability of crop cover types and soil moisture availability, these two factors could potentially have contributed to the increased variation of S-SEBI ET observed during the second period (mid January onwards).

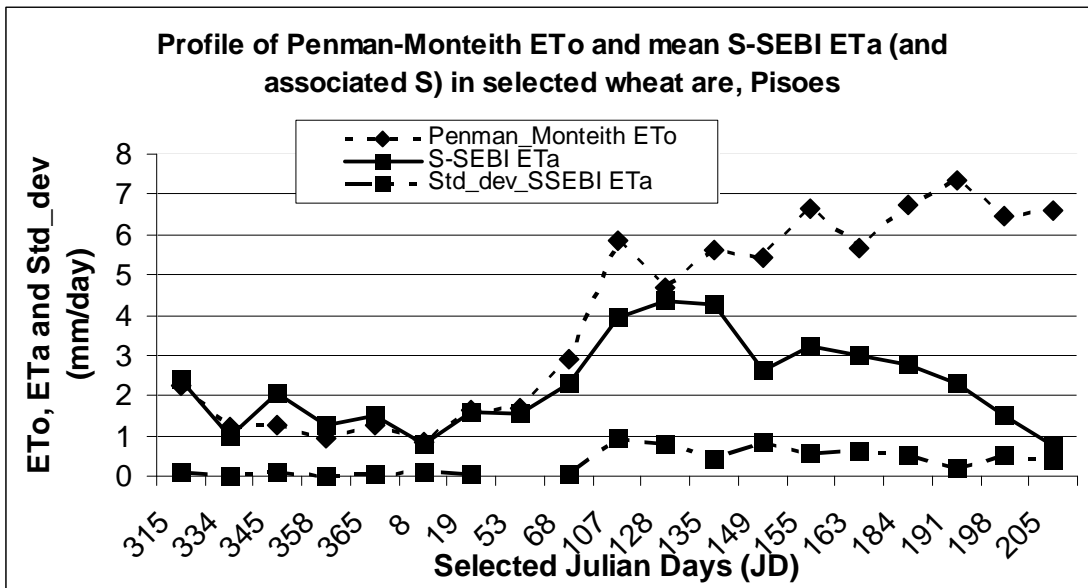


Figure 30: Temporal profile of Penman-Monteith ETo and S-SEBI ET (and associated standard deviation) in selected wheat field, Pisos, (October 2006- September 2007).

From the SSEBI- Kc profile (see Fig. 31), the trend is observed to break into four apparent junks. During the first period between October and early December 2006 (JD 278 through JD 345), S-SEBI Kc values increased, peaking at 1.6, and spatial variability was low (CV=11% and $s=0.2$). During the second period, mid December 2006 to mid April 2007 (JD 345 through JD 107), S-SEBI Kc gradually decreased to as low as 0.62. Spatial variation increased marginally during the period, though in JD 68, it was quite high (CV=42%). The period that followed, S-SEBI Kc increased, peaking at 0.92 (in JD 128=early May). In

subsequent period after JD 128, S-SEBI Kc gradually declined, coupled by declining spatial variability.

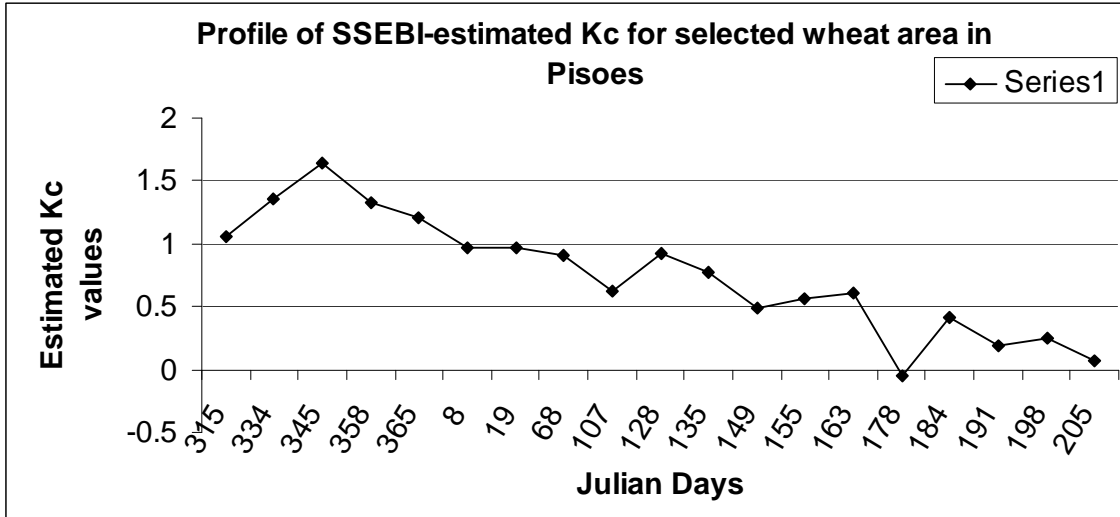


Figure 31: Temporal profile of S-SEBI Kc and associated spatial variation (CV) for selected wheat area, Pisoos, (Oct. 2006-Sep. 2007).

For any day within a specific growth phase-period, it was hypothesized that the phase-averaged S-SEBI-Kc multiplied by reference evapotranspiration (ET_o) would yield more accurate ET estimate than ‘traditional’ FAO 56 approach employing tabulated Kc values or K_{cr} (reflectance-based Kc, resolved spatially by vegetation indices). Characterization of S-SEBI Kc into distinct phases was based on NDVI profile that adequately captured the phenology of wheat growth (see Fig. 26).

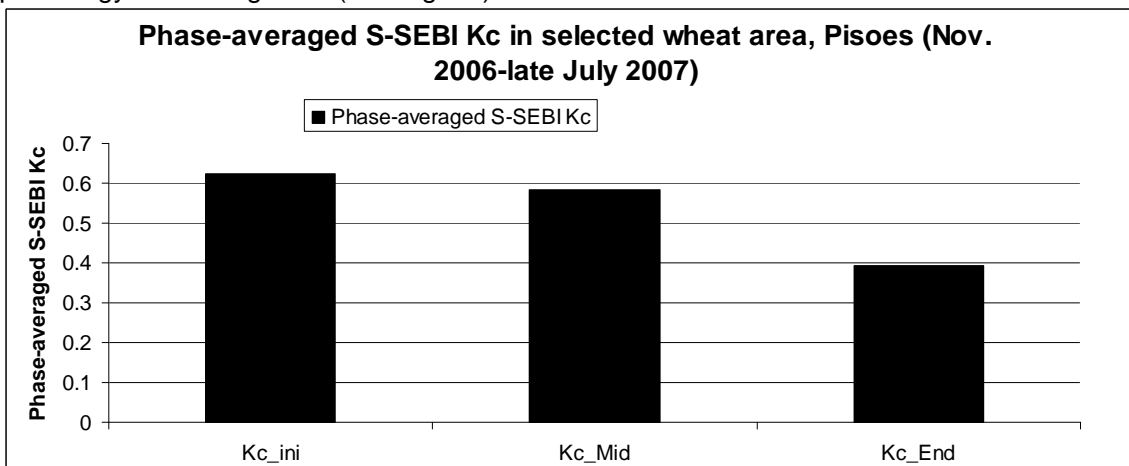


Figure 32: Temporal variation of phase-averaged S-SEBI Kc of winter wheat in Pisoos, (October 2006-late July 2007)

The obtained averages of S-SEBI-Kc values during the initial phase (JD 278 to 365), middle phase (JD 19 to 135) and end phase (JD 149 to 205) were 1.32, 0.70 and 0.32 respectively, (see Fig. 32). Estimated ET_c based on phase-averaged S-SEBI Kc is shown in Fig. 33.

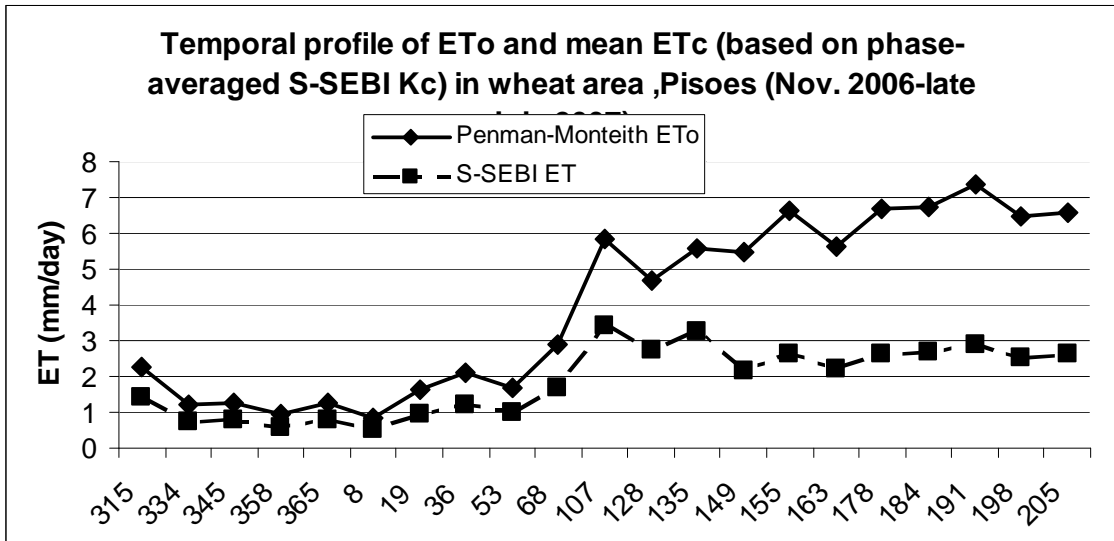


Figure 33: Temporal profile of ETc estimated based phase-averaged S-SEBI Kc applied into FAO 56 approach for winter wheat in PISOES, (October 2006-September 2007).

5.7.2. Evaluation of disaggregation procedure based on S-SEBI ET

Results of the comparison between estimates of Landsat TM and MODIS are presented first, followed in order by evaluation of the weighted ratio and disaggregation of original MODIS S-SEBI ET product and evaluation of spatial improvement.

5.7.2.1. Comparison of S-SEBI ET estimates derived from aggregated Landsat TM 5 with corresponding estimates from MODIS

On JD 68, the pattern of ET distribution was apparently similar in both aggregated Landsat TM and original MODIS estimates (see Appendices 11.5.1 and 11.5.2). Both of the images showed low ET rates around Beja City and high ET rates in selected fields. In Roxo, both images showed low ET rates in olive groves and moderate ET rates in rice and maize fields. However, from the histograms (see Appendix 11.5.3), apparent deviation of the estimates of the two sensors existed. By differencing the two estimates, the result indicated underestimation by MODIS sensor compared to Landsat TM, (ME/Bias=MAB=2.77 mm/day and RMSE=2.82 mm/day).

The observed deviation was attributed to the effect of spatial resolution of the two sensors, where the high resolution of Thematic Mapper captured peaks of even small area that were however blurred by the coarse resolution of MODIS derived ET map.

5.7.2.2. Results of evaluation of the weighted ratio derived from S-SEBI ET estimate of Landsat TM, JD 68

Based on equation 1, a ratio map obtained between ET map derived from original Landsat TM of JD 68 and its aggregation (simulated MODIS ET map) was multiplied to the aggregated ET map derived from Landsat TM map of JD 244. The output was a disaggregated S-SEBI ET of JD 244, (see Appendix 11.5.4), a blocky map of ET estimate. In (Vazifedoust 2007) and (Chemin 2004) ET images with 'blocky' structures was also observed. They noted that the 'blocky' structures only degrades the visual appearance while locally the values of the pixels are correct. It is more intense in areas where the aggregated Landsat TM map of ET does not satisfactorily represent the spatial pattern of ET.

Comparison of the disaggregated ET map with S-SEBI ET map derived from original Landsat TM map of JD 244 in terms of spatial distribution of ET values showed good agreement. This was further supported by their frequency histograms (mean=1.31 mm/day and 1.32 mm/day respectively, and standard deviation=1.69 mm/day and 1.05 mm/day respectively), indicating that the ratio map was of good quality. The scatter-plot indicated a high correlation between the two, (see Appendix 11.5.5). Statistical comparison further supported the observed agreement, having low ME/Bias, MAE and RMSE (-0.06 mm/day, 0.49 mm/day and 0.67 mm/day respectively).

5.7.2.3. Results of dissaggregation of original MODIS S-SEBI ET estimate and evaluation of spatial improvement

The ratio was also multiplied with the S-SEBI ET map derived from original MODIS of JD 68 as well as JD 334 and 184 in order to evaluate potential of enhancing spatial information by weighted ratio dissaggregation. Qualitative measure of dissaggregation procedure was by comparison of the output disaggregated maps, (see Appendix 11.5.6) with their original MODIS counterpart in terms of spatial distribution of ET. The spatial distribution of ET estimates was matching, showing good agreement between the original and disaggregated MODIS estimates. The scatter (Appendix 11.5.7) shows some degree of correlation.

Comparison of disaggregated MODIS ET (S-SEBI) estimate (JD 68) with original estimate of Landsat TM (JD 68) revealed deviation, with MODIS generally underestimating ET rates relative to Landsat TM estimates, (ME/Bias=-2.84, MAB=2.84 and RMSE=3.00 mm/day). Spatial variability of disaggregated S-SEBI ET estimates increased substantially in JD 334 by 11% but was insignificant in other days analyzed, (see Table 5).

Table 5: Analysis of spatial variability of S-SEBI ET estimates for original and disaggregated MODIS.

JD	ORIGINAL MODIS S-SEBI ET			DISAGGREGATED MODIS S-SEBI ET			Original Landsat TM		
	Mean	S	CV (%)	Mean	S	CV (%)	Mean	S	CV
334	1.63	0.18	11.04	1.62	0.35	21.6			
68	0.55	0.23	41.82	0.55	0.25	45.5	3.32	1.92	57.83
184	3.1	1.28	41.29	3.11	1.41	45.3			

6. Proposed Method of integrating remote sensing in Estimation of Reflectance-based Crop Coefficients and Soil Moisture Stress factor in Mapping Crop Evapotranspiration

6.1. Introduction

The framework of the proposed method is illustrated in Fig 34.

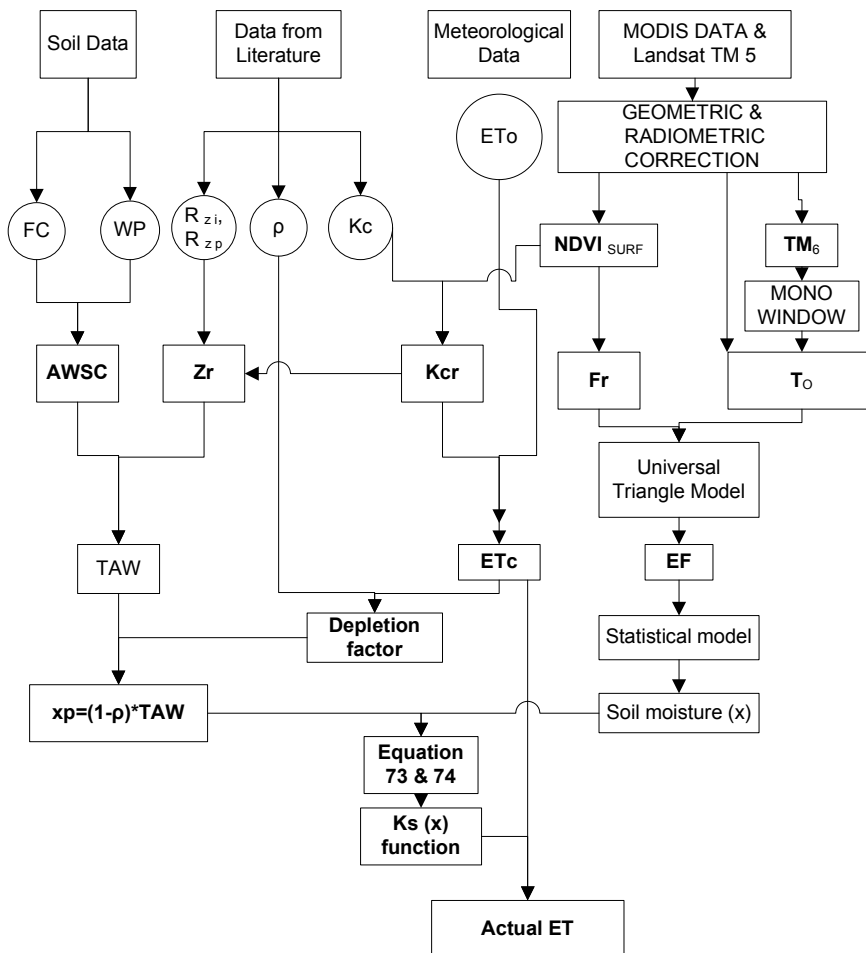


Figure 34: Flowchart of proposed scheme to obtain actual evapotranspiration

The scheme is based on equation 3 but make use of spatially resolved terms to yield spatially distributed ET products. It is initialized by definition of reflectance-based crop-coefficient (K_{cr}), specific to crop(s) being analyzed. Development of K_{cr} employs remotely sensed vegetation index (VI) as one of the main inputs. By combining K_{cr} with reference evapotranspiration (E_{To}) computed from meteorological data, spatially distributed crop evapotranspiration is obtained as the output. The next module takes into consideration the availability of soil water in the root zone. This is accounted by soil moisture stress factor (K_s) that is modelled and estimated spatially relative to soil moisture availability.

The scheme, integrating two spatially distributed modules, is expected to give a representation of actual field conditions in terms of crop evapotranspiration. In (Rossi 2007), it was noted that Kcr allow matching the crop coefficient with actual crop growth, and is sensitive to cases of anomalous climatic conditions and other stresses, being based on vegetation indexes and thus able to monitor photosynthetic activity.

In this study, implementation of the scheme followed logical steps of processing the remotely sensed vegetation index (sections 5.2.2 and 5.2.3) and subsequent characterization; estimating the reflectance-based crop coefficient (Kcr) and crop evapotranspiration (ETc), modelling and estimating soil moisture stress factor (Ks) and eventually evaluating actual evapotranspiration.

6.2. Spatial and temporal characterization of NDVI in selected wheat area

Based on the time series of estimated MODIS NDVI maps, representative values interior of the selected wheat area (Fig.4) are displayed in Fig. 35. The NDVI profile characterized the growth stage of the winter wheat, and agreeing with observations of (Martyniak 2007). The NDVI profile apparently depicted three distinct phases, in consistent with the phenological stages of winter wheat. The initial phase (JD 278 through JD 358), NDVI values were low. The middle phase (JD 36 through JD 135) NDVI values increased peaking at about 0.7. The final phase (JD 165 onwards) was similar to initial phase, having NDVI values as low as 0.2. In between these main phases were two transitional phases: the first between initial and middle phase (JD 365 through JD 19) having gradually increasing NDVI values; the second (JD 149 through 155) depicted by gradually declining of NDVI values.

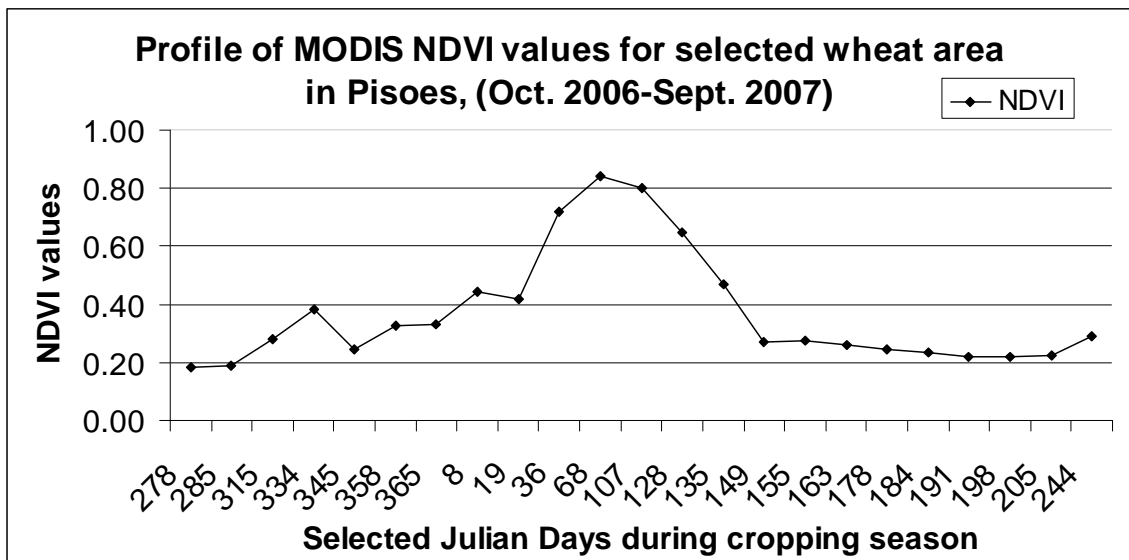


Figure 35: Temporal variation of NDVI for selected wheat area, Pisoos, (Oct. 2006-Sep. 2007).

Phase-average NDVI values were 0.31, 0.79 and 0.74, representing initial, middle and end phases respectively (see Fig. 36).

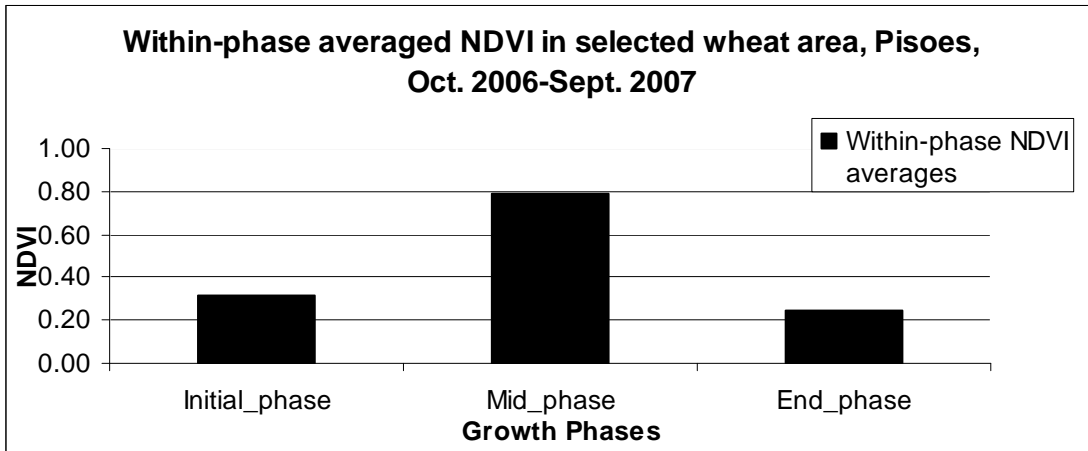


Figure 36: Within-phase averaged NDVI values for selected winter wheat area in Pisoes

6.3. Relationship between crop coefficient (Kc) and NDVI

Three procedures of developing “Reflectance-based Crop Coefficient” (K_{cr}) were investigated: FAO 56 K_c-NDVI time series approach, per-image NDVI-histogram approach, and relationship of NDVI and S-SEBI based K_c (SSEBI K_c-NDVI model).

6.3.1. FAO-56 K_c-NDVI time series modelling approach

NDVI-time series approach is based on the work of (Rossi 2007) and (Ray and Dadhwal 2001), and employ time series of remotely sensed vegetation indices. It is possible to model a vegetation index into a crop coefficient by means of a linear regression, thus obtaining reflectance-based coefficient (k_{cr}). The approach requires the general knowledge of what dominant crops are and of their growth stages at the time of data acquisition. Also required are crop coefficients relating to the crops in the image area.

In this study MODIS NDVI time series were employed. Characterization of the temporal NDVI profile over a homogenous crop field at a scale larger than the MODIS scale ((Rossi 2007)) was limited to the contiguous wheat area earlier identified, (see Fig.4). The model was established by relating the phase-averaged NDVI values to corresponding single crop coefficient (K_c) values, the latter assigned by consulting the K_c tables, ((Allen and Fao 1998)) under the appropriate crop development phase based on image acquisition date, (see Fig. 37).

A strong positive correlation (R²=0.85) was obtained and a fitted equation expressed as:

$$K_c = 0.0729 + NDVI * 1.399$$

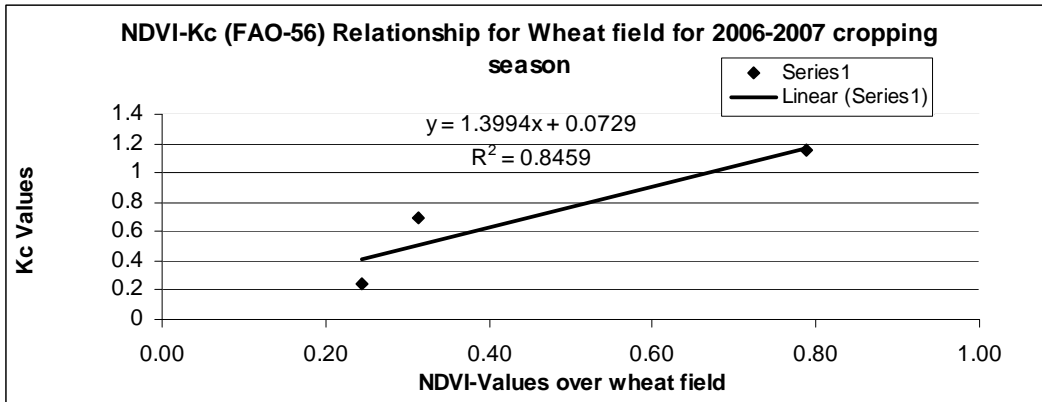


Figure 37: FAO 56 Kc-NDVI relationships based on NDVI time series approach

6.3.2. Per-image NDVI-histogram-FAO Kc modeling approach

The approach is based on the work of (Seevers 1994), and its unique advantage is that it eliminates the need for identifying each crop and determining the acreage of each. In addition, it does not require more than one image to build a NDVI-Kc model. However, like the previous approach, it does require the general knowledge of what dominant crops are and of their growth stages at the time of image acquisition. Also required are crop coefficients relating to the crops in the image area.

The approach involves building an empirical equation by means of linear transformation between maximum and minimum (NDVI) values (for each crop field known to be homogenous at a scale larger than the MODIS scale) and the FAO-56 tabulated k_c values for effective full cover and initial conditions (bare soil in crop fields). The procedure relies on the structure of the histogram of the NDVI values of the study area (see Fig. 38), to establish a linear relationship between the NDVI values and the crop coefficient values by assigning supplied crop coefficient values to their equivalent NDVI values. A point is defined on the histogram that is the beginning of NDVI values associated with the cropped land (bare soil in most cases) and is assigned a crop coefficient of zero. The value of the peak nearest the maximum NDVI values is assigned the crop coefficient of the predominant crop in the study area. The crop coefficient is determined by consulting the look-up tables under the appropriate date based on image acquisition.

The establishment of the two points on the histogram, each having an NDVI value and a crop coefficient, allows the calculation of an incremental value that represent an increase in crop coefficient defined by an increase of one in NDVI values. The form of expected regressions equations is similar to one applied by (Rossi 2007) and (Ray and Dadhwal 2001):

$$K_{cr} = a \text{ NDVI} + b$$

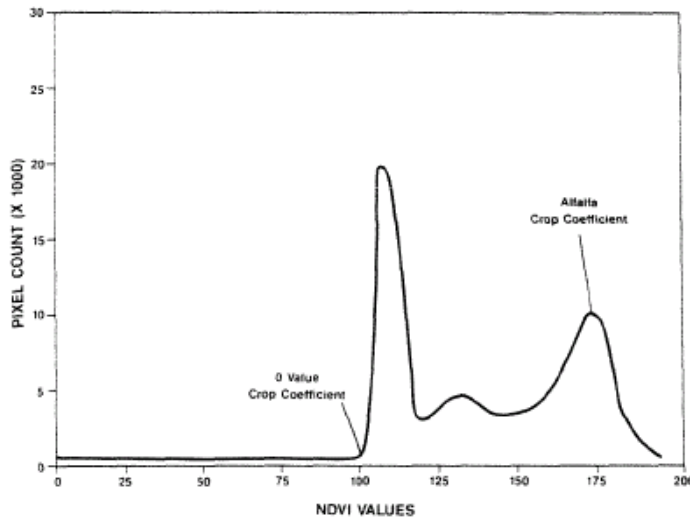


Figure 38: Histogram of NDVI values for a segment of the PVID showing crop coefficient labels at initial value and crop peak, based on 1988 data, (Adapted from [18]).

In this study, the MODIS NDVI histograms and two Landsat TM histograms over the selected wheat area were employed to implement this approach for selected days of interest. A database was constructed for minimum and maximum NDVI values for each day. To the minimum NDVI, a K_c value equal to zero was assigned according to the theory of this approach; while an appropriate K_c respect to the day of image acquisition was assigned to the maximum NDVI. The K_c values were plotted against NDVI values and a linear regression through the points performed, (see Fig. 39). Sets of fitted incremental equations/models of the form: $K_{cr} = a \cdot NDVI + b$ were obtained. Regression coefficients a and b of these relationships (see Table 6) are image specific.

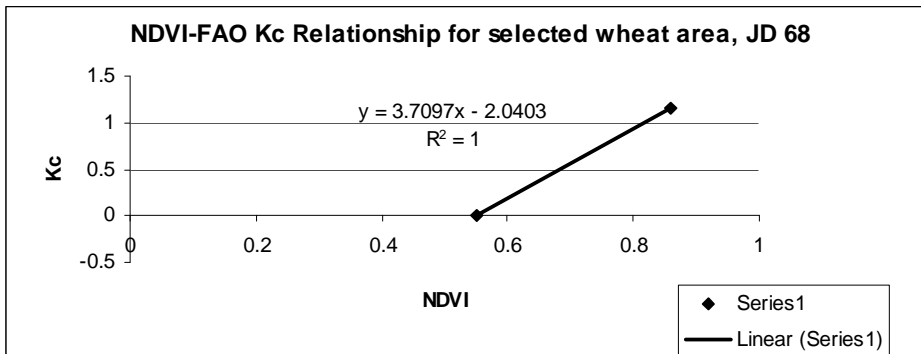


Figure 39: FAO 56 K_c -NDVI relationships based on per image histogram approach

Table 6: Regression coefficients a and b of per-image FAO-56 K_c -NDVI relationship

JD (DOY)	Growth Phase	a	b
334	Initial	1.7073	-0.4098
68	Mid	3.7097	-2.0403
184	End	1.5625	-0.3125

6.3.3. Relationship of NDVI and S-SEBI-based crop coefficient

Since energy balance models like SSEBI resolves the energy balance dependent on thermal channels (Tasumi and Allen 2007), the resolution of derived S-SEBI Kc maps correspond to that of thermal channel, in the case of MODIS being about 1000m and 120 m for Landsat 5 TM. Retrieval of values for both variables should theoretically be from fields with size twice the sensor resolution according to (Tasumi and Allen 2007). Typical field sizes in Pisoes/Roxo are smaller compared to such MODIS pixel size. Identification of such pixels was perhaps only possible for wheat in few areas, where farmers planted the crop in adjacent fields. Thus, as in other approaches, analyses of estimated variables were performed based on average values over the contiguous wheat area earlier identified, (see Fig. 4).

Possibility of modelling SSEBI-Kc by NDVI was investigated in section 5.7.1.4. For winter wheat, no relationship was observed when phase-averaged values of S-SEBI Kc (Fig. 32) were correlated with corresponding phase-averaged NDVI values, (Fig. 36). These was attributed to the influence of soil evaporation, which potentially introduced considerable scatter in the relation between the crop coefficient and NDVI, (Choudhury 1994).

According to (Tasumi 2005),Kc and NDVI have a clear relation during mid season, but no clear relation holds during periods having low ground cover due to large ranges in soil evaporation. Therefore, corresponding values of NDVI and S-SEBI Kc in the selected wheat area during the period of low vegetation cover were excluded in subsequent modelling effort. For the period between early May to late July, a positive relationship was obtained ($R^2=0.54$) and a fitted equation expressed as (see Fig. 40):

$$S-SEBI\ Kc_r = 0.5722 * NDVI + 0.0855$$

22

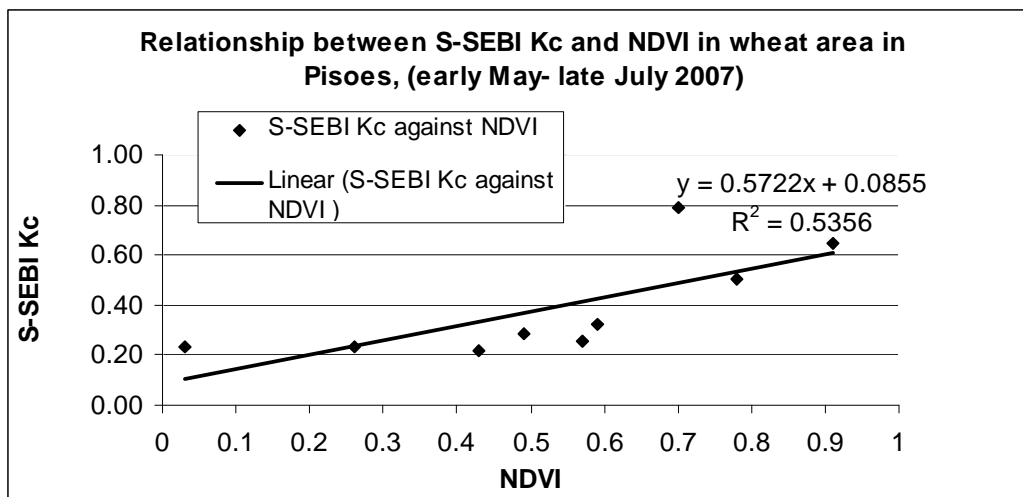


Figure 40: Relationship between S-SEBI Kc and NDVI in selected wheat area, Pisoes (early May to late July 2007).

The observed relationship during the second period, presumably when the crop cover was full, agrees with findings of (Tasumi 2005) due to the contribution of transpiration that very much relates with vegetation status. The observed scatter is attributed to instances of reduced root uptake associated with stress events, which could not immediately be detected by NDVI, since water shortage does not immediately affect the capacity of the canopies to absorb photosynthetically active radiation nor the structural properties of the plant,(Duchemin 2006).

6.4. Estimation of NDVI-based Kcr and crop evapotranspiration (ETc)

The established NDVI-Kc models were then stretched into NDVI maps (JD 334, 68, and 184) to obtain pixel-wise reflectance-based crop coefficient (k_{cr}) values for the selected wheat area. Subsequent evaluation of daily crop potential evapotranspiration (ET_c) for the selected days followed the normal FAO-56 procedure (equation 2), by multiplying Kcr by reference evapotranspiration (ET_o). ET_c represents the optimal amount of water that the crop needs to respond to atmospheric water demand.

6.4.1. Kcr and ETc estimates based on application of FAO 56 Kc-NDVI time series approach

Fig.41 shows a typical Kcr map obtained by application of FAO-56 Kc –NDVI time series approach. Table 7 give a summary of the statistics for the three days analysed.



Figure 41: Kcr based on FAO 56-NDVI time series: MODIS, JD 184

Generally, variability of Kcr was relatively low during the days analyzed, but apparently lowest in mid season, attributed to increased uniformity of NDVI.

Table 7: Summary statistics and spatial variability in reflectance-based crop coefficient (Kcr) in selected wheat field (based on FAO-56 Kc –NDVI time series approach)

Date	JD (DOY)	Growth Phase	Min	Max	Mean Kcr	Standard deviation	CV
30-Nov-07	334	Initial	0.45	1.01	0.68	0.13	19.12
09-Mar-07	68	Mid	0.84	1.27	1.09	0.13	11.93
03-Jul-07	184	End	0.35	0.58	0.45	0.07	15.56

Spatially distributed maps of ET_c were obtained when Kcr maps were combined with corresponding ET_o , (see Fig. 48). Table 8 present corresponding summary statistics.



Figure 42: ETc based on FAO 56-NDVI time series: MODIS, JD 184

Table 8: Summary statistics and spatial variability in ETc in selected wheat field (based on FAO-56 Kc –NDVI time series approach)

Date	JD (DOY)	Growth Phase	Min	Max	Mean ETc	Standard deviation	CV
30-Nov-07	334	Initial	0.54	1.21	0.82	0.16	20
09-Mar-07	68	Mid	2.44	3.68	3.15	0.38	12
03-Jul-07	184	End	2.36	3.91	3.04	0.34	45

Based on this approach, lowest ETc was observed in initial phase, and significantly increased over the next two phases. End phase had the highest rates. Variability of estimated ETc generally reflected variability of estimated Kcr.

6.4.2. Kcr and ETc estimates based on application of per-image NDVI-histogram approach

Fig.43 shows a typical Kcr map obtained by application of per-image NDVI-histogram approach. Table 9 give a summary of the statistics for the three days analysed.



Figure 43: Kcr based on Per-image approach: MODIS, Kcr, JD 68

Table 9: Summary statistics and spatial variability in reflectance-based crop coefficient (Kcr) in selected wheat field (based on per-image NDVI-Histogram approach)

Date	JD(DOY)	Growth Phase	Min	Max	Mean Kcr	Standard deviation	CV
30-Nov-07	334	Initial	0.05	0.73	0.33	0.16	48
09-Mar-07	68	Mid	0.01	1.13	0.67	0.33	49
03-Jul-07	184	End	0	0.25	0.09	0.06	67

The obtained Kcr estimates were relatively low and with high variability compared to those obtained using FAO 56 Kc-NDVI time series approach. Kcr maps obtained from per-image histogram approach were later employed to estimate crop ETc maps, (see Fig. 44). Table 10 present corresponding summary statistics.



Figure 44: ETc based on Per-image approach: MODIS, ETc, JD 68

Table 10: Summary statistics and spatial variability ET_c in selected wheat field (based on per-image Histogram approach)

Date	JD(DOY)	Growth Phase	Min	Max	Mean ET _c	Standard deviation	CV
30-Nov-07	334	Initial	0.06	0.88	0.4	0.19	48
09-Mar-07	68	Mid	0.03	3.28	1.95	0.96	49
03-Jul-07	184	End	0.02	1.74	0.63	0.39	62

The estimated ET_c rates were significantly low and with high variability than those obtained by FAO 56 K_c-NDVI time series approach.

6.4.3. K_c and ET_c estimates based on application of S-SEBI K_c-NDVI model

Fig.45 shows a typical K_c map obtained by application of S-SEBI K_c-NDVI model. Table 11 give a summary of the statistics for the days analysed.

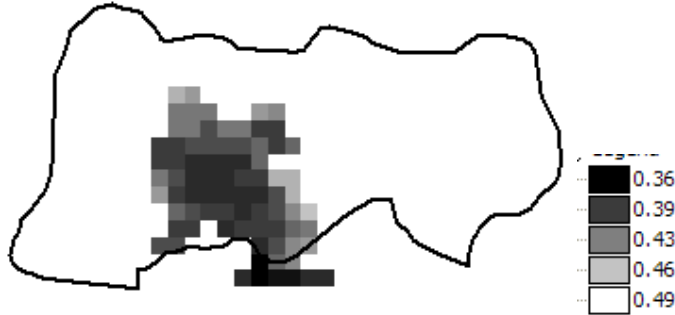


Figure 45: K_c based on S-SEBI K_c-NDVI model: MODIS, JD 184

Moderate K_c values were estimated in mid season (JD 68) and low values in end phase (JD 184). In both occasions, variability was generally low.

Table 11: Summary statistics and spatial variability in reflectance-based crop coefficient (K_c) in selected wheat field (based on S-SEBI K_c-NDVI model)

Date	JD (DOY)	Growth Phase	Min	Max	Mean SSEBI-K _c	Standard deviation	CV
09-Mar-07	68	Mid	0.63	0.88	0.77	0.08	10
03-Jul-07	184	End	0.36	0.49	0.42	0.04	9
01-Sep-07_MODIS	244	End	0.34	0.47	0.41	0.04	10
01-Sep-07_TM	244	End	0.2	0.69	0.43	0.12	28

Estimated K_c maps were then employed to estimate crop ET_c maps for selected days of interest, (see Fig. 46). Table 12 present corresponding summary statistics.



Figure 46: ET_c based on S-SEBI K_c-NDVI model: MODIS, JD 184

Estimated ET_c rates in JD 68 and 184 were quite similar, moderate and with low variability in both occasions.

Table 12: Summary statistics and spatial variability in crop ET_c in selected wheat field (based on S-SEBI Kc-NDVI model)

Date	JD (DOY)	Growth Phase	Min	Max	Mean SSEBI-ET _c	Standard deviation	CV
09-Mar-07	68	Mid	1.83	2.55	2.23	0.23	10
03-Jul-07	184	End	2.38	3.26	2.72	0.2	7

6.5. Comparison of K_{cr} and ET_c estimates from the three procedures

Preliminary comparison of the K_{cr} estimates derived from the three variants of reflectance-based approach (see Fig.47) showed that per-image histogram approach (Procedure 2) yielded the lowest estimate, whilst detected variability was often high. Estimates of FAO 56 Kc-NDVI time series approach (Procedure 1) and S-SEBI Kc-NDVI model (Procedure 3) apparently matched closely in JD 184,(0.45 and 0.42 respectively), but differed substantially in JD 68, (1.09 and 0.77). Variability was generally low in the two procedures.

Comparison of ET estimates show similar results, (see Fig. 48). Per-image histogram approach yielded the lowest estimate, whilst detected variability was often high. Estimates of FAO 56 Kc-NDVI time series approach and S-SEBI Kc-NDVI model matched closely in JD 184,(3.04 mm/day and 2.72 mm/day respectively), but differed substantially in JD 68, (3.15 mm/day and 2.23 mm/day). Again, variability was generally low in the two procedures.

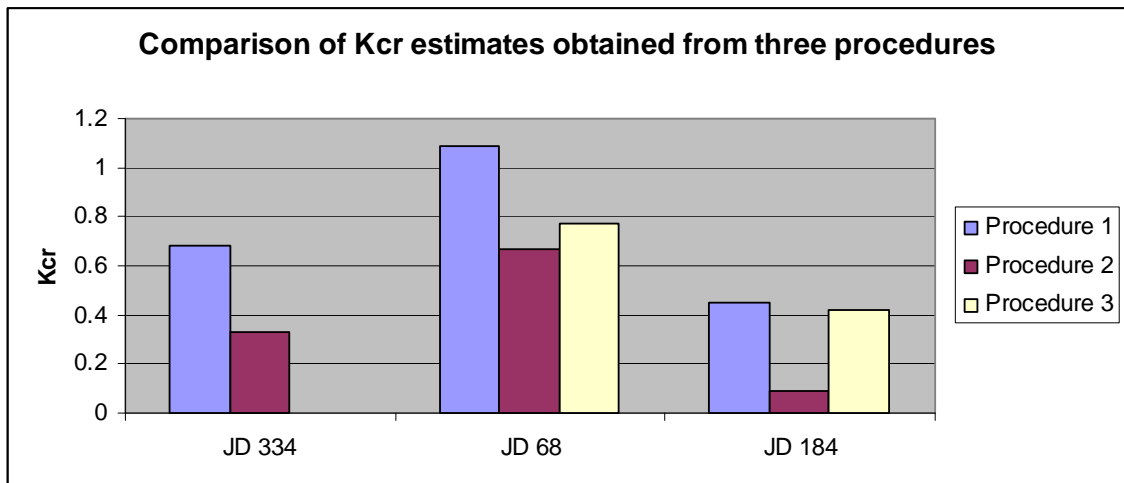


Figure 47: Comparison of K_{cr} estimates obtained from the three variants of reflectance-based approach.

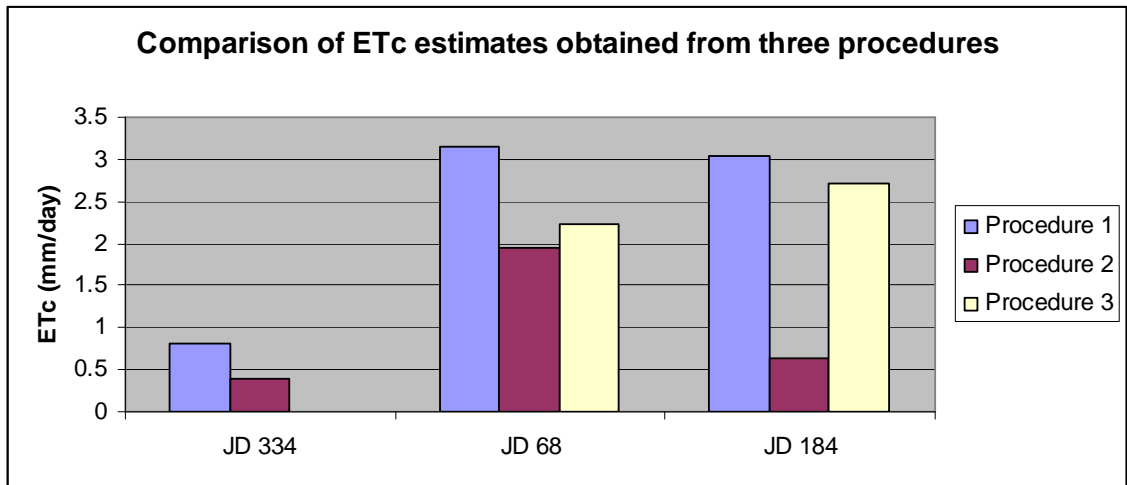


Figure 48: Comparison of ETc estimates obtained from the three variants of reflectance-based approach.

6.6. Remote sensing-based estimation of soil moisture stress factor (Ks)

According to (Beyazgul, Kayam et al. 2000), in calculation of actual crop evapotranspiration, limitations in root water uptake as a result of water shortage in the soil must be considered. In this way, actual crop water use would be evaluated under real conditions and the results could be utilized efficiently for the irrigation scheduling and optimal management of the available water resources, (Kotsopoulos 2003).

Soil water stress affects plant transpiration, (Er-Raki 2007). According to (Scott, Bastiaanssen et al. 2003), moisture that is transported to allow transpiration through the canopy originates throughout the vegetative zone and that difference in actual and potential evapotranspiration is caused by soil water stress.

6.6.1. Theoretical basis of estimation of Ks

Soil moisture stress factor (Ks) is employed as a linear soil water availability function in evaluation of actual evapotranspiration from crop potential evapotranspiration, (Kotsopoulos 2003). In this study, estimation of spatially distributed Ks integrated several steps, as schematized in the Fig.34. A three step process was followed in modelling and estimating Ks spatially. Evaporative fraction was estimated as a function of scaled surface temperature and NDVI. Depth-averaged root-zone soil moisture was then estimated by employing a statistical model relating soil moisture as a function of evaporative fraction. The linear function of Ks-soil moisture was finally resolved. Validation was in form of comparison of estimated soil moisture with ground-measured values.

6.6.1.1. Estimation of Evaporative fraction and depth-averaged soil moisture

Spatially distributed depth-averaged soil moisture (x) is determined from evaporative fraction (EF) based on a statistical model, expressed as:

$$(x)=f(EF) \quad 23$$

where f is the statistical model of estimating soil moisture as a function of evaporative fraction (EF). EF can be obtained from remotely sensed data following 'Universal Triangle Method', (Gillies, Kustas et al. 1997). This is based on the proved relationship between scaled NDVI and Land Surface Temperature and the EF, (Carlson 2007). This relationship, exemplified in Fig. 49, is build on the basis of physical interpretation of remotely sensed observations derived NDVI and surface radiant temperature when plotted as scatter plots, (Gillies, Kustas et al. 1997).

The limits defined by the feature space are referred to respectively as $NDVI_o$, $NDVI_s$, the cold edge (T_c (NDVI)) or T_o and the warm edge (T_w (NDVI)) or T_s and their scaled forms are defined as per equations 24, 25 and 26 respectively. Scaling is necessary when images from several days are to be compared because absolute values of NDVI tend to vary temporally in a non-systematic manner (Gillies, Kustas et al. 1997). According to (Carlson 2007) scaled variables have their coordinate axes varying from 0 to 1.0 regardless of the amount of net radiation or ambient air temperature. Scaling also reduces the sensitivity of Fr (and probably T^*) to atmospheric correction, and helps to isolate cloud and water pixels which tend to be outside the triangle.

$$NDVI^* = (NDVI - NDVI_o) / (NDVI_s - NDVI_o) \quad 24$$

$$Fr = ((NDVI - NDVI_o) / (NDVI_s - NDVI_o))^2 \quad 25$$

$$T^* = (T - T_o) / (T_s - T_o) \quad 26$$

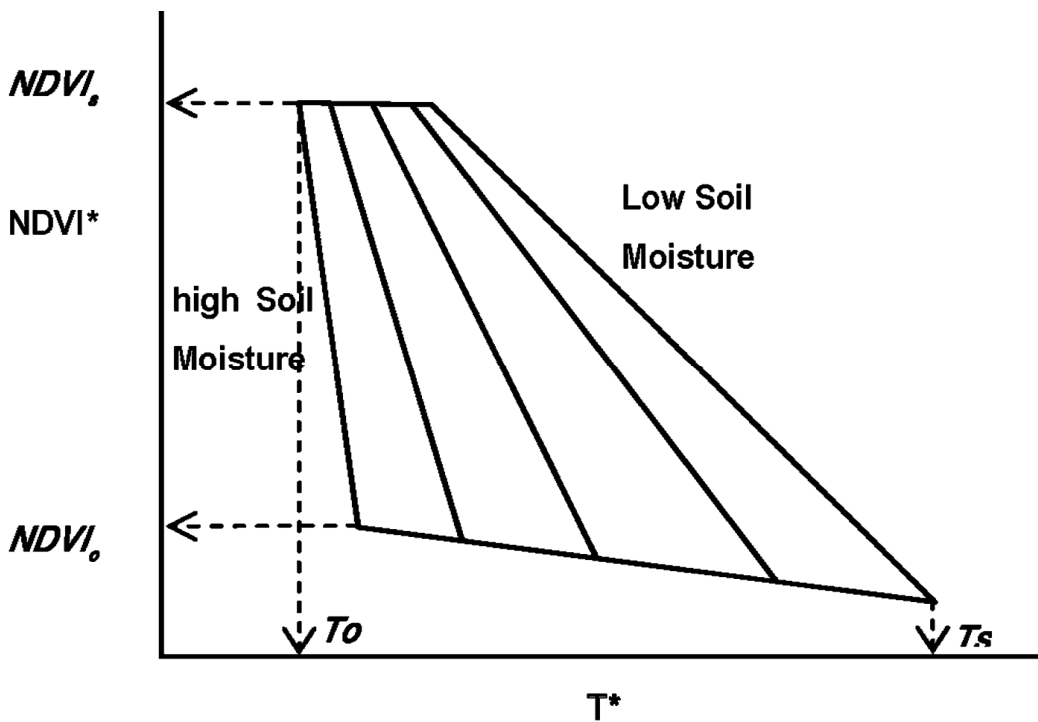


Figure 49: Universal Triangle relationship between soil moisture, temperature and NDVI, source(Wang 2007).

The scaled variables are inputs to polynomial equation to solve evaporative fraction (EF) and surface soil moisture, such as one defined by (Carlson 2007).

$$(Mo, EF) = \sum_{i=0}^3 \sum_{j=0}^3 a_{ij} T^{*i} Fr^j$$

27

where subscripts i and j pertain to the land surface temperature T^* and the fractional vegetation cover, Fr . According to (Carlson 2007), the triangle method, works with any reasonable land surface model. In essence, the model is used once to create a matrix of T^* and EF values for an entire range of input Fr and surface soil moisture availability values, given a fixed set of ancillary input variables such as surface albedo and stomato resistance. Simsphere, (<http://www.agry.purdue.edu/climate/dev/Simsphere.asp>), a SVAT model, was employed by (Carlson 2007) and third order polynomial generated to calculate surface soil

moisture and EF for all pixel values. The coefficients for the two surface parameters are given in the Table 13. According to (Carlson 2007), the relationship is sufficiently accurate and convenient to use where a suitable SVAT model is not available and requires relatively little expense in compute time or human resource in processing large images.

Quantitative assessments of depth-averaged soil moisture using crop water stress parameters as intermediate variables has been experimented by (Scott, Bastiaanssen et al. 2003), where approximation of volumetric soil moisture was obtained using a statistical relationship (f in equation 23) between moisture (x) and evaporative fraction (EF) (as Λ) that was independent of soil and vegetation type. The derived standard regression curve (for non-normalized data) is expressed as:

$$\Lambda = 0.421 \cdot \ln(x) + 1.284 \quad 28$$

With normalized soil moisture data between 0 (oven dry) and 1 (full saturation), the equation is expressed as:

$$\Lambda = a + b \cdot \ln(x/x_{\text{sat}})$$

Or

$$x/x_{\text{sat}} = \exp[(\Lambda - a)/b] \quad 29$$

where a and b are curve-fitting parameters, and $a=1.0$ (for normalized soil moisture); and $b=0.421$. Normalization allows the empirical function to be applied to a wider range of soil types as it exclude soil specific limits such as saturated soil water content and dry bulk density.

Table 13: Coefficients of the polynomial relationship for EF between T* and Fr as specified in equation 27

$(EF) = \sum_{i=0}^3 \sum_{j=0}^3 a_{ij} T^{*i} Fr^j, r^2=0.9993, RMSE=0.017$				
a_{ij}	$j=0$	$j=1$	$j=2$	$j=3$
$i=0$	0.8106	-0.5967	0.4049	-0.0740
$i=1$	-0.8029	0.7537	0.0681	0.2302
$i=2$	0.4866	1.2402	-0.9489	-0.8676
$i=3$	-0.3702	-1.3943	-0.7359	0.3860

6.6.1.2. Spatially distributed root depth (effective), available water storage capacity and total available water

Consideration for linear soil water availability requires quantified soil water storage or available soil water and availability coefficient of water to the crop. This approach has been regarded as suitable for heterogeneous irrigation applications because it can be used to characterise upper and lower limits for selected key locations within the root system.

Total available water (TAW) refers to the total amount of water that is stored in the soil within the plant's root zone. It is determined by soil texture and crop rooting depth. TAW is determined as:

$$TAW \text{ (mm)} = R_z \text{ (m)} * AWSC \text{ (mm/m)} \quad 30$$

where R_z crop rooting depth (m) and AWSC available water storage capacity of soil (mm/m). Soil parameters required to determine available water storage capacity (AWSC) include the soil moisture at field capacity (FC) and wilting point (WP), specific to the soil texture under consideration. In volumetric basis (vol), AWSC at a given component/sampling point is the residual of the two parameters, expressed as:

$$\text{Component_AWSC [vol]} = \theta_{FC} - \theta_{WP} \quad 31$$

For any layer being analyzed, conversion to depth of water per depth of soil is performed by multiplying the volumetric water content expressed as a decimal fraction by the layer depth, as;

$$\text{Component_AWSC [mm/m]} = \text{Layer depth} * \theta_{FC} - \theta_{WP} \quad 32$$

Weighted mean value of AWSC [mm] for a given map unit/soil textural class is resolved by weighting the component / sampling point profile values as;

$$\text{Mapunit_AWSC [mm]} = \frac{\text{sum} ((\text{Fraction_within class total}) * \text{component_AWSC [mm]})}{\text{sum} (\text{Fraction_within class total})} \quad 33$$

The root depth (R_z) is crop dependent ((Allen and Fao 1998)). According to (Jayanthi, Neale et al. 2007), it is estimated as a linear function of crop coefficient (between planting and maturity) using the following expression:

$$R_z = R_{z_i} + (R_{z_p} - R_{z_i}) * \left\{ \frac{(K_{crf} - K_{ci})}{(K_{cp} - K_{ci})} \right\} \quad 34$$

where R_z and K_c are the root depth and crop coefficient, subscripts i and p indicate initial and peak values, respectively. K_{crf} is reflectance-based crop coefficient. The minimum rooting depth is the effective rooting depth during the initial stage from which the germinating seed can extract water.

6.6.1.3. Availability coefficient of water to the crop/depletion fraction (ρ)

The parameter ρ depends on the crop species and the prevailing weather conditions which formulate the magnitude of the crop potential evapotranspiration, ET_c (mm/day) and for daily intervals is estimated as (Kotsopoulos 2003):

$$pd = \rho + 0.04 * (5 - ET_c) \quad 35$$

Where pd is the modified value of ρ . The values of ρ for the various crops is obtained from tables ((Allen and Fao 1998)). ET_c is the crop potential evapotranspiration at the day (mm/day).

6.6.1.4. Soil moisture stress coefficients (K_s)

To determine any change of actual evapotranspiration over time (t), equation 3 takes into account the available soil moisture in the root zone, x , and is modified as follows (Kotsopoulos 2003):

$$ET_a(x,t) = K_s(x) * ET_c(t) \quad 36$$

$K_s(x)$ may be linear of the following form, (Ortega, de Juan et al. 2005) and (Kotsopoulos 2003):

$$K_s(x) = 1 \quad \text{when } x_p < x < \text{TAW} \quad \text{and} \quad 37$$

$$K_s(x) = x/x_p \quad \text{when } 0 < x < x_p \quad 38$$

Where $x_p = (1 - \rho) * \text{TAW} = \text{readily available water [RAW]}$ 39

TAW is available soil water in the root zone (mm) and p is parameter expressing the average fraction of total available water that can be depleted from the root zone before moisture stress occurs (Kotsopoulos 2003).

$K_s(x)$ function is then resolved respectively for the condition of high moisture status (Equation 37), and for low moisture status condition (Equation 38) and finally linked to equation 36 to obtain actual crop evapotranspiration.

This method of accounting for water deficit is similar to that applied by (Ortega, de Juan et al. 2005) for effecting management strategies for deficit irrigation.

6.6.2. Implementation of the K_s estimation scheme

The proposed scheme was implemented for both MODIS and Landsat TM data over selected days of interest, by executing preceding systems of equations over selected days for analysis, (JD 334, 68 and 184).

6.6.2.1. Evaporative fraction based on 'Universal Triangle' model

In order to estimate evaporative fraction, NDVI maps were resampled to match the LST pixels and the two maps crossed and eventually rescaled using equations 24, 25, and 26. The two parameters were employed in calculating evaporative fraction (UM-EF) based on the polynomial model expressed in equation 27 and coefficients in Table 13, (see Fig. 50).



Figure 50: Maps of Evaporative Fraction, estimated using Universal Triangle model (equation 27 and Table 16).

Appendix 12 present the summary statistics in wheat area for the selected days. Variability of UM-EF in wheat area was low.

Comparison of UM-EF against EF estimates of S-SEBI model is illustrated by Fig. 51. In all the three days analyzed, the estimates were comparable, (RMSE=0.11), indicating the plausibility of the 'Universal Triangle' model.

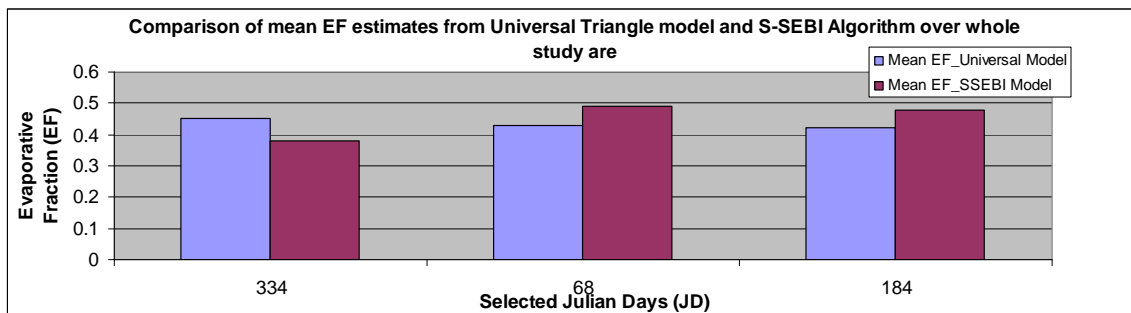


Figure 51: Comparison of EF estimated by 'Universal Triangle' model against estimates of S-SEBI model

6.6.2.2. Depth-averaged soil moisture

The statistical model expressed in equation 29 for normalized soil moisture data was then stretched over estimated EF maps, to obtain volumetric soil moisture. Conversion to depth of water per depth of soil was performed by multiplying the volumetric water content expressed as a decimal fraction by 700mm, the depth interval considered appropriate for wheat, and over which historical moisture data was available (Appendix 2). Fig. 52 show a typical map of depth-averaged soil water content with dimensions as mm/cm³.

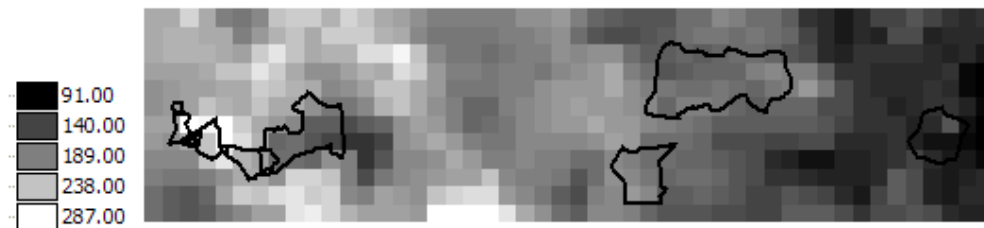


Figure 52: Depth-averaged soil moisture (mm/cm³), MODIS, JD184

Appendix 13 present the summary statistics in wheat area for the selected days. Variability of estimated depth-averaged soil moisture was again very low in wheat area.

Comparison of depth-averaged soil moisture estimated by remotely-sensed data against ground-based measurements collected from fields in Pisos is illustrated by Fig. 53. The model estimates were extracted from pixels corresponding to the fields from which ground-based moisture measurements were collected, (Appendix 4). The estimates were plausible, slightly overestimating the moisture level. In JD 68 and 184, the estimates were comparable in terms of bias, mean absolute error (MAE) and RMSE (9.38 mm, 9.38 mm, and 10.6 mm respectively).

Determination of AWSC employed the soil water holding characteristic data provided in Appendix 2. At each soil sample collection point, AWSC (mm/m) was calculated based on equations 31 and 32, but for only the horizons not deeper than 100cm considered as the effective vegetative zone of most annual crops. The sum of these was calculated as AWSC for that component/sampling point, representing the amount of water an increment in soil depth can store.

Using the Pisos soil map (Appendix 1), within-soil class AWSC values was calculated through weighted averaging based on equation 33. Where only one sample point/ component existed, the AWSC value was directly taken as representative value for that soil class. The value map was then rasterized to obtain respective AWSC maps, (see Appendix 14).

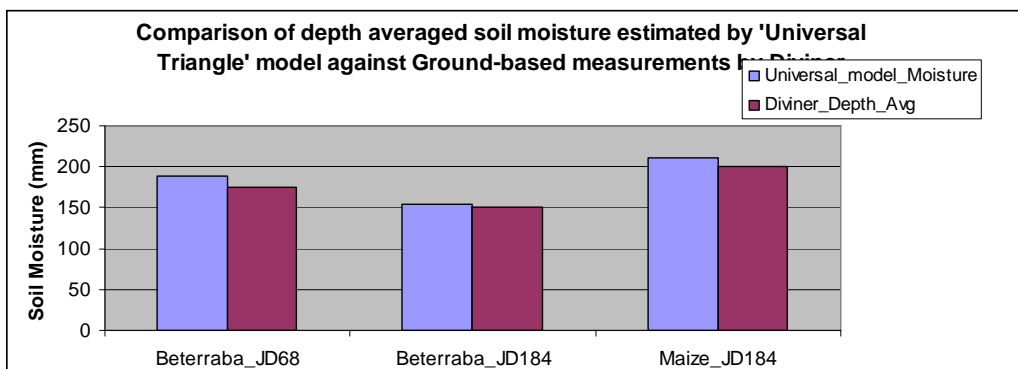


Figure 53: Comparison of depth-averaged soil moisture estimated by 'Universal Triangle' model against ground-based measurements

Estimation of root depth for winter wheat crop was determined based on equation 34. Maximum effective rooting depth ($R_{z_p} = 1.8\text{m}$) was obtained from tables ((Allen and Fao 1998)) for the larger values for modelling soil moisture stress. The minimum rooting depth, being the effective rooting depth during the initial stage from which the germinating seed can extract water, was considered as $R_{z_i} = 0.1\text{ m}$, (Er-Raki 2007).

Initial K_{ci} and peak K_{cp} were determined from reflectance-based crop coefficient (K_{cr}) maps at JD 334 and JD 68 respectively (see section 6. 4). Based on Kc-NDVI time series approach $K_{ci} = 0.4$ (minimum value) and peak $K_{cp} = 1.27$ (maximum value). Based on the per image histogram approach, $K_{ci} = 0.2$ (mean value) and peak $K_{cp} = 1.13$ (maximum value). K_{cr} itself was the only variable input parameter in the equation, which was assigned for respective day of interest. Results of analysis of spatial variability of effective rooting depth obtained from three variants of reflectance-based crop coefficients approach is presented in Appendices 15.1, 15.2 and 15.3.

With AWSC and root depth maps ready, they were input into equation 30 to obtain Total Available Water (TAW) map, but for selected wheat area only. Again, estimates were specific to variants of the reflectance-based crop coefficients approach. Results of analysis of spatial variability are presented in Appendices 16.1, 16.2 and 16.3.

Determination of adjusted depletion fraction (p_d) employed equation 35, since the ET_c for the selected days of interest was not equal to 5 mm day^{-1} . ET_c was obtained earlier from the different reflectance-based crop coefficient approaches (section 6. 4). Parameter $\rho = 0.55$ was obtained from table ((Allen and Fao 1998)). The estimated depletion factor crop depended on the prevailing weather conditions which formulate the magnitude of the crop potential evapotranspiration, (ET_c), (Kotsopoulos 2003). Results of analysis of spatial variability are presented in Appendices 17.1, 17.2 and 17.3 for all the three variants of reflectance-based crop coefficients approach.

To allow resolving the linear relation between K_s and instantaneous soil moisture expressed by equation 37 and 38, fraction of TAW that is not readily available $(1-p)*TAW$ or x_p was calculated based on equation 39. These represent the water held by the soil matrix, the fraction of TAW that is not readily available. Results of analysis of spatial variability are presented in Appendices 18.1, 18.2 and 18.3 for all the three variants of reflectance-based crop coefficients approach.

Instantaneous soil moisture was then crossed with $(1-p)*TAW$ or x_p , to obtain indicative binary maps based on the conditions expressed by equations 37 and 38 obtained. The binary maps relate to soil moisture status in the root zone; a high moisture status mask corresponding to pixels with moisture above TAW fraction that is not readily available (x_p) and a low moisture mask would correspond to pixels with moisture below RAW threshold.

Once the soil moisture status binary were delineated, then it was possible to resolve for $K_s(x)$ function for the selected days of interest. Where estimated depth-averaged root zone moisture was more than $x_p (=TAW \text{ fraction not readily available})$, then $K_s(x)$ function was automatically taken as unity (1), based on equation 37. In cases where soil moisture was below the threshold, the $K_s(x)$ function was automatically computed as ratio of estimated soil moisture to (x_p), (equation 38). The analysis was specific to the three variants of reflectance-based crop coefficients approach, (see Appendix 19.1). It should be noted that the resolution of these outputs was about 1000 m , corresponding to MODIS estimates of depth averaged soil moisture.

The results of the analysis indicated that soil matrix had adequate water and did not constrain the plant from accessing the water at least in JD 334 and 184. In JD 68, however, there was an apparent soil moisture stress detected in isolated pixels based on FAO 56 Kc-NDVI time series approach. These pixels are located within "Franco-Argiloso" soil texture

class. As noted earlier, this soil class apparently has low available water storage capacity (AWSC) due to its combination of physical components. This may explain the apparent occurrence of soil moisture stress in this site.

$K_s(x)$ function estimated by FAO 56 Kc-NDVI time series approach on JD 68 was linked to the already calculated crop potential evapotranspiration according to equation 36 to obtain spatially distributed actual evapotranspiration. The resolution of the obtained estimate was about 1000m, (see Fig. 54). Based on analysis of spatial variability, estimated average value was 3.17 mm/day while variability was quite low (CV=11%). The lowest estimate (2.51 mm/day) occurred in the isolated pixel having low AWSC and therefore low readily available water.



Figure 54: Actual ET based on FAO 56 Kc-NDVI time series: MODIS, JD68

6.7. Dissaggregation of selected products of proposed method using weighted ratio approach

Evaluation of dissaggregation of ET_c (based on FAO-56 Kc-NDVI time series procedure) is presented in the preceding sections; first the comparison between estimates of Landsat TM and MODIS, followed in order by evaluation of the weighted ratio and then dissaggregation of original MODIS ET_c product and evaluation of spatial variability improvement. Results of dissaggregation of soil moisture distribution and x_p (distribution of unready available water in root zone) are presented in Appendices 20 and 21 respectively.

6.7.1. Comparison of ET_c estimates derived from (aggregated) Landsat TM 5 with corresponding estimate from MODIS

Aggregated Landsat TM and MODIS ET_c estimates based FAO-56 Kc –NDVI time series approach were compared qualitatively. Map representation of ET distribution pattern and frequency histograms are shown in Appendices 19.2.1 and 19.2.2 respectively.

From the maps, deviation in ET_c estimates in JD 68 is clearly apparent in the middle part of the wheat area. Estimates of MODIS are quite high compared to aggregated Landsat TM, (mean =3.29 and 2.80 mm/day respectively). By differencing the two estimates, the result indicated apparent overestimation by MODIS sensor compared to Landsat TM, (ME/Bias=-0.49, MAB=0.64 and RMSE=0.79 mm/day).

Based on similar comparison of estimates of JD 244, both the overall maps as well as the ET histograms matched each other quite well (mean =2.28 and 2.24 mm/day respectively). Statistical comparison in terms of mean error/bias, MAB and RMSE also showed good agreement between the reflectance-based ET from Landsat TM (aggregated) and ET from MODIS, (-0.05 mm/day, 0.26 mm/day and 0.32 mm/day respectively).

6.7.2. Evaluation of weighted ratio derived from Landsat TM estimates of reflectance-based ET_c (FAO 56-Kc-NDVI time series procedure), JD 68

Equation 1 was employed to obtain a weighted ratio derived from the Landsat TM estimate of reflectance-based ET_c of JD 68 and its corresponding aggregate map of 250m. Evaluation of the performance of the ratio applied the same procedures as applied in 5.7.2.2. The output disaggregated Landsat TM ET_c map of JD 244 is shown in Appendix 19.2.3 (left).

Comparison of disaggregated Landsat TM ETc map of JD 244 with that of corresponding ETc map from original Landsat TM map (Appendix 19.2.3) in terms of spatial distribution of ETc estimates showed slight deviation, with the former slightly overestimating the ETc rates. The frequency histograms showed good agreement, (ETc means =2.38 mm/day and 2.23 mm/day, and standard deviation=0.64 mm/day and 0.24 mm/day respectively).

The scatter-plot (Appendix 19.2.4) indicated a weak correlation between the two. This was attributed to the weighted ratio map used in the disaggregation, which was based on ETc map of March (JD 68) a period of full cover compared to September (JD 244) when wheat was already harvested.

Statistical comparison, however, showed low ME/Bias, MAE and RMSE (-0.02 mm/day, 0.39 mm/day and 0.50 mm/day respectively) apparently indicating good agreement between the disaggregated and original Landsat TM ETc map.

6.7.3. Disaggregation of original MODIS estimates of ETc and evaluation of spatial variability enhancement

The ratio was also multiplied with the ETc map derived from original MODIS of JD 68 as well as JD 334 and 184 in order to evaluate potential of enhancing spatial information by weighted ratio disaggregation. Qualitative evaluation of disaggregation procedure was by comparison of the output disaggregated maps, (Appendix 19.2.5-left) with their original MODIS counterpart (Appendix 19.2.5-right) in terms of spatial distribution of ET. The spatial distribution of ET estimates showed some degree of agreement; in both original and disaggregated MODIS, the south eastern part of the area had low ET rates, and relatively higher rates in the middle and north western part.

Scatter plot (see Appendix 19.2.6) of disaggregated MODIS ETc estimate against corresponding original estimate of Landsat TM of JD 68 showed high correlation between the two. However, further statistical comparison revealed deviation, with MODIS overestimating ETc rates, (ME/Bias=0.56 mm/day, MAB=0.68 mm/day and RMSE=0.84 mm/day). Disaggregation also increased the spatial variability of ETc in JD 334 significantly by 43%, but the increase was lower in the other days analyzed, (see Table 14).

Table 14: Analysis of spatial variability of ETc estimates (based on FAO 56 Kc-NDVI time series) for both original and disaggregated MODIS.

JD	ORIGINAL MODIS ETc			DISAGGREGATED MODIS ETc			Landsat TM		
	Mean	S	CV (%)	Mean	S	CV (%)	Mean	S	CV
334	0.82	0.16	19.51	0.91	0.57	62.6			
68	3.15	0.38	12.06	3.55	0.93	26.2	2.75	0.78	28.36
184	3.04	0.45	14.80	3.12	0.9	28.8			

7. Cross Analysis of the ET estimates of the different approaches

Mean evapotranspiration rates along the growth profile of winter wheat crop in Pisos estimated by three approaches- 'traditional' FAO 56, S-SEBI algorithm and based on phase averaged S-SEBI Kc- was compared (see Fig. 55). For three selected days (JD 334, 68 and 184), the mean ETc estimates obtained from the three variants of reflectance-based crop coefficient approaches in the same wheat area were also included for comparison. Profile of reference evapotranspiration (ETo) is also shown.

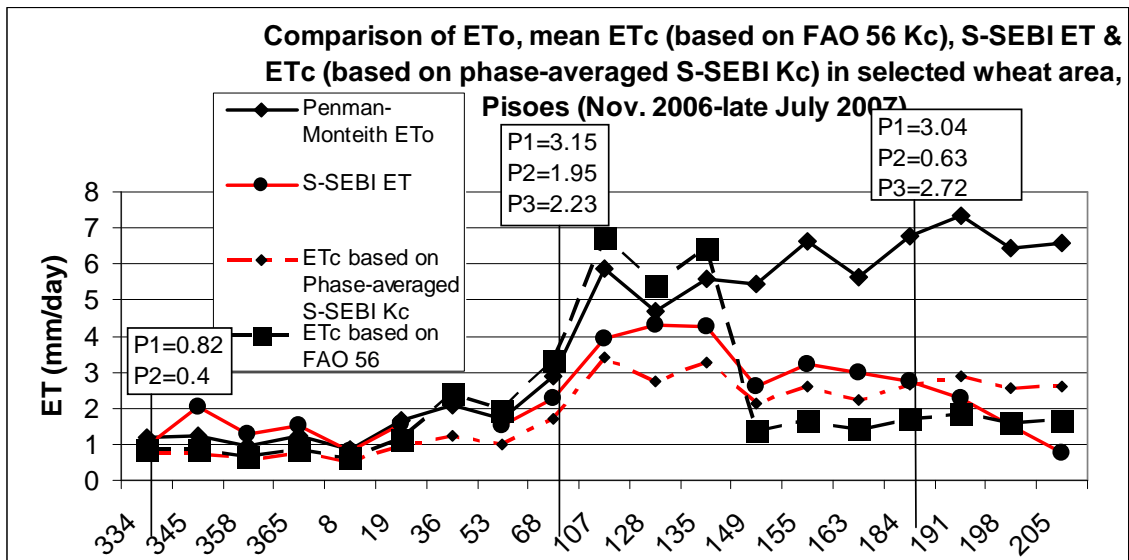


Figure 55: Profiles of S-SEBI ET, crop evapotranspiration (ETc) estimated using FAO 56 Kc and phase-averaged S-SEBI Kc and Penman-Monteith ETo, (Oct. 2006-Sep. 2007). P1, P2 and P3 are respectively FAO 56 Kc-NDVI time series approach, per image NDVI histogram approach and S-SEBI Kc-NDVI model.

During the initial period of the growth season-November 2006-January 2007- estimates obtained from S-SEBI model were relatively higher compared to those estimated by both FAO 56 and estimates based on phase-averaged S-SEBI Kc. During mid-season, FAO 56 estimates were quite higher than those obtained by both S-SEBI model and based on phase-averaged S-SEBI Kc. The latter two were matching closely. Overall deviation of FAO 56 ETc estimates from S-SEBI in terms of RMSE also showed significant deviation, (1.2 mm/day). Similar measure of deviation of ETc estimated based on phase-averaged S-SEBI Kc against S-SEBI ET showed improvement over those obtained using published FAO 56 Kc, (RMSE=0.90 mm/day).

The comparison was zoomed to mean evapotranspiration estimates of only three selected days-JD 334, 68 and 184- (see Fig. 56).

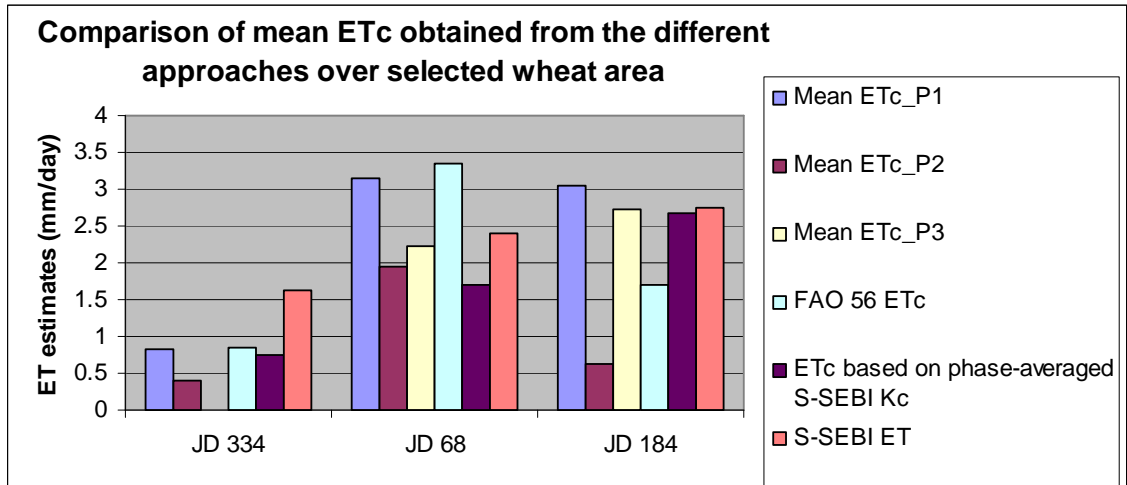


Figure 56: Comparison of crop ETc estimated by the approaches investigated. P1, 2 and 3 refer to respectively FAO 56 Kc-NDVI time series approach, per image NDVI histogram approach and S-SEBI Kc-NDVI model.

On JD 334 (during initial phase), mean evapotranspiration estimates of Procedure 1, 'traditional' FAO 56 and estimate based on phase-averaged S-SEBI Kc were comparable to S-SEBI ET estimates. Procedure 2 was least accurate. On JD 68 (during mid phase), mean estimates of Procedure 2, Procedure 3 and estimate based on phase-averaged S-SEBI Kc were comparable to S-SEBI ET estimates. However, estimates of Procedure 1 and 'traditional' FAO 56 were significantly overestimated relative to S-SEBI ET. On JD 184, mean S-SEBI ET matched with estimates of other approaches, apart from Procedure 2 and 'traditional' FAO 56 that underestimated evapotranspiration rates relative to S-SEBI ET.

Besides comparison of mean estimated evapotranspiration against corresponding S-SEBI estimates, error magnitude (in terms of bias, mean absolute bias, and RMSE) was evaluated, (see Appendix 22). The estimation error of the investigated procedures was low in JD 334 (phase) and high in JD 68 and 184, respectively mid and end phases.

Observed deviation may be attributed to nature of crop coefficient employed by the specific approach. Comparison of mean crop coefficient (see Fig. 57) depicted the same trend as the one observed with respect to comparison of mean evapotranspiration estimates. Also, evaluation of error magnitude (see Appendix 23) matches with the measured errors of evapotranspiration in Appendix 22.

In mid season, it seemed that S-SEBI based coefficient was more sensitive to the wet events and intermittent stress events, (Allen and Fao 1998), (Tasumi 2005) and (Duchemin 2006) than its published FAO 56 counterpart. The remarkable inadequacy of estimated Kcr of P1 in both initial and end phase (JD 334 and 184 respectively) may be attributed to the nature of the regression models earlier formulated (see section 6.3). For instance JD 334, the upper boundary of the model was very low and in effect, the output Kcr was evidently low. Estimated ETc was in turn underestimated. P 1 on the other hand had its model boundaries well stretched over the spectrum of NDVI profile. This may suggest the relatively better performance by this approach compared to P 2.

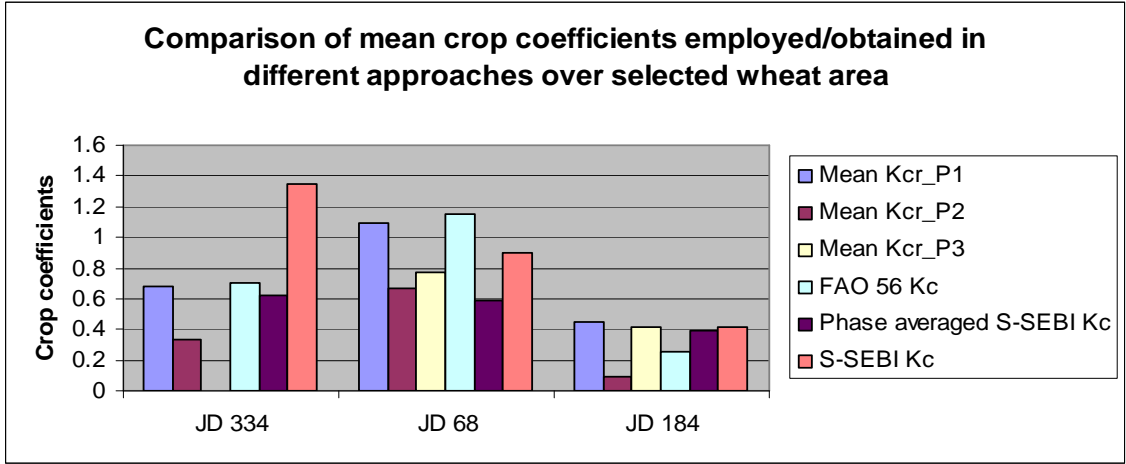


Figure 57: Comparison of crop coefficient employed/ obtained by the ET estimation approaches investigated. P 1, 2 and 3 refer to respectively FAO 56 Kc-NDVI time series approach, per image NDVI histogram approach and S-SEBI Kc-NDVI model.

8. DISCUSSION

This chapter discusses the proceedings and results of previous chapters and elaborates them in context of other similar studies. It is organized round the two hypotheses formulated earlier.

8.1. Performance of 'traditional' FAO 56 Approach and S-SEBI algorithm vis-à-vis the Proposed Method in estimation of Evapotranspiration

In chapter two, several methods of estimating evapotranspiration were elaborated. In this study, extreme but common approaches of estimating evapotranspiration were implemented: the 'traditional' FAO-56 model and Simplified Surface Energy Balance Index (S-SEBI).

FAO-56 approach proved simple, requiring only the determination of reference evapotranspiration (ET_o) and crop coefficient (K_c). Single crop coefficient published by (Allen and Fao 1998) were used. Single K_c integrates the effect of both crop transpiration and soil evaporation. (Kotsopoulos 2003) applied single and dual K_c for comparison, and found the two methods estimating efficiently the actual crop evapotranspiration, their results being similar when irrigations was applied over the entire field. Single K_c factor was also used by (Beyazgul, Kayam et al. 2000) in their comparative study of the performance of ET_o estimation methods.

ET_o represent the evaporation power of the atmosphere,(Allen and Fao 1998) and there are several estimation methods that have been formulated suitable for different conditions, (Beyazgul, Kayam et al. 2000). The ET_o data used in this study was previously calculated based on FAO Penman-Monteith method. Averaging the ET_o from the two stations seems to have served the purpose, as the difference was low, (MAB=RMSE=0.03 mm/day). It could not be ascertained as to whether standard approaches like inverse-square-distance applied by (Ray and Dadhwal 2001) would have given different results.

FAO 56 methodology is especially suitable for standard condition, where the crop is not subject to stress in terms of agronomic, soil or water, (Rossi 2007). In spite of it being simple, its major drawback is in regard to its non-spatial nature, using instead point data of ET_o and K_c, (Ray and Dadhwal 2001). Yet the climate data used to measure ET are highly variable spatially, hence limiting potential of this 'traditional' approach to take into account the actual crop growing condition and real-time vegetation variations.

S-SEBI algorithm, on the other hand, is a spatially-based model of estimating evapotranspiration, heavily based on retrieving fluxes from remotely sensed data, requiring very few ancillary measurements from the weather stations. Its main disadvantage is in its requirement for extremes temperatures along the spectrum to be determined from the image itself, such that extreme dry and wet hydrological conditions must be present, (Sobrino 2007). In S-SEBI, these extreme temperatures are determined over the spectrum of changing reflectance values; in contrast to other methods that try to determine a fixed temperature for wet and dry conditions for the whole image and /or for each land use class,(Roerink 1997). According to (Gomez 2005), one main difference between S-SEBI and SEBAL lies in the former method not considering H (sensible heat) flux computation, aerodynamic and thermal roughness. Determination of roughness length is a difficult task; and the fact that S-SEBI bypasses such hustle yet estimating evapotranspiration with comparable accuracy as SEBAL is indeed an advantage.

Evaluation of evapotranspiration estimates using S-SEBI involved resolving the energy balance equation. Propagation of errors in such extensive processing was an issue, a subject of sensitivity analysis of the accuracy of the products derived from S-SEBI,(Gomez 2005),

and (Sobrino 2007). To minimize errors, caution should be exercised when calculating variables and parameters involved in the retrieval of ET.

In this study, input variables were mainly from MODIS archive, whose quality assurance is exercised. With regard to the Landsat TM, retrieval of at-surface estimates of the parameters followed proven methods. For example, atmospheric correction of band 3 and 4 using SMAC algorithm and subsequent estimation of at-surface NDVI yielded good results, similar to what (Sobrino, Jimenez-Munoz et al. 2004) got. The method for retrieval of net radiation was based on the procedure of (Hurtado and Sobrino 2001).

The estimated instantaneous net radiation in this study was in general overestimated, and the deviation /error (RMSE=98 W/m², 19%) exceeded the normal range reported by other researchers in terms of relative error ,(Sobrino 2007), (Gomez 2005) and (Sobrino, Gomez et al. 2005) (7%). In (Gomez 2005), it was noted that errors in net radiation estimations could be related to the errors in albedo estimations. It was difficult to assess the accuracy of the input parameters for estimation of net radiation. While albedo values may have been in good agreement with the values in the literature, averaged MODIS emissivity data in the early part of the growing season was underestimated compared to values suggested in the literature. Also, the implication of the discrete nature of the ground measurement and associated measurement error could not be immediately verified, yet it immensely impact any comparison operations, (Bisht 2005). The limitation imposed by course resolution MODIS in establishing relationship between averaged values representatives of spatially varied variable in a square km pixel with few discrete values measured on the ground within the pixel should also be kept in mind while analyzing the outputs.

This latter point seems plausible in explaining the outcome of the net radiation comparison when seen in context of the study by (Jacobs 2002) and reviewed by (Bisht 2005). The former employed Geostationary Operational Environmental Satellites (GEOS-8) systems on a 20km grid cell in estimating instantaneous net radiation (INR) and compared the results with pyrometer estimates. They reported a bias and RMSE for INR as 73.5 W/m² and 107 W/m² respectively. The study was only for one ground station as in the case of the current study, while a fixed value of surface emissivity and surface albedo was assumed over the grid. In (Bisht 2005), MODIS (a square km pixel) was used, yielding an error of about (bias and RMSE) 59 W/m² and 74 W/m² respectively for INR. They reported low bias and RMSE when similar comparison was performed for daily net radiation, (60 W/m² and 50 W/m² respectively).

It is important to note that among the errors incurred in processing of S-SEBI input variables and parameters, the errors in the determination of T_H and T_{AE} lines, and therefore in evaporative fraction have a major impact on the estimation of evapotranspiration, (Gomez 2005; Sobrino 2007). This arises as graphical procedures are employed in obtaining the two lines and may generate significant errors.

Over and above, it may be concluded that the overall fitness of S-SEBI outputs was on average good. Validation of S-SEBI outputs for ET values over water surface against estimation of simulated PAN ET from meteorological data indicated that the model output was plausible, in terms of high R^2 (0.90) and reasonable RMSE (1.16 mm/day). The obtained r^2 value was higher than that obtained by (Conrad 2007) ($r^2=0.6$) who performed similar comparison, indicating slightly better results in this study. The RMSE was not very different from that obtained by (Gomez 2005), (1 mm/day), and agree with the errors incurred in graphical determination of evaporative fraction. The scattering obtained may be related to the errors in $R_{ni} - G_i$ and to the determination of evaporative fraction.

Analysis of the evolution of estimated S-SEBI ET implied the effect of net radiation profile (that in turn influences the evaporative fraction) and the variability of crops covers and soil

moisture regime, the last two being profound in the second period observed mid January onwards.

Against expectation, relationship between evapotranspiration on one hand and soil moisture availability and NDVI on the other hand, was observed to be lacking and in some cases poor or negative. Lag of NDVI to register sudden drop of evapotranspiration during stress events was attributed to affect the nature of relationship. In (Duchemin 2006), it was observed that as the NDVI saturates, it fails to be a good instantaneous indicator of plant stress.

With respect to soil moisture, there was no relationship with evaporative fraction estimated by S-SEBI. Similar observations were made by (Su 2003). They obtained weak relationships in shallow depths than in deeper layers. These observations are unexpected, and against the statistically proved exponential relationship derived by (Scott, Bastiaanssen et al. 2003).

In (Su 2003), these observations were explained by referring to the coarse resolution of NOAA-AVHRR. Similarly, moderate resolution as MODIS can not detect spatial variations in daily evapotranspiration within 1 square km area of its resolution, but approximates the average value over the pixel. On the other hand, measured soil moisture is only in few points within the MODIS pixel. Therefore, the big variation in soil moisture within the MODIS pixel may result in low correlation of the relative soil moisture and evapotranspiration as observed in the scatter plots.

The S-SEBI Kc profile was observed to deviate from usual profile of Kc along crop growth stages. Statistical comparison with published FAO 56 Kc showed significant deviation, (RMSE=0.45). Similar measure of deviation was observed with respect to phase-averaged S-SEBI Kc, (RMSE=0.45). In comparison with evapotranspiration in wheat area derived from direct application S-SEBI algorithm, estimates based on application of phase averaged S-SEBI Kc seemed more reliable (RMSE=0.90 mm/day) than those based on application of published FAO 56 Kc (RMSE=1.2 mm/day).

According to (Paco, Ferreira et al. 2006), crop coefficients vary significantly during the growth season limiting possibility to assume a constant value. In their review, they noted that FAO 56 approach showed a certain lack of sensitivity to capture the dynamic nature of the evaporation process. The phase-averaged S-SEBI Kc was observed to respond better to dynamics of evapotranspiration in mid season. Kc drops rapidly during stress events,(Duchemin 2006).On the other hand, it was noted in (Allen and Fao 1998) and (Tasumi 2005) that during initial phase, Kc increases in condition of wet soil surface layer after irrigation or rain events. In (Choudhury 1994), it was observed that changes in soil evaporation did significantly affect Kc for low values of leaf area index.

The implication of soil evaporation was significant when modelling Kc and vegetation indices relationship. In (Er-Raki 2007), it was noted that the relationship between Kc and NDVI for winter wheat is affected by soil evaporation. In (Choudhury 1994), dependence of Kc and leaf area index was hardly recognizable for wet soil. Kc for wet soils was seen to be less strongly dependent on leaf area index. This was especially evident when the data of S-SEBI Kc and NDVI during low vegetation cover was included in modelling. The scatter was big, proving difficult to establish a relationship. It is important to note that a moderate relationship ($R^2=0.54$) in wheat field was established for data captured after March 2007, presumably when the wheat crop had fully covered the ground, limiting the influence of soil evaporation. This agree with the observation reported by (Choudhury 1994) and (Tasumi 2005), that Kc and NDVI have a clear relation during mid season but no clear relation holds during periods having low ground cover due to influence of soil evaporation. The low correlation is associated with scatter introduced by lag of NDVI to immediately respond to rapid drop of transpiration rates during stress events, (Duchemin 2006). Further study is recommended to

elaborate the nature of relationship between these variables in condition differing in moisture regimes.

A method was proposed that basically adapts FAO -56 model using remote sensing technologies was elaborated in this study. The scheme evidently integrates several sub-modules, ranging from resolving spatially the normally point-based published crop coefficient to estimation of spatially distributed water stress coefficient. As any other model, its performance was dependent of the theoretical and experimental robustness of the sub-modules but also their adequacy in local situation.

The feasibility of estimating crop coefficient (K_c) from spectral measurements occurs because both K_c and vegetation indices are affected by leaf area index, (Choudhury 1994) and (Er-Raki 2007). In definition of reflectance-based crop coefficient, the remark of (Choudhury 1994) suffice as caution, that variabilities in any relation between crop coefficient and vegetation indices may arise from changes in both soil and atmospheric characteristics and also due to interactions between soil and vegetation in determining evaporation and transpiration rates.

This study investigated three procedures of modelling relationship between K_c and vegetation indices. Relationship of FAO 56 K_c -NDVI time series for winter wheat crop was successfully established during the mid-season, ($R^2=0.85$). This was as expected, as there was similarity between the seasonal pattern of NDVI and tabulated K_c curve that offer potential for modelling NDVI into K_c , (Er-Raki 2007). Similar relationship had been modelled by (Rossi 2007) who applied MODIS NDVI-time series. (Ray and Dadhwal 2001) also successfully distributed spatially tabulated K_c using series of soil adjusted vegetation index (SAVI) derived from WiFS (wide field sensor) on board IRS-1C satellite.

Application of per-image NDVI histogram approach proved possible to use only one image to establishing a linear incremental relationship between FAO 56 K_c and two extreme NDVI values in a cropped area. According to (Seevers 1994), defined incremental equations can be used for other images acquired within a particular crop development stage. In period of low vegetation cover, the low value of upper boundary of the respective regression model meant that the procedure was prone to error of underestimating K_{cr} and in turn the evapotranspiration estimates. Its application would seem tenable during mid-season from the results. However, with coarse resolution as MODIS NDVI data, it was difficult to reliably delineate the two extreme points in the NDVI histogram. In (Seevers 1994), the peak NDVI value was also not discernible in NOAA-AVHRR. However, definition of the model was straightforward in Landsat TM.

Estimates of K_{cr} based on the three procedures were highest in mid season (JD 68) and lowest in end season (JD 184) but differed remarkably. These differences were also reflected in crop evapotranspiration (ET_c) estimates that were calculated using K_{cr} and reference ET. The nature of the K_c -NDVI models partly influenced the estimates but also the sensitivity of the K_c relative to the dynamics of NDVI.

Previous studies reported successful evaluation of soil moisture availability function (K_s), (Kotsopoulos 2003) and (Beyazgul, Kayam et al. 2000). The former developed and employed a system of equations while the latter used a computer simulation model (IRSI) to account for limitations in root water uptake. In both cases, retrieved values were assumed to be representative of field condition.

In this study, a scheme was formulated of estimating spatially distributed K_s using remote sensing, by linking several sub-modules, from estimation of evaporative fraction, depth-averaged soil moisture, effective rooting depth (RD), total available water (TAW) and depletion factor, unready available water (x_p) and eventually moisture stress function.

Estimation of evaporative fraction (EF) employed “Universal Triangle “ model formulated by (Carlson 2007) . The model has roots in previous work of many researchers, including (Gillies, Kustas et al. 1997) and proved reliable in estimating surface soil water content and energy fluxes. In all the three days analysed, the estimates were comparable, (RMSE <0.11).

Statistical modelling of depth-averaged soil moisture by employing evaporative fraction can be traced in the work of (Scott, Bastiaanssen et al. 2003), and similar procedure was employed in this study. Comparison of estimated soil moisture estimated by employing a statistical model in JD 68 and 184 against ground-based measurements by Diviner 2000™ were in good agreement in terms of bias, mean absolute error (MAE) and RMSE (9.38 mm, 9.38 mm, and 10.6 mm).

In the selected wheat area, observed variability of available soil water storage capacity (CV=40%) may be attributed to the variability in soil physical properties influencing the water holding capacity. In (Gomez-Plaza 2001) similar influence of physical parameters to soil water content was also observed.

Effective rooting depth apparently increased from planting up to the end of mid season development stage. The assumption made by (Colaizzi 2003) seems to agree with the observation. Again, the variability observed compares with that of Kcr, since the two are related linearly,(Jayanthi, Neale et al. 2007). Estimates of the three approaches were comparable in mid season (JD 68), since the Kcr estimates did not differ much.

Estimates of depletion factor based on the three procedures did not differ much on average basis. Depletion factor is a function of evapotranspiration, (Allen and Fao 1998) and (Kotsopoulos 2003). In those pixels with relatively low ETc, then by extent, the depletion factor was high, and vice versa.

Water held by soil matrix (**x_p**) estimated by the three approaches apparently increased from initial phase peaking during mid season (JD 68). On the overall, FAO 56 Kc-NDVI time series approach yielded the highest estimates and lowest variability followed in order by S-SEBI Kc-NDVI model and per-image histogram approach. Spatial and temporal distribution was attributed to weather condition that define the magnitude of crop evapotranspiration but also variability of soil matrix potential which correspond to soil types with different soil water content.

Evaluation of soil moisture availability by the three approaches indicated that soil moisture availability was not limiting the rate of evapotranspiration at least in JD 334 and 184. In JD 68, there was an apparent soil moisture stress detected in isolated pixels based on FAO 56 Kc-NDVI time series approach. These pixels are located within “Franco-Argiloso” soil texture class, which apparently has low available water storage capacity (AWSC) due to combination of physical components.

The final part of the proposed scheme was evaluation of actual evapotranspiration (ET_a) by accounting for apparent moisture stress in JD 68. For the days without moisture stress, crop potential evapotranspiration (ET_c) was considered equivalent to ET_a. In JD 68, estimated ET_a (based on FAO 56 Kc-NDVI time series approach) with a spatial resolution of 1000m averaged 3.65 mm/day and variability up to CV=11%. Error magnitude relative to S-SEBI ET was 1.34 mm/day, slightly higher than corresponding ET_c that had error magnitude of 1.31 mm/day).

Performance of the proposed scheme was evaluated against outputs of S-SEBI algorithm, for both crop coefficients and evapotranspiration estimates. When the accuracy of the ET_c estimates derived from these procedures is analyzed in view of the error estimated in S-SEBI

ET estimates (RMSE=1.16 mm/day), one will appreciate the magnitude of overall error that may be incurred while using the methods. Possible reasons are attributed to the nature of the constituent's elements of models that were used in deriving the K_c. S-SEBI K_c-NDVI model was already noted to be weak and attributed to the lag in the part of NDVI that did not respond immediately to fluctuations of S-SEBI K_c (Duchemin 2006), thereby introducing scatter in the relation (Choudhury 1994).

The shortcomings of the two FAO 56-K_c-NDVI models suggest that the K_c parameter in the model ought to have been adjusted to relate with the wet condition in initial phase (JD 334) and apparent stress event in JD 68. According to (Allen and Fao 1998) initial K_c increases more than the tabulated during frequent wet conditions. During stress events, actual K_c drops rapidly, (Duchemin 2006). According to (Tasumi 2005), the error range in predicted K_c would reduce significantly especially during periods of low vegetation cover, if dual K_c procedure that predicts the increase in K_c caused by a wet soil surface layer is utilized. This implies that application of dual K_c may contribute to addressing the limitation of 'traditional' FAO 56 model in terms of inability of the approach to account for the actual growing conditions and real-time vegetation variations, (Tasumi 2005). Further study to evaluate the proposed scheme while utilizing dual K_c is recommended.

8.2. Evaluation of weighted ratio approach in disaggregation of MODIS ET data and enhancement of spatial variability

Reliability of disaggregation of ET data derived from MODIS sensor-with low spatial but high temporal resolution- to a spatial resolution comparable to Landsat TM 5 based on weighted ratio approach was evaluated. Issues evaluated were consistency of the ET data from different sensor, quality of the derived weighting ratio maps, quality of the disaggregated MODIS ET data and spatial distribution and the effect of disaggregation to spatial variability.

Investigation of consistency of ET data for satellite images of different scales showed varied results. Corresponding S-SEBI ET estimates of Landsat TM 5 and MODIS showed in general an underestimation on the part of MODIS, (RMSE= 2.82 mm/day for JD 68 and 1.48 mm/day for JD 244). For ET_c estimates based on FAO 56 K_c-NDVI time series approach inconsistency (slight overestimation by MODIS) was showed in both JD 68 and 244, (RMSE=0.79 mm/day and 0.32 mm/day). Soil moisture estimates showed inconsistency (overestimation by MODIS). In JD 68, RMSE=53.7mm while in JD 244, maximum estimates by Landsat TM was 163 mm and mean estimate by MODIS was 221 mm. Estimates of water held by soil matrix also showed inconsistency (overestimation by MODIS) in both JD 68 and JD 244, (RMSE=81.44 mm and 48.8 mm respectively). (Hong, Hendrickx et al. 2005) attributed this to effect of resolution, where the high resolution of Landsat TM captured peaks of even small area that were however blurred by the coarse resolution of MODIS derived ET map.

The result of fitness evaluation of the derived weighted ratio maps showed that they were generally good, at least in terms of RMSE. For S-SEBI ET, FAO 56 K_c-NDVI time series approach, soil moisture estimate, and water held by soil matrix (xp), the corresponding RMSE was 0.67 mm/day, 0.50 mm/day, 25.6 mm and 9 mm respectively.

Quality of disaggregated maps derived by stretching the respective ratio maps into original MODIS maps (JD 68) showed high correlation with corresponding Landsat TM 5 ET estimate.

Measure of inconsistency between disaggregated MODIS maps of S-SEBI ET, FAO 56 K_c-NDVI time series approach, soil moisture estimate, and water held by soil matrix (xp) with corresponding Landsat TM maps of JD 68 in terms of RMSE was 3.00 mm/day, 0.84

mm/day, 65 mm, and 91 mm respectively. This indicated that the inconsistency of the estimates did not close after disaggregation.

Spatial variability of ET data increased following disaggregation from low spatial resolution. For S-SEBI ET estimates, it increased by 11 % in JD 334, but was insignificant for the other days analyzed. For ET_c estimates based on FAO 56 Kc-NDVI time series approach, it also increased significantly by 43% in JD 334, but moderately (14%) in the other days analyzed. For soil moisture estimates, the increase was moderate (12%) for the three days analyzed. Estimates of water held by soil matrix (xp) yielded marginal increase of spatial variability, (8% in JD 334 and 1% in JD 184).

In general, it was shown that the weighted ratio procedure of disaggregation of MODIS ET using detailed Landsat TM 5 data is quite reliable. Disaggregated products appeared blocky, giving a negative visual impression but as noted by (Chemin 2004), the local pixel values were correct. The quality of the initial/original products determines a lot the quality of the disaggregated products. For instance, the inconsistency between disaggregated MODIS and Landsat TM was about equal as the one estimated before disaggregation. Increase of spatial variability is a plus to weighted disaggregation procedure, which is quite simple to implement yet enhancing the spatial information of MODIS data. By complementing the high temporal resolution of MODIS data, possibility of enhanced spatial information would enable the Irrigation Advisory Services to improve their performances tremendously given that MODIS data are public domain and freely accessible.

9. CONCLUSIONS AND RECOMMENDATIONS

9.1. Conclusions

Improved operational and low cost methods will enable IAS to cost effectively monitor crop and irrigation water requirements of each field in extended areas. The benefit of this is in terms of improved irrigation scheduling by farmers thus alleviating the problems of over-irrigation and potential for nutrient leaching; but also inefficient use of water which has implication to yield. On an area-wide scale, successful monitoring of crop water use is essential for allocation and rights purpose and overall management and conservation against the background of inter-sectoral competition.

The study investigated the potential of the proposed remote sensing-based method and elaborated its strength of integrating remote sensing data in the FAO 56 method. It is expected that convenient adaptation of EO will improve the performance of IAS. The proposed method, however, reveals some unique aspects when viewed within the context and background of other methods.

Research question 1: *What are the existing remote sensing-based methods of estimating actual evapotranspiration (ET)?*

Several remote sensing based methods were reviewed in this study, including empirical, indirect and residual methods. The empirical methods, including reflectance-based crop coefficient approaches, are based on the relationships established between variables representing Earth surface processes, in turn used as proxies to infer evapotranspiration processes. Indirect methods generally use complex models simulating the different terms of energy budget, and remote sensing data can be incorporated at different levels. Residual methods are based on surface energy balance and combine empirical relationships and physical components. Most of them are based on the contrast between wet and dry areas existing in the image. Some calculate sensible heat (H) first and then obtain latent heat flux as the residual of the energy balance, e.g. SEBAL. Computation of H is complicated, involving the determination of aerodynamic and roughness length. Other residual methods like SEBI, SEBS and S-SEBI, estimate evapotranspiration from evaporative fraction.

Question 2: *How can an operational method of estimating actual evapotranspiration be developed?*

Indirect and residual methods (based on surface energy balance) reviewed in Chapter 2 yield accurate estimates of evapotranspiration. However, they are very advanced and sophisticated, their implementation not readily matching the current procedure of Irrigation Advisory Services.

The study investigated a remote sensing-based method that does not require major adjustment of the operational procedure of IAS, and which is convenient for most of them in terms of adaptation of Earth Observation technologies. The method is based on the use of remotely sensed vegetation index to resolve crop coefficient spatially-in turn used to obtain maps of crop evapotranspiration (section 6.3 & 6.4)- and estimation of soil moisture stress factor estimated using remote sensing data,(section 6.6). The latter element accounts for soil moisture availability, critical in situation of moisture stress. Three variants of the proposed method were investigated. The variants differ in terms of the procedure to resolve crop coefficient spatially.

Question 3: *What would be the results of the operational method and its practical performance?*

The study has shown that the operability of the first module of the proposed method (resolving crop coefficient spatially) is straightforward, with only few computation steps. However, the second module (estimation of soil moisture stress factor) is quite complicated, involving several steps before the soil moisture availability function is retrieved.

Of the three variants investigated, procedure 1 (FAO 56 Kc-NDVI time series) and procedure 2 (per image NDVI histogram approach) are easy to implement as they rely on the tabulated FAO 56 Kc. With one image, procedure 1 can be implemented, in contrast to procedure 2 that require series of NDVI in at least two crop growth phases to establish a Kc-NDVI model. Implementation of procedure 3 (S-SEBI Kc-NDVI model) is complicated as it requires first the determination of Kc based on energy balance (residual) methods.

Questions 4: *How reliable are the estimates derived from the operational method relative to estimates derived from the energy balance approaches?*

Estimates of crop coefficients and evapotranspiration in selected wheat area by the three variants deviated to some extent from corresponding S-SEBI estimates (Chapter 7). In JD 334 (during initial phase), evapotranspiration rates was slightly underestimated by the three variants relative to S-SEBI estimates. Procedure 2 was the least accurate. In JD 68 (during mid season), Procedure 1 and 'traditional' FAO 56 approach overestimated evapotranspiration rates while Procedure 3 closely matched S-SEBI ET estimates. In JD 184 (during end phase), evapotranspiration rates was significantly underestimated by Procedure 2 and slightly overestimated by P1. Procedure 3 closely matched S-SEBI ET estimates. Of the three variants, Procedure 3 seemed more reliable in tracking the dynamics of evapotranspiration. Procedure 1 was less reliable, but quite better than Procedure 2.

The study has also showed the existing potential of disaggregation procedures that would enable IAS to use the moderate to low spatial resolution satellite data. Most IAS can freely access MODIS data (being a public domain) and disaggregation would then allow them to extract spatial information with high spatial variability matching that of high resolution satellite data. This is an added benefit to IAS, complementing their need to monitor crop water use on reasonable temporal and spatial scales. Spatial distribution of estimated variables from MODIS and Landsat TM 5 data were inconsistent, attributed to estimation error. The quality of disaggregation procedure in terms of weighted ratio map was good. Increase of spatial variability was evident in all disaggregated MODIS products as measured by coefficient of variation.

9.2. Recommendations

In general, this study has furthered previous studies of reflectance-based crop coefficient approach of estimating evapotranspiration. Major improvement was the introduction of spatially modelled soil moisture stress coefficient (Ks) to evaluate actual from potential evapotranspiration. Within the scope of the literature reviewed, this was the first attempt to model Ks spatially using remote sensing data and integrate resultant maps into the adapted FAO 56 model.

As an additional strength, the proposed method yields other important products besides ETc. Depth-averaged soil moisture and readily available water in root zone distribution give an indication of the availability of moisture to sustain crops during growth period. Root depth maps would enable the farmer to better manage tillage practice, since the latter influences root penetration.

As a practical recommendation, the scheme may be appropriate in conditions/areas occasioned by moisture stress, by virtue of having a module to detect and evaluate spatial distribution of soil moisture stress.

Implementation of the scheme would also require that choice of crop coefficient be carefully assessed, especially during the initial and mid phases. This may require adjustment of the single K_c to be consistent with wetting/drying events during or following dual crop coefficient approach.

Successful operationalisation of the scheme requires that soil textural properties and water holding characteristics be known and mapped. It is expected that many Irrigation Advisory Services (IAS) already have these data in their database.

To benefit from potential of weighted ratio disaggregation approach, effort should be made to ensure that accuracy of both low and high resolution is maintained during the earlier processing phases, so that spatial distribution of the estimated variables match in spite of resolution. The good quality of the weighted ratio maps and enhanced spatial information are both positive attributes of disaggregation. Decision of the level at which to apply disaggregation is important. Choosing to disaggregate only the final products is convenient and makes the operation simpler.

Further studies are recommended especially in two areas:

1. In view of the unexpected relationships observed between surface variables estimated by satellite data and ground measurements, further study is recommended to elaborate the nature of relationship between these variables in condition of differing moisture regimes and using satellite data of different spatial resolution.
2. Further, in view of the shortcomings of the proposed scheme based on single K_c , performance of the scheme while using dual K_c should also be evaluated.

10. References

- Akbari, M., Toomanian, N., Droogers, P., Bastiaanssen, W., & Gieske, A. (2007). "Monitoring irrigation performance in Esfahan, Iran, using NOAA satellite imagery." *Agricultural Water Management* **88**(1-3): 99-109.
- Allen, R. G. (2000). "Using the FAO-56 dual crop coefficient method over an irrigated region as part of an evapotranspiration intercomparison study." *Journal of Hydrology* **229**(1-2): 27-41.
- Allen, R. G., Pereira, L.S., Raes, D., Smith, M., & FAO (1998). *Crop evapotranspiration : guidelines for computing crop water requirements*. Rome, FAO.
- Bandara, K. M. P. S., Bos, M. G., Feddes, R.A. (2006). Assessing irrigation performance by using remote sensing. *ITC Dissertation;134*. Wageningen, Wageningen University: 156.
- Bastiaanssen, W. G. M. (2000). "SEBAL-based sensible and latent heat fluxes in the irrigated Gediz Basin, Turkey." *Journal of Hydrology* **229**(1-2): 87-100.
- Bastiaanssen, W. G. M. and S. Ali (2003). "A new crop yield forecasting model based on satellite measurements applied across the Indus Basin, Pakistan." *Agriculture, Ecosystems & Environment* **94**(3): 321-340.
- Bastiaanssen, W. G. M., Menenti, M., Feddes, R. A. & Holtslag, A. A. M. (1998). "A remote sensing surface energy balance algorithm for land (SEBAL). 1. Formulation." *Journal of Hydrology* **212-213**: 198-212.
- Bastiaanssen, W. G. M., Molden D. J. & Makin, I.W. (2000). "Remote sensing for irrigated agriculture: examples from research and possible applications." *Agricultural Water Management* **46**(2): 137-155.
- Bausch, W. C. (1993). "Soil background effects on reflectance-based crop coefficients for corn." *Remote Sensing of Environment* **46**(2): 213-222.
- Bausch, W. C. (1995). "Remote sensing of crop coefficients for improving the irrigation scheduling of corn." *Agricultural Water Management* **27**(1): 55-68.
- Belmonte, A. C., Jochum, A. & Garcia, A. (2003). "Space-assisted irrigation management: Towards user-friendly products." *ICID Workshop on Remote Sensing of ET for Large Regions, 17 September, 2003*.
- Beyazgul, M., Kayam, Y. & Engelsman, F. (2000). "Estimation methods for crop water requirements in the Gediz Basin of western Turkey." *Journal of Hydrology* **229**(1-2): 19-26.
- Bisht, G., Venturini, V., Islam, S. & Jiang, L. (2005). "Estimation of the net radiation using MODIS (Moderate Resolution Imaging Spectroradiometer) data for clear sky days." *Remote Sensing of Environment* **97**(1): 52-67.
- Bochenek, Z. e. (2007). *New developments and challenges in remote sensing : proceedings of the 26th symposium of the European association of remote sensing laboratories EARSeL, Warsaw, Poland, 29 May-2 June 2006*. Rotterdam.
- Bouman, B. A. M. (2007). "A conceptual framework for the improvement of crop water productivity at different spatial scales." *Agricultural Systems* **93**(1-3): 43-60.
- Calera, A., Jochum, A., & Garcia, A. (2003). "Space-assisted irrigation management: Towards user-friendly products." *ICID Workshop on Remote Sensing of ET for Large Regions, 17 September, 2003*.
- Carlson, T. (2007). "An Overview of the "Triangle Method" for Estimating Surface Evapotranspiration and Soil Moisture from Satellite Imagery." *Sensors* **7**: 1612-1629.
- Chemin, Y., & Alexandridis, T. (2004). "Spatial Resolution Improvement of Seasonal Evapotranspiration for Irrigated Rice, Zhanghe Irrigation District, Hubei Province, China." *Asian Journal of Geoinformatics* **5**(1): 3-11.
- Choudhury, B., Ahmed, N., Idso, S., Reginato, R., Daughtry, C.S. T. (1994). "Relations between evaporation coefficients and vegetation indices studied by model simulations." *Remote Sensing of Environment* **50**(1): 1-17.

- Colaizzi, P. D., Barnes, E.M., Clarke, T.R., Choi, C.Y. & Waller, P.M. (2003). "Estimating Soil Moisture Under Low Frequency Surface Irrigation Using Crop Water Stress Index." Journal of Irrigation and Drainage Engineering **129**(1): 27-35.
- Conrad, C., Dech, S., Hafeez, M., Lamers, J., Martius, C. & Strunz, G. (2007). "Mapping and assessing water use in a Central Asian irrigation system by utilizing MODIS remote sensing products." Irrigation and Drainage Systems **21**(3): 197-218.
- Courault, D., Seguin, B. & Olioso, A. (2003). "Review to estimate Evapotranspiration from remote sensing data: some examples from the simplified relationship to the use of mesoscale atmospheric models." ICID Workshop on Remote Sensing of ET for Large Regions.
- De Lannoy, G. J. M., Verhoest, N. E. C., Houser, P. R., Gish, T. J. & Van Meirvenne, M. (2006). "Spatial and temporal characteristics of soil moisture in an intensively monitored agricultural field (OPE3)." Journal of Hydrology **331**(3-4): 719-730.
- de Wit, A. J. W. and H. L. Boogaard (2001). Monitoring of crop development and crop model optimisation using NOAA - AVHRR : towards an integrated satellite and model - based crop monitoring system in the European context. Delft, Beleidscommissie Remote Sensing (BCRS).
- Doraiswamy, P. C., Hatfield, J. L., Jackson, T.J.M Akhmedov, B., Prueger, J. & Stern, A. (2004). "Crop condition and yield simulations using Landsat and MODIS." Remote Sensing of Environment **92**(4): 548-559.
- Duchemin, B., Hadria, R., Erraki, S., Boulet, G., Maisongrande, P., Chehbouni, A., Escadafal, R., Ezzahar, J., Hoedjes, J. C. B., Kharrou, M. H., Khabba, S., Mougnot, B., Olioso, A., Rodriguez, J. C. & Simonneaux, V. (2006). "Monitoring wheat phenology and irrigation in Central Morocco: On the use of relationships between evapotranspiration, crops coefficients, leaf area index and remotely-sensed vegetation indices." Agricultural Water Management **79**(1): 1-27.
- Dunkel, Z. and I. Grob-Szenyan (2002). "A simple method for estimation of evapotranspiration using remotely sensed data during vegetation period in Hungary." Physics and Chemistry of the Earth, Parts A/B/C **27**(23-24): 1109-1111.
- English, M. J., Solomon, K.H., & Hoffman, J.G. (2002). "A Paradigm Shift in Irrigation Management." Journal of Irrigation and Drainage Engineering **128**(5): 267-277.
- Er-Raki, S., Chehbouni, A., Guemouria, N., Duchemin, B., Ezzahar, J., & Hadria, R. (2007). "Combining FAO-56 model and ground-based remote sensing to estimate water consumptions of wheat crops in a semi-arid region." Agricultural Water Management **87**(1): 41-54.
- Gillies, R. R., W. P. Kustas, et al. (1997). "A verification of the "triangle" method for obtaining surface soil water content and energy fluxes from remote measurements of the Normalized Difference Vegetation Index (NDVI) and surface radiant temperature." International Journal of Remote Sensing **18**(15): 3145-3166.
- Gomez-Plaza, A., Martinez-Mena, M., Albaladejo, J. & Castillo, V. M. (2001). "Factors regulating spatial distribution of soil water content in small semiarid catchments." Journal of Hydrology **253**(1-4): 211-226.
- Gomez, M., Olioso, A., Sobrino, J. A. & Jacob, F. (2005). "Retrieval of evapotranspiration over the Alpillles/ReSeDA experimental site using airborne POLDER sensor and a thermal camera." Remote Sensing of Environment **96**(3-4): 399-408.
- Hong, S., Hendrickx, J. M. H. & Borchers, B. (2005). "Effect of Scaling Transfer between Evapotranspiration Maps Derived from Landsat 7 and MODIS Images." Proceedings of SPIE **5811**: 147-158.
- Huete, A. R. (1988). "A soil-adjusted vegetation index (SAVI)." Remote Sensing of Environment **25**(3): 295-309.
- Hurtado, E. and J. A. Sobrino (2001). "Daily net radiation estimated from air temperature and NOAA-AVHRR data: a case study for the Iberian Peninsula." International Journal of Remote Sensing **22**(8): 1521-1533.
- Jacobs, J. M., Myers, D. A., Anderson, M. C. & Diak, G. R. (2002). "GOES surface insolation to estimate wetlands evapotranspiration." Journal of Hydrology **266**(1-2): 53-65.

- Jayanthi, H., Neale, C. M. U. & Wright, J.L. (2007). "Development and validation of canopy reflectance-based crop coefficient for potato." *Agricultural Water Management* **88**(1-3): 235-246.
- Jiang, L. and S. Islam (2001). "Estimation of surface evaporation map over southern Great Plains using remote sensing data" *Water Resources Research* **37**(2): 329.
- Kite, G. and P. Droogers (2000). "Comparing evapotranspiration estimates from satellites, hydrological models and field data." *Journal of Hydrology* **229**(1-2): 1-2.
- Kotsopoulos, S., Kalfountzos, D., Alexiou, I., Zerva, G., Karamaligas, C. & Vyrlas, P. (2003). "Actual evapotranspiration and soil moisture studies in irrigated cotton fields." *European Water* **3**(4): 25-31.
- Li, F. and T. J. Lyons (2002). "Remote estimation of regional evapotranspiration." *Environmental Modelling & Software* **17**(1): 61-75.
- Lorite, I. J., Mateos, L., Orgaz, F., Fereres, E. "Assessing deficit irrigation strategies at the level of an irrigation district." *Agricultural Water Management In Press, Corrected Proof*.
- Martin de Santa Olalla, Calera, F., A. & Dominguez, A. (2003). "Monitoring irrigation water use by combining Irrigation Advisory Service, and remotely sensed data with a geographic information system." *Agricultural Water Management* **61**(2): 111-124.
- Martyniak, L., Dabrowska-Zielinska, K., Szymczyk, R. & Gruszczynska, M. (2007). "Validation of satellite-derived soil-vegetation indices for prognosis of spring cereals yield reduction under drought conditions - Case study from central-western Poland." *Advances in Space Research* **39**(1): 67-72.
- Moran, M. S., Inoue, Y. & Barnes, E.M. (1997). "Opportunities and limitations for image-based remote sensing in precision crop management." *Remote Sensing of Environment* **61**(3): 319-346.
- Nishida, K., Nemani, R. R. & Running, S.W. (2003). "An operational remote sensing algorithm of land surface evaporation." *Journal of Geophysical Research* **108**(D9): 4270.
- Ortega, J. F., de Juan, J. A. & Tarjuelo, T.M. (2005). "Improving water management: The irrigation advisory service of Castilla-La-Mancha (Spain)." *Agricultural Water Management* **77**: 37-58.
- Paco, T. A., M. I. Ferreira, et al. (2006). "Peach orchard evapotranspiration in a sandy soil: Comparison between eddy covariance measurements and estimates by the FAO 56 approach." *Agricultural Water Management* **85**(3): 305-313.
- Paralta, E., Fernande, R., Carreira, P. & Ribeiro, L. (2005). "Assessing the impacts of Agriculture on Groundwater quality using nitrogen isotopes-preliminary results on the "Gabbros of Beja" Aquifer System (South Portugal)." *2nd Workshop of the Iberian Regional Working Group on Hardrock Hydrogeology, 18-21 May 2005, Evora, Portugal.* : 14
- Qin, Z., A. Karnieli, et al. (2001). "A mono-window algorithm for retrieving land surface temperature from Landsat TM data and its application to the Israel-Egypt border region." *International Journal of Remote Sensing* **22**(18): 3719 - 3746.
- Ray, S. S. and V. K. Dadhwal (2001). "Estimation of crop evapotranspiration of irrigation command area using remote sensing and GIS." *Agricultural Water Management* **49**(3): 239-249.
- Roerink, G. J., Bastiaanssen, W. G. M., Chambouleyron, J. & Menenti, M. (1997). "Relating Crop Water Consumption to Irrigation Water Supply by Remote Sensing." *Water Resources Management* **11**(6): 445-465.
- Roerink, G. J., Z. Su, et al. (2000). "S-SEBI: A simple remote sensing algorithm to estimate the surface energy balance." *Physics and Chemistry of the Earth, Part B: Hydrology, Oceans and Atmosphere* **25**(2): 147-157.
- Rossi, S., & Bocchi, S. (2007). *Monitoring crop evapotranspiration with time series of MODIS satellite data in Northern Italy* Rotterdam, Millpress.

- Scott, C. A., Bastiaanssen, W. G. M. & Ahmed, M. (2003). "Mapping Root Zone Soil Moisture Using Remotely Sensed Optical Imagery." Journal of Irrigation and Drainage Engineering **129**(5): 326-334.
- Seevers, P. M., & Ottmann, R.W. (1994). "Evapotranspiration estimation using a normalized difference vegetation index transformation of satellite data." Hydrological Sciences Journal **39**(4): 333-345.
- Sen, P. K. and A. S. M. Gieske (2005). "Use of GIS and Remote Sensing in identifying recharge zones in an arid catchment: a case of Roxo River basin, Portugal." Journal of Nepal Geological Society **31**: 25-32.
- Sobrino, J. A., Gomez, M., Jimenez-Monoz, J.C., Olioso, A., Chehbouni, G. (2005). "A simple algorithm to estimate evapotranspiration from DAIS data: Application to the DAISEX campaigns." Journal of Hydrology **315**(1-4): 117-125.
- Sobrino, J. A., Gomez, M., Jimenez-Munoz, J. C. & Olioso, A. (2007). "Application of a simple algorithm to estimate daily evapotranspiration from NOAA-AVHRR images for the Iberian Peninsula." Remote Sensing of Environment **110**(2): 139-148.
- Sobrino, J. A., Jimenez-Munoz, J. C., Juan, C. & Paolini, L. (2004). "Land surface temperature retrieval from LANDSAT TM 5." Remote Sensing of Environment **90**(4): 434-440.
- Stisen, S., Sandholt, I., Norgaard, A., Fensholt, R., Jensen, K. "Combining the triangle method with thermal inertia to estimate regional evapotranspiration -- Applied to MSG-SEVIRI data in the Senegal River basin." Remote Sensing of Environment In Press, Corrected Proof.
- Su, Z., Yacob, A., Wen, J., Roerink, G., He, Y., Gao, B., Boorgaard, H., van Diepen, C. (2003). "Assessing relative soil moisture with remote sensing data: theory, experimental validation, and application to drought monitoring over the North China Plain." Physics and Chemistry of the Earth, Parts A/B/C **28**(1-3): 89-101.
- Tasumi, M. and R. G. Allen (2007). "Satellite-based ET mapping to assess variation in ET with timing of crop development." Agricultural Water Management **88**(1-3): 54-62.
- Tasumi, M., Allen, R., Trezza, R. & Wright, J. (2005). "Satellite-Based Energy Balance to Assess Within-Population Variance of Crop Coefficient Curves." Journal of Irrigation and Drainage Engineering, ASCE **131**(1): 94-109.
- Vazifedoust, M., Dam, J.C., Feddes, R. A. & Bastiaanssen, W. G. M. (2007). "Disaggregation of remote sensing evapotranspiration data: from low to high spatial resolution." Geophysical Research Abstracts **9**(02674).
- Wang, L., Qu, J. J., Zhang, S., Hao, X., Dasgupta, S. (2007). "Soil moisture estimation using MODIS and ground measurements in eastern China." International Journal of Remote Sensing **28**(6): 1413-1418.
- Wesseling, J. G. and R. A. Feddes (2006). "Assessing crop water productivity from field to regional scale." Agricultural Water Management **86**(1-2): 30-39.
- Wu, W., Hall, C. A. S., Scatena, F. N. & Quackenbush, L. J. (2006). "Spatial modelling of evapotranspiration in the Luquillo experimental forest of Puerto Rico using remotely-sensed data." Journal of Hydrology **328**(3-4): 733-752.
- Zwart, S. J. and W. G. M. Bastiaanssen (2004). "Review of measured crop water productivity values for irrigated wheat, rice, cotton and maize." Agricultural Water Management **69**(2): 115-133.
- Zwart, S. J. and W. G. M. Bastiaanssen (2007). "SEBAL for detecting spatial variation of water productivity and scope for improvement in eight irrigated wheat systems." Agricultural Water Management **89**(3): 287-296.

AERONET. Aerosol Robotic Network. URL: <http://aeronet.gsfc.nasa.gov/> Access Date: 19 October 2007.

Eurimage. URL: <http://www.eurimage.com/> . Access date: November 15 2007

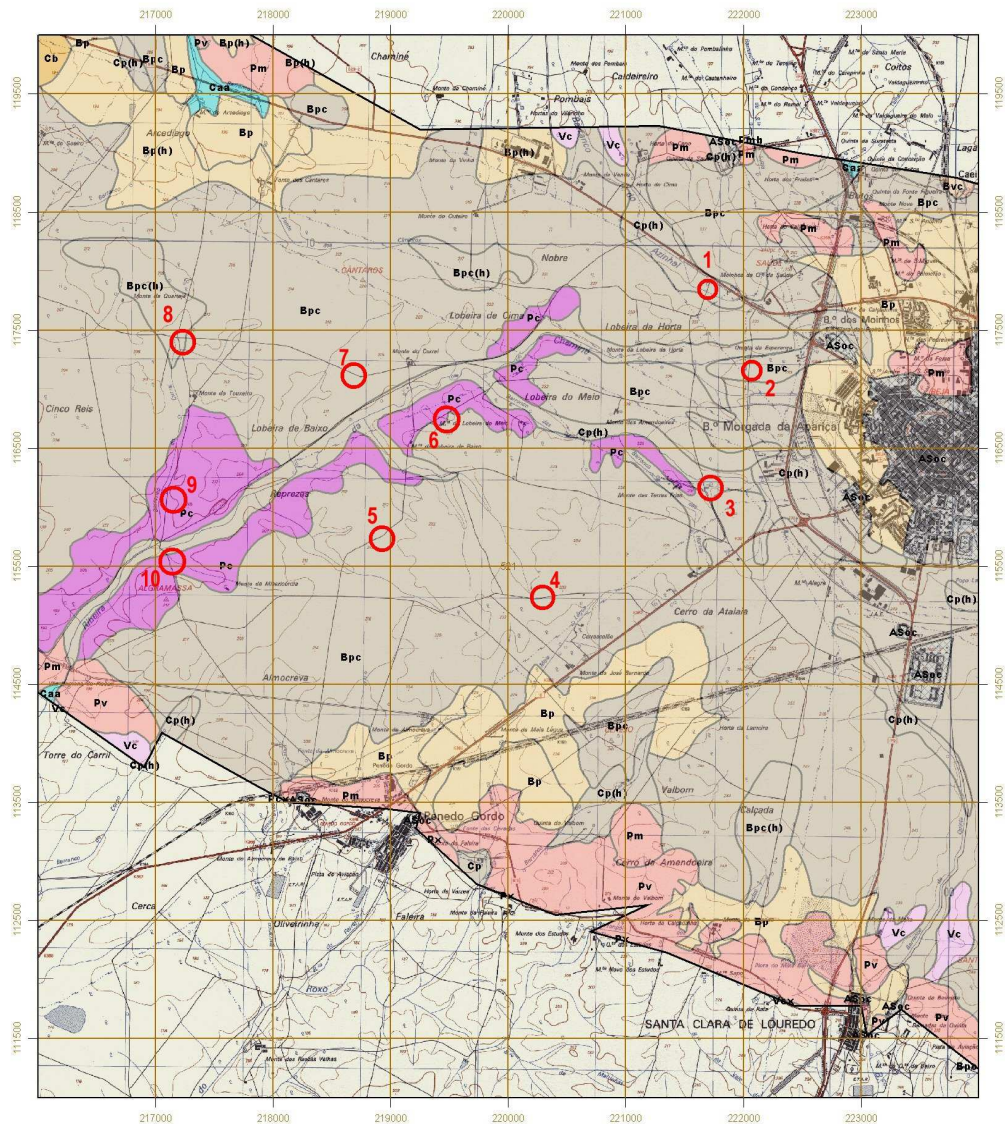
Earth Observing System (EOS) Aura. URL: <http://aura.gsfc.nasa.gov/instruments/omi/index.html> . Access date: 22 November 2007

Simsphere. A Biosphere/Atmosphere Simulation. URL:

<http://www.agry.purdue.edu/climate/dev/simsphere.asp> . Access date: 31 October 2007

11. Appendices

Appendix 1: Soil samples collected over different soil types in Pisos for determination of soil water holding characteristics



Aluviossolos	Solos Calcários	Barros
Modernos, Calcários	Pardos dos Climas de Regime Xérico	Castanho-Avermelhados, Calcários
Modernos, Não Calcários	Vermelhos dos Climas de Regime Xérico	Barros Castanho-Avermelhados, Não Calcários
Antigos, Não Calcários	Solos Argiluvitados	Pretos, Calcários
Solos Incipientes	Pouco Instaurados-materiais calcários	Barros Pretos, Não Calcários
Solos Incipientes - Calcários	Pouco Instaurados-materiais não calcários	Afloramento rochoso
Não Calcários	Litossolos	Afloramento rochoso
Solos Hidromórficos	Dos Climas de Regime Xérico	Outros
Sem horizonte Eluvial	Não Húmicos Pouco Insaturados	Área Social

Appendix 2: Soil water holding characteristic among sampled locations in Pisos

Location	Horiz.	Deep. (cm)	$\theta v_{0.33B}^*$ (%)	$\theta v_{1.0B}$ (%)	$\theta v_{5.0B}$ (%)	$\theta v_{15.0B}^{**}$ (%)
P₁	Ap₁	0-38	48.20	32.09	27.13	25.92
	B₁	38-105	47.53	35.17	30.56	28.14
	B₂	105-132	44.86	34.69	29.89	27.30
	Bc	132-163	42.50	32.81	27.01	26.83
P₂	Ap	0-23	28.09	24.43	23.31	19.89
	B	23-45	32.77	29.69	21.65	22.39
P₃	Ap	0-30	41.50	34.92	29.72	22.11
	B	30-52	39.02	28.38	26.52	25.10
	Bc	52-69	29.12	26.74	22.54	20.58
P₄	Ap	0-30	32.00	26.77	23.57	17.62
	B	30-47	32.75	26.95	23.57	17.90
	Bc	47-60	28.63	22.79	20.24	15.39
P₅	Ap₁	0-35	43.20	34.40	33.53	31.60
	B	35-70	45.47	35.21	33.02	31.29
	Bc	70-84	36.54	33.74	28.05	25.80
P₈	Ap	0-25	42.41	39.60	35.79	28.32
	B	25-46	35.72	31.96	29.47	26.57
	C	46-90	34.08	30.95	28.62	26.03
P₉	Ap₁	0-50	44.94	33.30	29.49	22.99
	AB	50-90	47.15	39.15	33.81	26.80
	B	90-190	46.53	39.11	32.29	25.50
P₁₀	Ap₁	0-45	24.17	21.50	20.67	19.41
	B₁	45-90	37.83	35.38	30.79	29.69
	B₂	90-137	31.53	28.97	23.29	22.54
	C₁	137-170	32.93	27.70	26.26	26.05

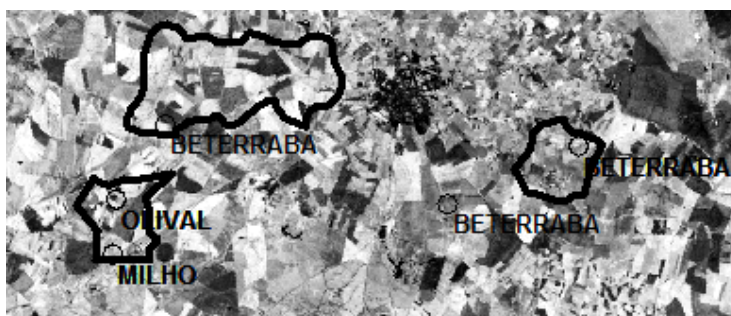
* field capacity

** wilting point

Appendix 3: Soil physical characteristics among sampled locations in Pisos

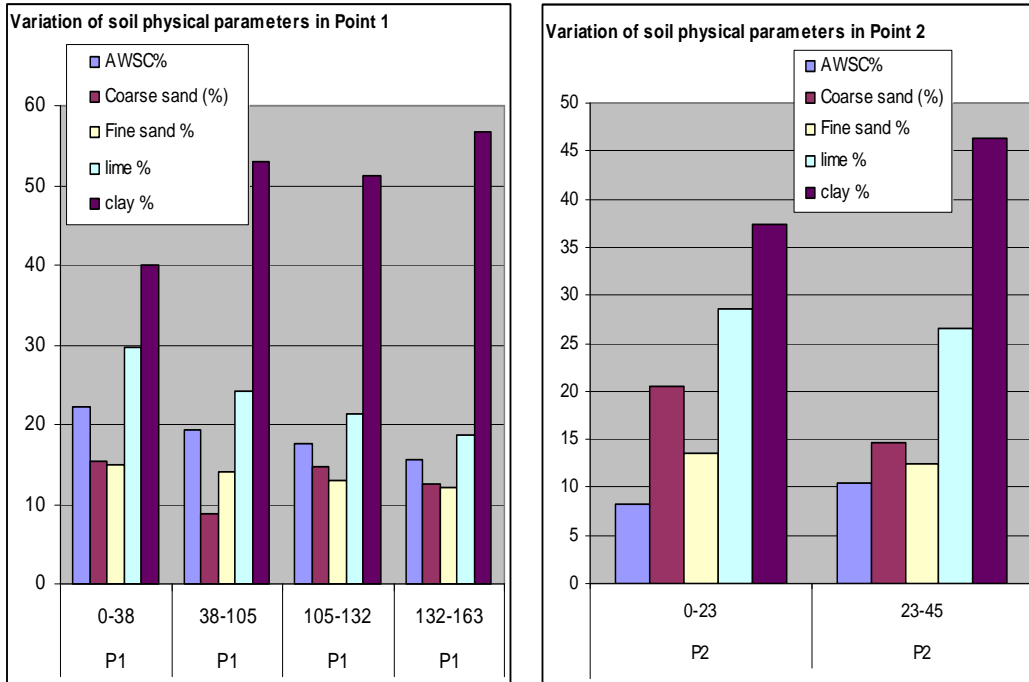
Location	Horiz.	deep. (cm)	Coarse sand (%)	Fine sand (%)	lime (%)	clay (%)	Texture class
P ₁	Ap ₁	0-38	15.43	15.01	29.6	39.97	Argilo-Limoso a Franco-Argilo-Limoso
	B ₁	38-105	8.83	13.99	24.22	52.96	Argilo-Limoso
	B ₂	105-132	14.68	13.01	21.22	51.10	Argiloso
	Bc	132-163	12.50	12.08	18.71	56.71	Argiloso
P ₂	Ap	0-23	20.53	13.57	28.49	37.41	Franco-Argilo-Limoso
	B	23-45	14.60	12.52	26.50	46.38	Argilo-Limoso
P ₃	Ap	0-30	29.75	11.62	24.82	33.81	Franco-Argiloso
	B	30-52	18.80	12.17	24.41	44.62	Argilo-Limoso
	Bc	52-69	29.48	11.99	19.53	39.00	Franco-Argiloso
P ₄	Ap	0-30	23.48	20.21	23.50	32.82	Franco-Argiloso
	B	30-47	15.60	23.29	22.75	38.36	Franco-Argiloso
	Bc	47-60	37.80	17.66	15.51	29.02	Franco-Argiloso
P ₅	Ap ₁	0-35	9.18	16.72	25.45	48.66	Argilo-Limoso
	B	35-70	16.73	16.55	24.11	42.62	Argilo-Limoso
	Bc	70-84	25.73	18.84	18.92	36.51	Franco-Argiloso

Appendix 4: Location of moisture monitoring spots (2006/2007 growing season) in selected fields in Pisos. At the background is NDVI map in March 2007.

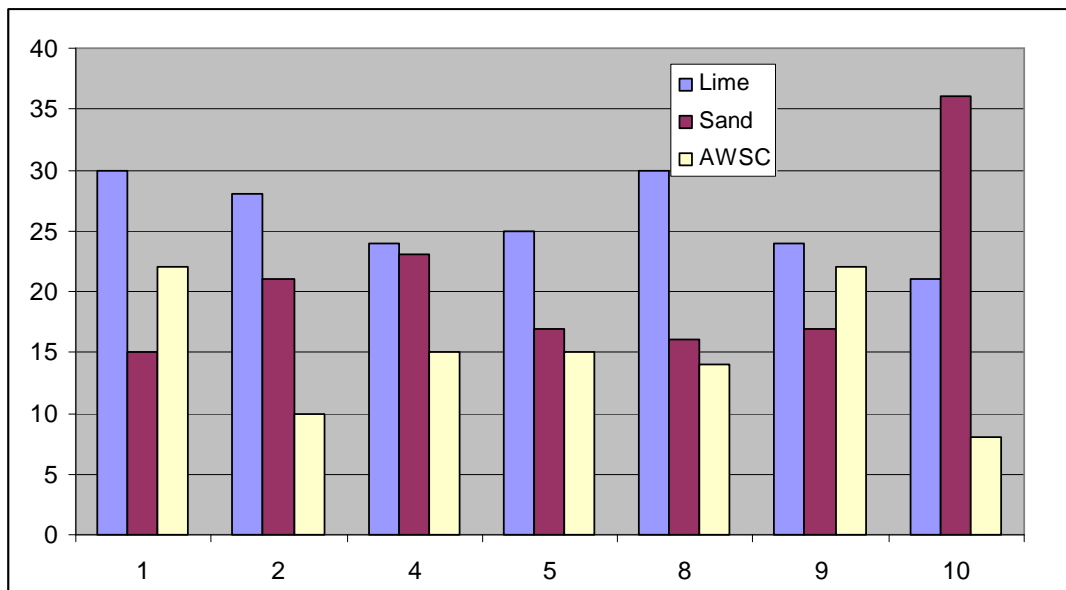


Appendix 5: Exploratory analysis of soil physical parameters and water holding capacity

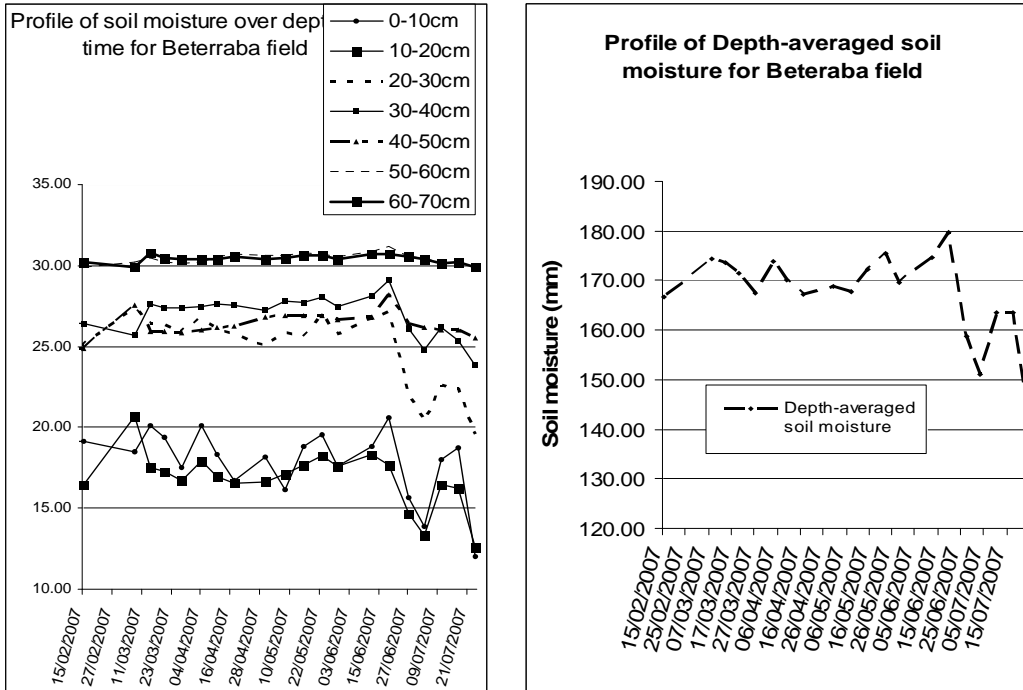
5.1: Soil physical parameters (left is point 1 and right is point 2).



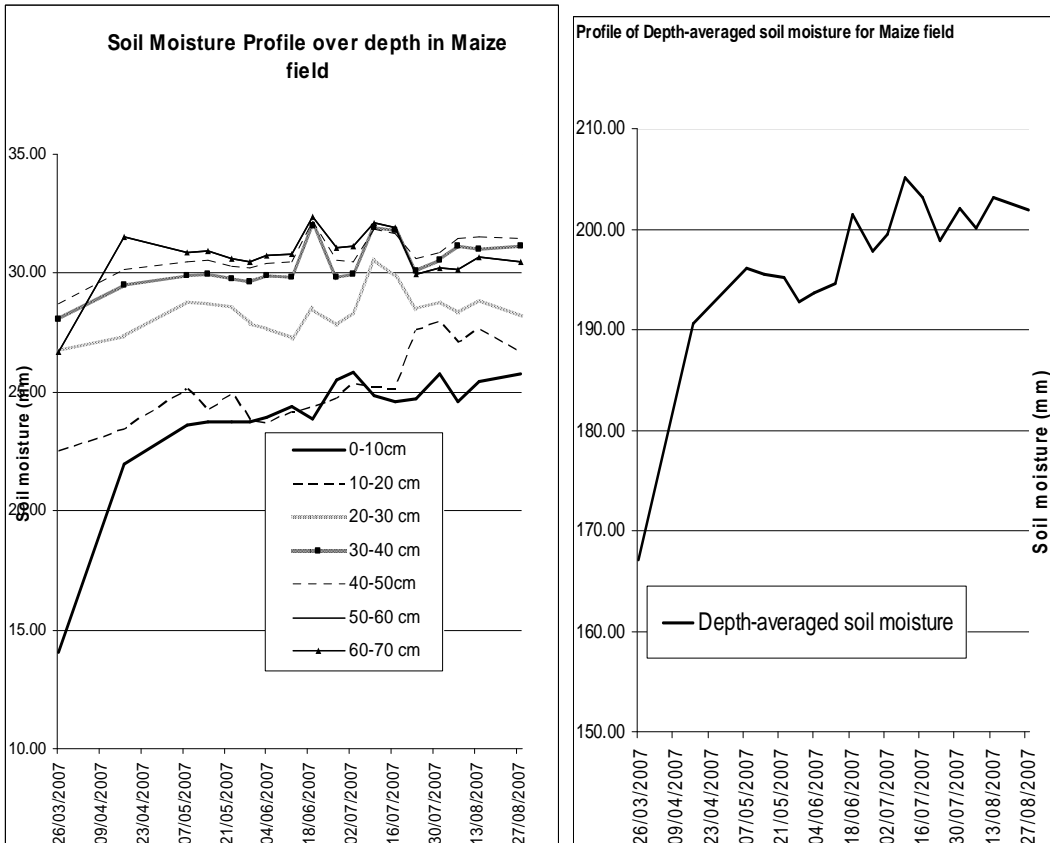
5.2: Proportion of lime, sand and AWSC among the sampled points, (points along x-axis and % along y-axis).



5.3: Soil moisture profile during growing season in beterraba field (left is sampled depths, right is depth-averaged)



5.4: Soil moisture profile during growing season in maize field (left is sampled depths, right is depth-averaged)



Most soils in Pisos are calcareous clayey, and this may explain as to why the proportion of clay is high. The sampled points and depths displayed unique interaction of soil physical constituents, and it was difficult to generalize the nature of the interaction.

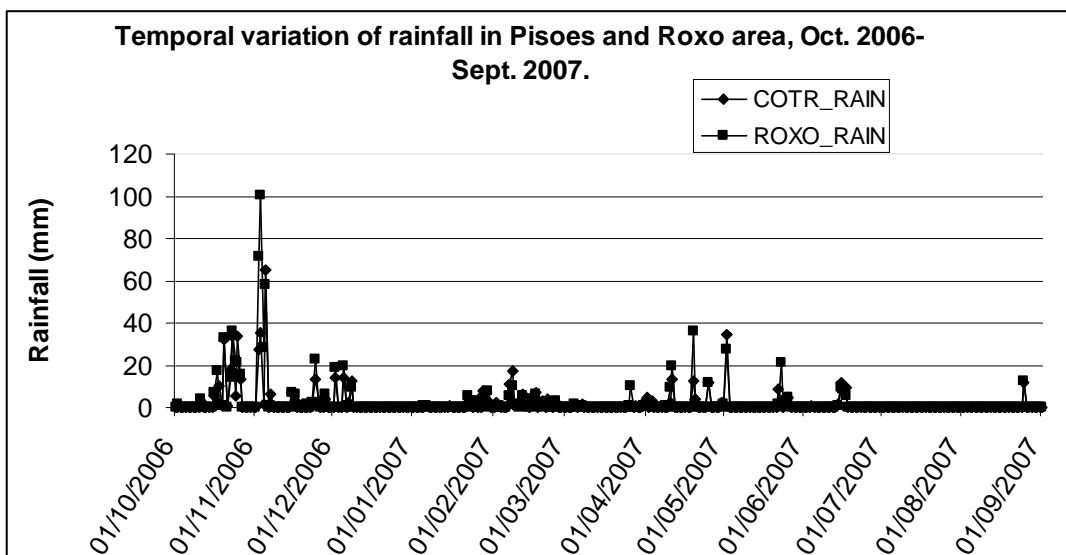
Available water storage capacity was observed to be influenced by the proportion of lime and coarse sand components. Except in sites where coarse sand is relatively high, increase in lime was apparently accompanied with increase of AWSC and vice versa. In sites with relatively high coarse sand content, this influence was blurred and at most reversed. The nature of interaction may be explained by the process of surface tension, which acts to hold available soil water in the soil pores against gravity. Small pores in fine textured soil holds more water than large pores in sandy soils.

The soil moisture profile was characterised by fluctuation especially in the top layers, but the deeper layers were more or less stable. The middle layers observed a steady course for most part of the growing period and then at a later stage (after 19th June 2007), experienced decline of moisture level. This trend was also observed in the overall depth-averaged soil moisture status. The top layers generally experienced a declining moisture status throughout the growing period.

Top soil layers are exposed to atmospheric forcing-stochastic precipitation and /irrigation input and evapotranspiration- and is little influenced by groundwater, whereas for deeper soil layers, soil moisture changes more slowly and remains nearly the same, (De Lannoy 2006). It may also be attributed to phenological stages and management of the crop fields based on information gathered in the field.

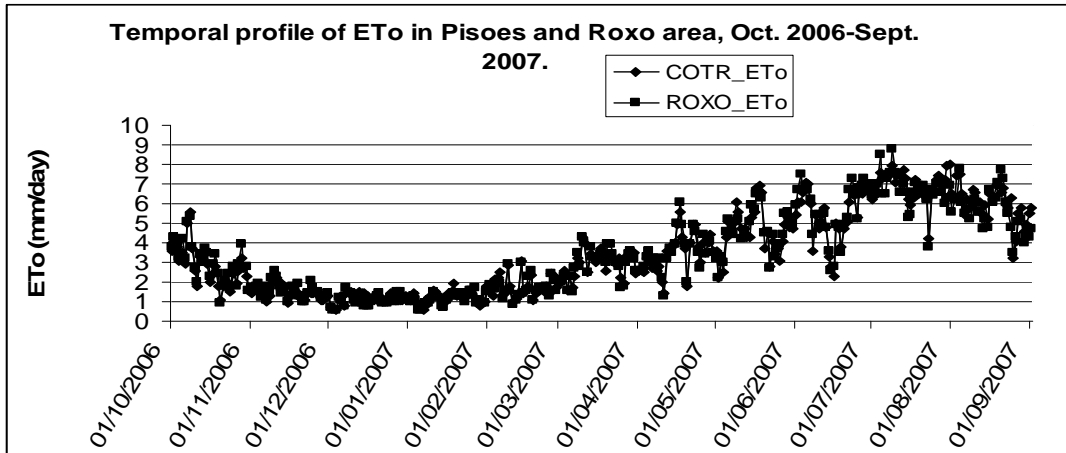
5.5: Exploratory analysis of meteorological input data

5.5.1: Temporal of variation of rainfall (Oct. 2006 -Sep 2007) in Pisos catchment and Roxo area.



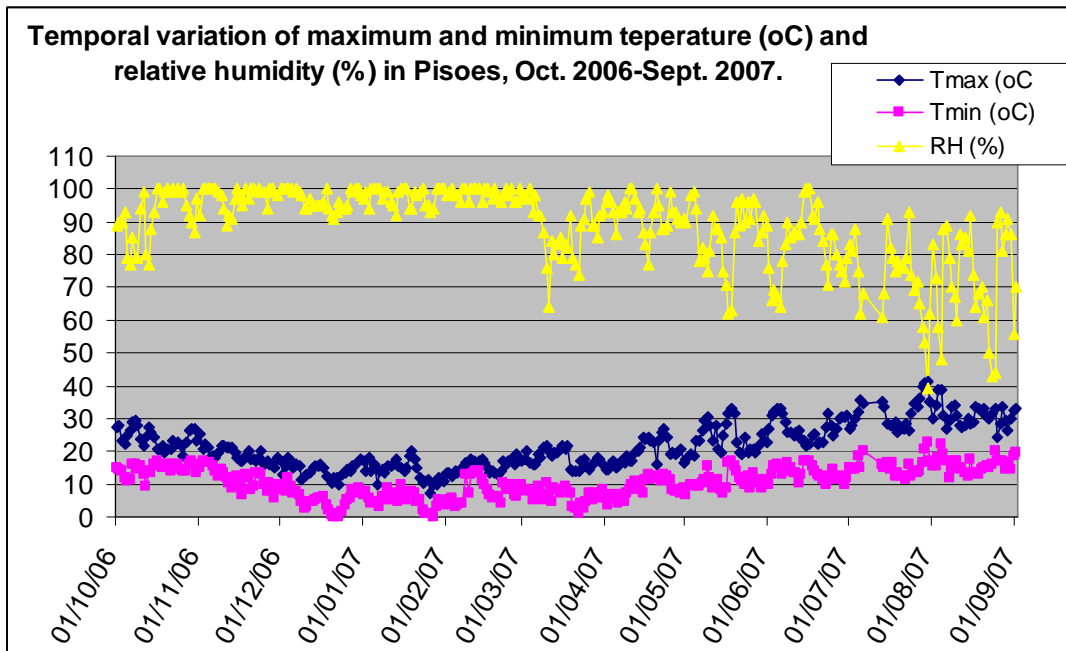
Between October 2006 and September 2007, rainfall pattern was characterized by three distinct periods. The first period was occasioned by heavy rains, recorded end of October, November and in December 2006. The second period (February) had reduced volume but frequency of occurrence was high. March was generally a dry month. The third period was in April, characterized by low amount of rainfall and with low frequency of occurrence. Spring rainfall events and amount were recorded in subsequent months.

5.5.2: Temporal of variation of reference evapotranspiration (ET_o) (Oct. 2006 -Sep 2007) in Pisos catchment and Roxo area.



Evolution of ET_o over the same period was characterized by a gradual decline from October (about 4.3 mm/day), with lowest values observed between December and January (about 1 mm/day). During the subsequent period, ET_o increased gradually, peaking in July (about 7.3 mm/day) followed by a gradual decline.

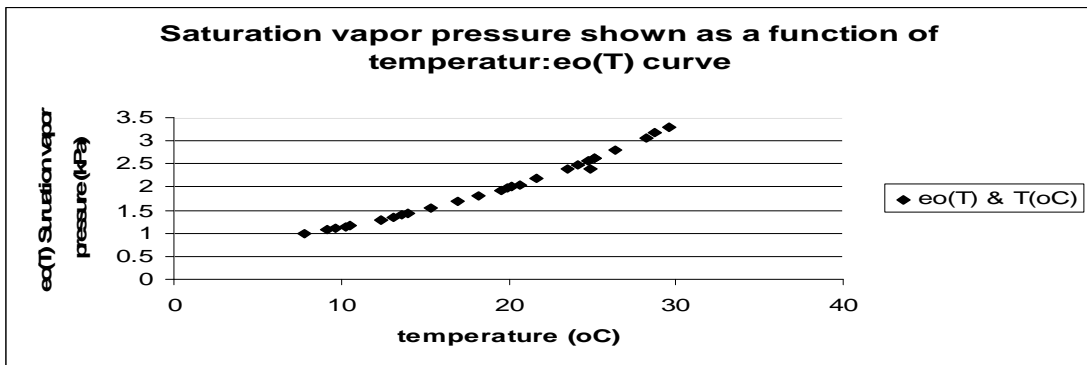
5.5.3: Temporal variation of temperature, relative humidity and precipitation measured at ITC-ADAS (Oct 2006-Sept 2007).



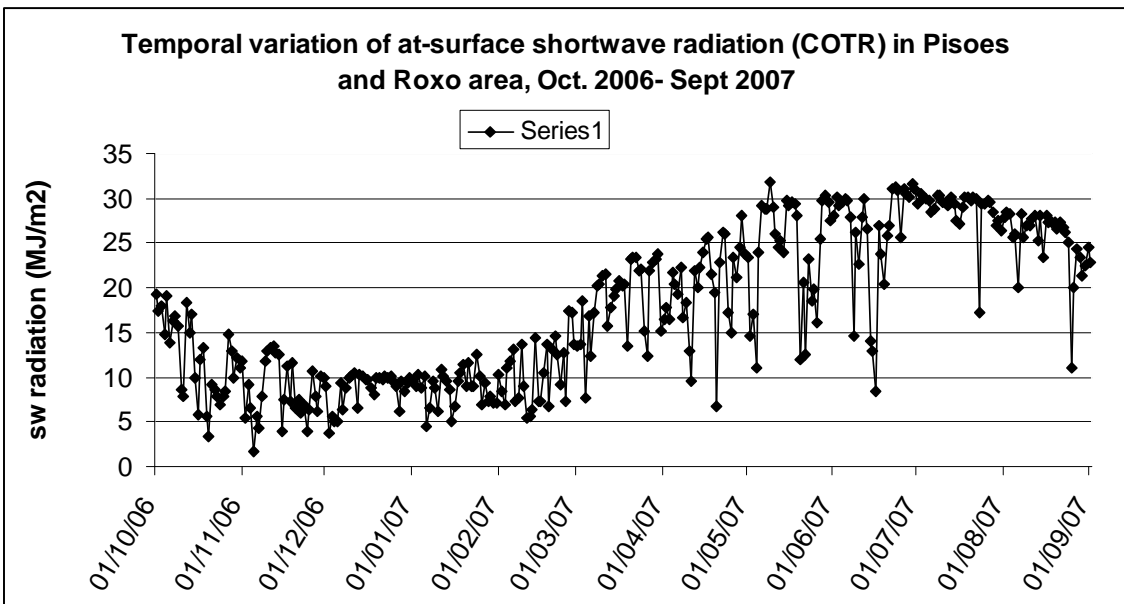
5.5.4: Relationship of saturation vapor pressure and air temperature measured in ITC-ADAS station

Relative humidity was low beginning of October, rising thereafter to saturation level. In March, the level was quite low and in subsequent months, it was occasioned by fluctuations and general decline. Temperature declined from October (about 27°C maximum), with lowest values observed between December and January (about 9°C maximum). In subsequent months, temperature gradually increased peaking end of July (about 40°C maximum).

The contrasting behaviour of relative humidity and temperature is primarily because of the relationship between the two climatic variables. The number of water molecules that can be stored in the air depends on the temperature. The higher the air temperature, the higher is the storage capacity and the higher its saturation deficit, i.e., the difference between actual vapor pressure and saturation vapor pressure.



5.5.5: Temporal variation of at-surface shortwave radiation in Pisos and Roxo area, (Oct. 2006-Sept. 2007).



Shortwave radiation declined in October (from 19 MJ/m²) through December and January (from 9 MJ/m²). During the subsequent period, it increased gradually, peaking end of June (from 31 MJ/m²) followed by a gradual decline. This oscillation of shortwave radiation seems

to be in agreement with the known seasonal cycle of the study area influenced by the position of the sun.

Appendix 6: Description of Remotely sensed data

6.1: MODIS Products

Moderate Resolution Imaging Spectroradiometer, flown on board Terra satellite, is one of the five sensors onboard. Terra was the first Earth Observing System (EOS) launched by NASA on DECEMBER 18, 1999. Terra is at an altitude of 705 km and has a cross track and along track swath of 2330 and 10km respectively, with a global coverage of 1 or 2 days. It has 36 spectral bands between 0.405 and 14.385 μm whose spatial resolutions range from 250 to 500 and 1000m. MODIS Team does process different data products to support study of earth processes. In the present study, data products of land were used, available in hierarchical data format (HDF) and were obtained from EOS Data Gateway (<http://edcimswww.cr.usgs.gov/pub/imswelcome/>).

6.1.1: MODIS data used in the study

Long-name	Frequency	Resolution	usage
MOD11A1 Land Surface Temperature/Emissivity Daily L3 Global 1km			
LST Day 1 km	Daily	1km	Surface Temperature, T_0
Emissivity Band 31	Daily	1km	
Emissivity Band 31	Daily	1 km	Emissivity
MOD09GHK Surface Reflectance Daily L2G Global 500m			
Band1-7	Daily	500m	Albedo
MOD09GA Surface Reflectance Daily L2G Global 500m			
Band1-7	Daily	500m	Albedo
MOD09GQK Surface Reflectance Daily L2G Global 250m			
Band1 &2	Daily	250m	NDVI
MOD09GQ Surface Reflectance Daily L2G Global 250m			
Band1 &2	Daily	250m	NDVI

Daily Land Surface Temperature & Emissivity Product (MOD11A1) V004 (collection 4 for 2006) and V005 (collection5 for 2007) were used for surface thermal measurements. This is a level-3 product that includes values generated in sinusoidally projected tiles by mapping the level-2 LST product on 1-kilometer (0.928km) grids. It comprises daytime and nighttime LSTs, quality assessment, observation times, view angles, clear sky coverage and emissivities estimated in Bands 31 and 32 from land cover types. LST is retrieved from TIR data only in clear sky conditions. Thus, it is defined by the radiation emitted by the land surface observed by MODIS at the instantaneous viewing angle. LST is calculated using

generalized split window algorithm for those pixels whose emissivities are known in bands 31 & 32.

Terra Surface Reflectance daily products (MOD09) were also used in this study. Derivation of higher level products from remotely sensed estimates requires that the top of the atmosphere signal be converted to surface reflectance. With respect to MODIS sensor, the Land Surface Reflectance Science Computing Facility is responsible for applying correction algorithms and associated processing code to already processed MODIS level 1B radiances, finally generating the surface reflectance product.

MODIS Surface Reflectance is a seven-band product computed from the MODIS Level 1B land bands 1, 2, 3, 4, 5, 6, and 7 (3 visible red and 4 infrared). The product is an estimate of the surface spectral reflectance for each band as it would have been measured at ground level as if there were no atmospheric scattering or absorption. It corrects for the effects of atmospheric gases, aerosols, and thin cirrus clouds. The correction is achieved by means of a look-up table which provides the transmittances and path radiances for a variety of sun-sensor geometry's and aerosol loadings. This product is freely downloadable from MODIS WEBSITE <http://edcdaac.usgs.gov/modis/mod09gav5.asp>.

Scientific data sets (SDS) of surface reflectance of both 250m and 500m resolution were used in this study. MOD09GQK (collection 4 for 2006) and MOD09GQ (collection5 for 2007) contains SDS for band 1 and band 2 with a resolution of 250m and were employed in generation of NDVI. MOD09GHK and MOD09GA (collection 4 and 5 respectively), contain SDS of Band 1 to 7. They were used in calculation of broadband albedo.

6.1.2: MODIS channels 1 to 7 and their respective wavelength

CHANNEL	1	2	3	4	5	6	7
WAVELENGTH (μm)	0.648	0.858	0.470	0.555	1.240	1.640	2.13

The study employed twenty four series beginning October 2006 to September 2007 of LST and emissivity measurements and the surface reflectance products.

6.2: Landsat TM 5

Thematic Mapper (TM) data of 9th March and 1st September 2007 were used in this study, acquired from Eurimage (<http://www.eurimage.com>). TM is a sensor on board the Landsat 5 satellite and its data are one of the most used for environmental studies, (Sobrino, Jimenez-Munoz et al. 2004). It is composed of seven bands, six of them in the visible and near infra-red, and only one band located in the thermal infra-red region.

6.2.1: Wavelengths and band resolution of Landsat TM

Band	Wavelength	Resolution
1	490 +/- 60 nm	30m
2	575 +/- 75 nm	30m
3	670 +/- 70 nm	30m
4	837 +/- 107 nm	30m
5	1692 +/- 178 nm	30m
6	11457 nm	120m
7	2190 +/- 215 nm	30m

6.3: Determination of coefficient established between LST and shortwave radiation for selected cover types in Pisos and Roxo area.

Cover type	Beterraba	Rice	Olive grooves	Maize (Pisos)	Maize (Roxo)	Wheat
R ²	0.84	0.83	0.81	0.80	0.79	0.76

6.4: Determination of coefficient established between LST and surface and depth-averaged soil moisture in Beterraba and maize fields in Pisos.

	Beterraba field	Maize field
Surface layer	No correlation	Positive; R ² =0.64
Depth-averaged	Negative; R ² =0.24	Positive; R ² =0.65

Appendix 7: Pre-processing of Landsat TM 5 remotely-sensed inputs parameters

7.1 Processing of Land Surface Temperature estimated from band 6 Landsat TM

From Landsat TM image, surface temperature was evaluated from band 6 (10.4-12.5 μm) which measures emitted long-wave radiation from the earth surface and atmosphere. The grey levels of Landsat TM data, given as digital number (DN) ranging from 0 to 255, were converted to at-satellite radiance based on equation applied by (Roerink, Su et al. 2000), (Qin, Karnieli et al. 2001) and (Wu 2006) expressed as:

$$L_{6,TOA}(\lambda) = 0.1238 + (1.560 - 0.1238) * DN / 255 \quad 7.2.1E$$

At-satellite temperature (T_{sat}) was then derived from the spectral radiance, following equation applied by (Roerink, Su et al. 2000) and (Qin, Karnieli et al. 2001), and expressed as:

$$T_{sat} = 1260.56 / [\ln\{1 + 60.776 / (L_{6,TOA}(\lambda))\}] \quad 7.2.2E$$

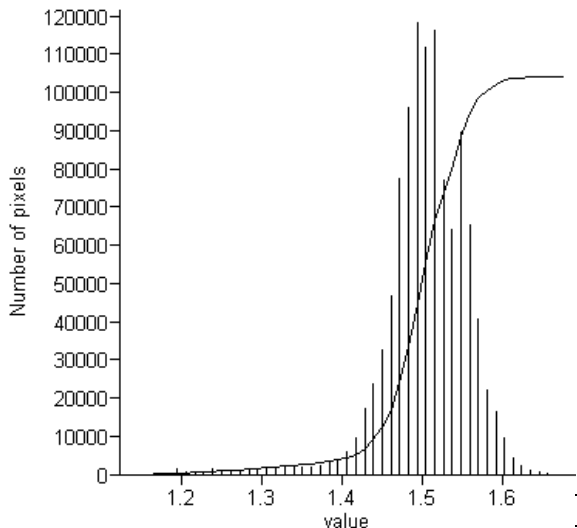
In (Wu 2006), different constants were used to evaluate at-satellite radiant temperature of TM6 at maximum accuracy:

$$T = k_2 / \ln(1 + k_1 / L_{6,TOA}(\lambda)) \quad 7.2.3E$$

where k₁ = 67.162 mWcm⁻²sr⁻¹ and k₂ = 1284.3 K (Kelvin degrees)

Comparison of the two equations (7.2.2E and 7.2.3E) in retrieval of radiant temperature of JD 244 showed slight deviation, (1.5K). In this study, equation 7.2.2E was employed.

7.1.1: Histogram of differenced image between radiant temperature of Landsat TM6, estimated using the two equations.



The atmospheric effects to electromagnetic radiation cannot be ignored when considering the application of Landsat TM6 data for surface temperature estimation. Radiance travelling through the atmosphere will be attenuated by absorption of the atmosphere in the wavelength. Moreover, as noted by (Qin, Karnieli et al. 2001), the atmospheric upwelling will combine with the ground thermal radiance to reach the sensor in space.

In (Roerink, Su et al. 2000), atmospheric correction was performed to the at-satellite values by linking the latter to the surface measured values. In this way, the upward atmospheric thermal radiance and the reflected atmospheric radiance from the observed radiance at satellite level was removed so that the brightness temperature at ground could directly be retrieved. In this study, corresponding surface measured values for the day/time of image acquisition were lacking.

Mono-window algorithm developed and validated by (Qin, Karnieli et al. 2001) and also used successfully by (Sobrino, Jimenez-Munoz et al. 2004) was used to retrieve surface temperature (T_s) from at-satellite radiant/brightness temperature. The algorithm is expressed as:

$$T_s = [a_6 (1-C_6-D_6) + (b_6 (1-C_6-D_6) + C_6+D_6) T_6 - D_6 T_{a\text{eff}}] / C_6 \quad 7.2.4E$$

where:

$$C_6 = \epsilon_0 \tau$$

$$D_6 = (1 - \tau) [1 + (1 - \epsilon_0) \tau]$$

ϵ_0 = land surface emissivity

τ = total atmospheric transmissivity

T_6 = at-satellite radiant/brightness temperature

$T_{a\text{eff}}$ = represents the mean atmospheric temperature

$$a_6 = -67.355351$$

$$b_6 = 0.458606$$

According to (Qin, Karnieli et al. 2001), provided that ground emissivity is known, the computation of LST from TM6 data is dependent on determination of atmospheric transmittance τ for band 6 and effective mean atmospheric temperature $T_{a\text{eff}}$. The former (τ) was resolved using simple linear equation established by (Qin, Karnieli et al. 2001), given for high and low temperatures respectively, for specified ranges of water vapor

For $w = 1.6 - 3.0 \text{ gcm}^{-2}$

$$\tau = 1.031412 - 0.11536w \quad (\text{high temperature}) \quad 7.2.5E$$

$$\tau = 1.053710 - 0.14142w \quad (\text{low temperature}) \quad 7.2.6E$$

For $w = 0.4 - 1.6 \text{ gcm}^{-2}$

$$\tau = 0.974290 - 0.08007w \quad (\text{high temperature}) \quad 7.2.7E$$

$$\tau = 0.982007 - 0.09611w \quad (\text{low temperature}) \quad 7.2.8E$$

where $w \text{ (gcm}^{-2}\text{)}$ is the total amount of atmospheric water vapor in the vertical column of surface unity between the Earth's surface and the sensor, (Table 4). For JD 68 and 244, equations 7.2.7E and 7.2.5E respectively were employed in estimation of atmospheric transmissivity.

For approximation of $T_{a\text{eff}}$ from the near surface air temperature (T_a) (which is easily available from meteorological stations), the authors have developed simple linear relations for standard atmospheres.

$$\text{For mid-latitude summer:} \quad T_{a\text{eff}} = 16.0110 + 0.92621 T_a \quad 7.2.9E$$

For mid-latitude winter: $T_{\text{aeff}} = 19.2704 + 0.91118 T_a$ 7.2.10E

where both T_{aeff} and T_a have dimensions in Kelvin degrees. The equation implies that under the standard atmospheric distributions (clear sky and without great turbulence), the effective mean atmospheric temperature T_{aeff} is a linear function of near-surface air temperature T_a . For JD 68 and 244, equations 7.2.10E and 7.2.9E respectively were employed in estimation of effective air temperature.

7.2: Processing of Surface emissivity estimated from Landsat TM 5

Estimation of surface emissivity (ϵ_0) followed an empirical approach applied by (Hurtado and Sobrino 2001) and (Roerink, Su et al. 2000), which models a given surface considering it as constituted by a mixture of bare soil and vegetation:

$$\epsilon_0 = \epsilon_v P_v + \epsilon_g (1 - P_v) + 4 < d\epsilon > P_v (1 - P_v) \quad 7.3.1E$$

with ϵ_v =emissivity of full vegetation

ϵ_g =emissivity of bare soil

P_v =fractional vegetation cover

$< d\epsilon >$ =vegetation structure parameter, a term that depends on the surface characteristics and which takes into account the internal reflections (cavity effects)

According to (Hurtado and Sobrino 2001), this methodology can be used for the mixed pixels because the narrow interval of the emissivity values of the land natural surfaces in the 10.5–12.5 μm (from 0.94 for bare soils to 0.99 for fully vegetated areas).

For the broadband thermal region 8-14 μm , ϵ_v and ϵ_g were set respectively at 0.972 and 0.947+0.005, typical for full vegetation ((Sobrino, Jimenez-Munoz et al. 2004)) and considering the calcareous soil in the region. Since band 6 has a narrow spectral range, calibration of these emissivities was requisite, and performed using AHAS algorithm as:

$$e_{o\ b6s} = a_s * e_{o\ 8-14\ \mu\text{m}} + b_s \quad \text{for narrowband } \epsilon_g$$

$$e_{o\ b6v} = a_v * e_{o\ 8-14\ \mu\text{m}} + b_v \quad \text{for narrowband } \epsilon_v \quad 7.3.2E$$

Estimation of proportion of vegetation cover (p_v) followed the AHAS procedure, expressed as:

$$P_v = \frac{1 - NDVI / NDVI_g}{(1 - NDVI / NDVI_g) - K \cdot (1 - NDVI / NDVI_v)}$$

$$K = \frac{CH2SUR_v - CH1SUR_v}{CH2SUR_g - CH1SUR_g}$$

7.3.3E

Where:

'K' is the ratio between the difference of the reflectance of the fully vegetated pixel in CH2SUR and CH1 SUR by the same difference but for the bare soil pixel. It is an image constant. CH1SUR and CH2 SUR are atmospherically corrected reflectance of TM band 3 and band 4 respectively, (see Appendix 7.1). P_v is the vegetation proportion map. $NDVI_g$ and $NDVI_v$ are image constant values that might correspond to the minimum (no-water) and maximum NDVI in the reference image.

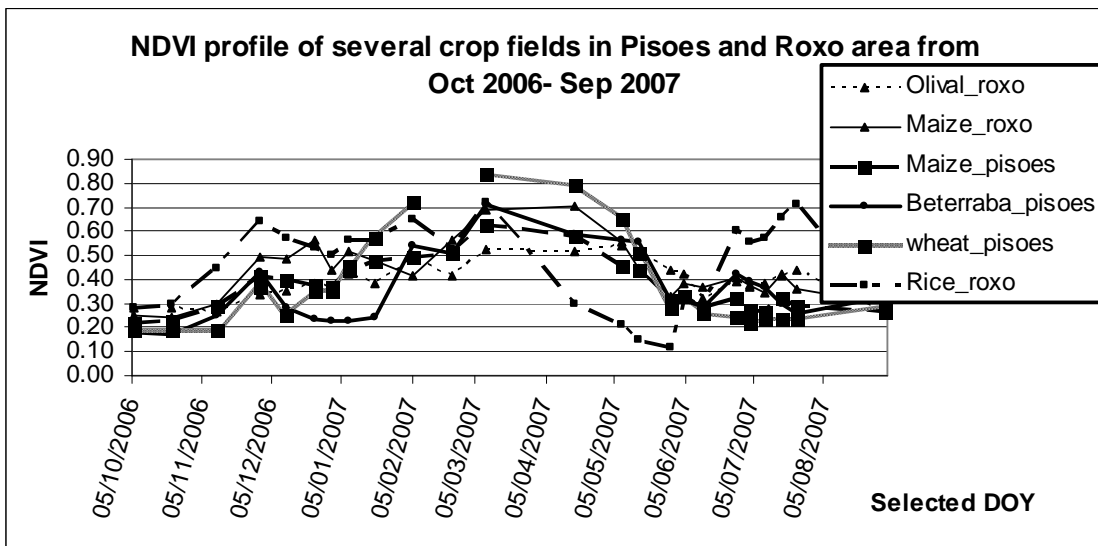
The vegetation structure parameter, $\langle de \rangle$, was estimated following the approach of (Sobrinho, Jimenez-Munoz et al. 2004), expressed as:

$$\langle de \rangle = (1 - e_{0.66s}) * (1 - P_v) F e_{0.66v} \quad 7.3.4E$$

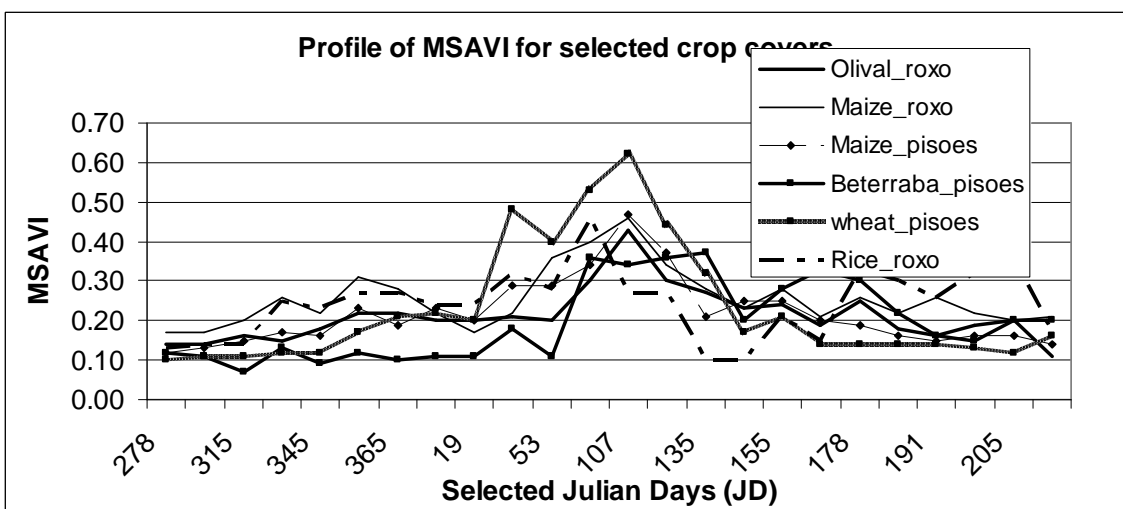
where F is a shape factor whose mean value. Assuming different geometrical distributions is 0.55. These parameters were then input into equation 7.3.1E to yield surface emissivity map for Landsat TM images.

Appendix 8: Estimates of normalized difference vegetation index (NDVI) and modified soil adjusted vegetation index (MSAVI)

8.1: Temporal variation of NDVI of selected crop cover types in Pisos and Roxo area from Oct 2006-Sept 2007.



8.2: Temporal variation of MSAVI of selected crop cover types in Pisos and Roxo area from Oct 2006-Sept 2007.



Appendix 9: Procedure to derive net radiation from MODIS and Landsat TM 5 data

Implementation of equation 16 entailed determination of input parameters, primarily from remote sensing data, MODIS and Landsat TM 5.

9 A: Estimation of Albedo

9. A.1: MODIS Albedo

According to MODIS Science Team, Albedo is related to land surface reflectance by directional integration and is therefore dependent on the BRDF, which describes how the reflectance depends on view and solar angles. Specification of BRDF provides land surface reflectance explicitly in terms of its spectral, directional, spatial and temporal characteristics. The output of this specification is band-specific albedos that are purely properties of the surface and do not depend on the state of the atmosphere. They can be used with any atmospheric specification to provide true surface albedo. A 16-days composite MOD4383 Albedo product is freely downloadable from above MODIS Website.

However, in (Nishida, Nemani et al. 2003), daily surface albedo values used to run the algorithm for MOD16 ETa product were derived from simple weighted average of band reflectance values. Because estimates of daily albedo were required in this study, similar approach was followed, with shortwave broadband albedo computed according to (Wu 2006):

$$toa = \sum_{i=1,2,3,4,5,7} weight \times reflectance(band_i)$$

9. A.1.1E

where toa is albedo at top of atmosphere (dimensionless) and weight is band dependent weighting coefficient (Appendix 9 A.1.1), which allows for spectral-to-broadband conversion. These conversion factors are derived for typical average cases albedo, (http://modis.gsfc.nasa.gov/data/atbd/atbd_mod09.pdf).

9 A.1.1: MODIS spectral-to-broadband conversion coefficients

SPECTRAL-TO-BROADBAND CONVERSION COEFFICIENTS

Band	Wavelength	VIS-BB	NIR-BB	SW-BB
<i>MODIS (from Liang et al. [37])</i>				
Blue	0.459–0.479	0.4364	0.0000	0.3489
Green	0.545–0.565	0.2366	0.0000	–0.2655
Red	0.620–0.670	0.3265	0.0000	0.3973
NIR	0.841–0.876	0.0000	0.5447	0.2382
1.2	1.230–1.250	0.0000	0.1363	0.1604
1.6	1.628–1.652	0.0000	0.0469	–0.0138
2.1	2.105–2.155	0.0000	0.2536	0.0682
Intercept		–0.0019	–0.0068	0.0036

9. A.2: Landsat TM Albedo

The surface albedo was determined by integrating at-satellite spectral reflectance in the six short-wave bands of the Landsat 5 image and then applying a correction based on the general air transmittance, (Tasumi 2005). Spectral-to-planetary broadband albedo (at the top

of atmosphere) was then calculated as weighted sum of the different in-band planetary albedos as in equation 9.A.1.1E. Weights for different bands are presented in Table 3.

The planetary shortwave albedo of Landsat TM has to be corrected for atmospheric distortions to obtain realistic surface albedo values. In (Roerink, Su et al. 2000), this was carried out by performing a linear regression between measured surface albedo and planetary albedo and stretching the fitted equation over the planetary albedo.

In this study, method employed to perform atmospheric correction was based on the expression used by (Wu 2006):

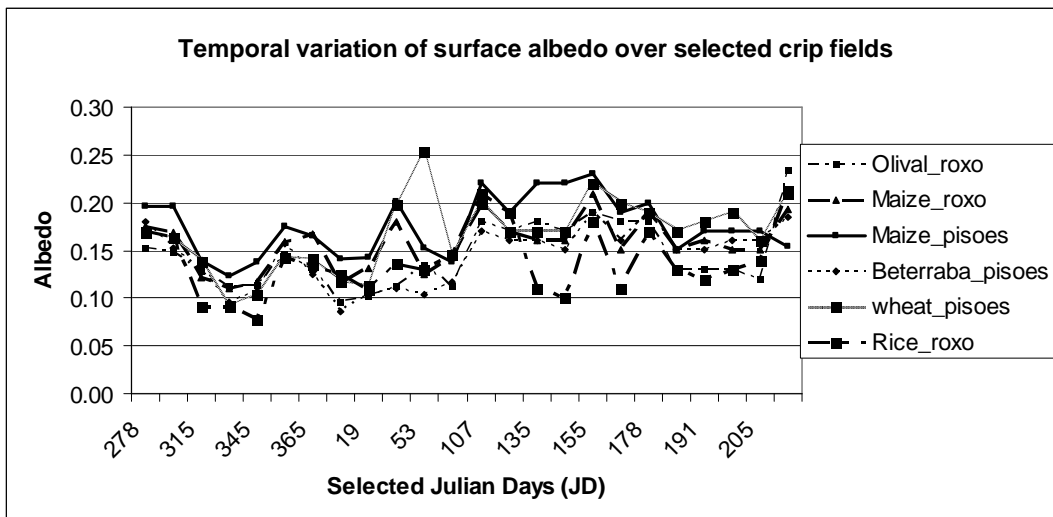
$$\alpha = [(toa)-pathradiance] / \tau^2 \quad 9.A.2.1E$$

where (τ) is atmospheric transmissivity, in this study calculated as the ratio of surface shortwave radiation measured at COTR weather station (Beja City) to at-sensor shortwave radiation. For JD 68 and 244, estimated values of $\tau = 0.804$ and 0.679 respectively were applied. Path radiance was retrieved from the planetary albedo map, as the value of a point in open water body. At supposedly the deepest point in Roxo dam, path radiances were 0.043 and 0.063 in JD 68 and 244 respectively. This value deviates slightly from the typical range noted by (Wu 2006) ($0.025-0.04$). Slight deviation (0.01 and 0.07) for JD 68 and 244 respectively were observed. In clear sky days as JD 68 and 244, low levels of atmospheric noises are expected.

9. A.3: Comparison of the range of albedo values used in this study and those reviewed from literature, (Conrad 2007).

Range of Albedo values used in this study		Values employed by (Conrad 2007)		Values reviewed by (Conrad 2007) (Ranges)
Min	Max	Min	Max	
0.09	0.25	0.182	0.014	0.14-0.22; 0.16-0.22; 0.16-0.23

9. A.4: Temporal profile of surface albedo over the selected cropping zones in Pisos/Roxo (Oct. 2006- Aug. 2007).



9. A.5: Determination of coefficient established between Albedo and shortwave radiation for selected cover types in Pisos and Roxo area.

Cover type	Beterraba	Rice	Olive grooves	Maize (Pisos)	Maize (Roxo)	Wheat
R ²	0.53	0.14	0.33	0.38	0.29	0.32

9. A.6: Determination of coefficient established between albedo and surface and depth-averaged soil moisture in Beterraba and maize fields in Pisos.

	Beterraba field	Maize field
Surface layer	No correlation	Negative; R ² =0.61
Depth-averaged	No correlation	Negative; R ² =0.63

9. B: Solar radiation at the top of atmosphere

According to (Roerink, Su et al. 2000), solar radiation at the top of atmosphere ($K_{\downarrow sun}$) (Wm^{-2}) is determined by its geographic location, day-number and daytime. Taking in account these factors, the equation applied by (Wu 2006) was used, but substituted for the total shortwave broadband instead of specific band, as:

$$K_{\downarrow sun} = S_o \cdot \cos \theta \cdot dr \quad 9.B.1E$$

where S_o is the solar constant at TOA, about $1367 Wm^{-2}$, θ is the solar zenith angle and dr is the inverse relative distance from the earth to the sun, which corrects for the earth's elliptical orbit. $K_{\downarrow sun}$ was calculated using a spreadsheet as a constant value representative of the study area.

9. C: At-surface (downward/incoming) shortwave radiation (K_{\downarrow})

The at-surface shortwave radiation was retrieved from COTR weather station (Beja City). A value for each instantaneous moment (hourly) of satellite over-pass was assumed constant over the whole study area. Atmospheric transmissivity was calculated as the ratio between exo-atmospheric solar radiations to surface solar radiation and was applied to correct broadband albedo values specifically for the case of Landsat TM.

9. D: Reflected shortwave radiation (K_{\uparrow})

For both MODIS and Landsat TM, reflected shortwave radiation was determined from at-surface shortwave radiation (K_{\downarrow}) as a function of albedo (α), expressed as:

$$K_{\uparrow} = \alpha * K_{\downarrow} \quad 9.D.1E$$

K_{\downarrow} was obtained from COTR station (W/m^2) (see Fig. 8), while albedo maps (α) were calculated as detailed in Appendix 9.A.

9. E: Instantaneous Net shortwave radiation

Instantaneous net shortwave radiation (K_n) (W/m^2), was calculated as the residual of at-surface incoming and outgoing shortwave radiation, expressed as:

$$K_n = K_{\downarrow} - K_{\uparrow} \quad 8.E.1E$$

9. F: Incoming longwave radiation

Downward atmospheric longwave radiation (L_{\downarrow}) (Wm^{-2}) is determined predominantly by the humidity and temperature profiles through the atmosphere, (Hurtado and Sobrino 2001). In this study, meteorological data of screen level air temperature and relative humidity were

obtained from ITC-ADAS weather station and assumed to be representative of the whole study area.

Evaluation of incoming long-wave radiation employs numerical models parameterized using multi-interval band and emissivity schemes. The Rapid Radiative Transfer Model (RRTM) reported by (Bisht 2005) for instance, divides the longwave spectrum into 16 intervals and needs information about gases like H₂O, CO₂, O₃ and others.

Simple empirical formulations have been devised. The scheme used by (Bisht 2005), expressed as:

$$L_{\downarrow} = \epsilon_a \sigma T_a^4 \quad 9.F.1E$$

where L_{\downarrow} is the downward longwave radiation (Wm^{-2}), T_a is air temperature (Kelvin) at screen level, $\sigma = 5.67 \times 10^{-8} Wm^{-2}$ is Steffan-Boltzmann constant and ϵ_a (air emissivity) is expressed as:

$$\epsilon_a = [1 - (1 + \xi) \exp \{-(1.2 + 3\xi)^{1/2}\}], \text{ and } \xi = 46.5 e_o / T_a; \text{ and } e_o \text{ is screen level vapor pressure (hPa)} \quad 9.F.2E$$

Another method of estimating atmospheric incoming longwave radiation flux, $L_{\downarrow} (Wm^{-2})$, is one suggested by (Hurtado and Sobrino 2001) and (Gomez 2005), expressed as:

$$R_a = 1.31 \sigma T_a^4 (e / T_a)^{1/7} \quad 9.F.3E$$

where $R_a = L_{\downarrow}$; e is the screen level vapor pressure (hPa).

Another simple relation has been noted by same authors, expressed as:

$$R_a = 0.94 \times 10^{-5} \sigma T_a^6 \quad 9.F.4E$$

Estimate of incoming atmospheric long wave radiation flux derived by the three methods was compared and found not to be deviating much (about 47 W/m^2 between the two extremes). Estimates of equation 9.F.3E were selected for use in subsequent processing.

9. H: Emitted Longwave radiation

Once land surface temperature and surface emissivity maps were calculated for both MODIS and Landsat TM, then emitted longwave radiation, $L^{\uparrow} (Wm^{-2})$, was estimated based on the Stefan Boltzman equation as applied by (Roerink, Su et al. 2000), and (Bisht 2005), and expressed as:

$$L^{\uparrow} = \sigma \epsilon_o T_o^4 \quad 9.H.E.1$$

Where $\sigma = 5.67 \times 10^{-8} Wm^{-2} K^{-4}$ is the Steffan-Boltzmann constant, ϵ_o is surface emissivity and T_o is surface temperature.

9. I: Net longwave radiation

Net longwave radiation was then estimated as the residual of incoming and outgoing longwave radiation, expressed as, (Hurtado and Sobrino 2001):

$$L_n = \epsilon_o L_{\downarrow} - L^{\uparrow} \quad 9.I.E.1$$

where ϵ_o is surface emissivity, L^{\uparrow} is outgoing longwave radiation (Wm^{-2}), and L_{\downarrow} is incoming atmospheric longwave radiation flux at the surface (Wm^{-2}). In this way, the longwave radiation reflected by the surface is accounted.

Generally, Earth surface is a net emitter of long wave radiation, which is then absorbed by the atmosphere or is lost in space. As the outgoing long wave radiation is almost always greater than the incoming long wave radiation, net long wave flux represents an energy loss, (Allen and Fao 1998).

9. J: Instantaneous net radiation

Once the net short and longwave were estimated, it was possible to resolve for instantaneous net radiation as the sum of the two fluxes, expressed as:

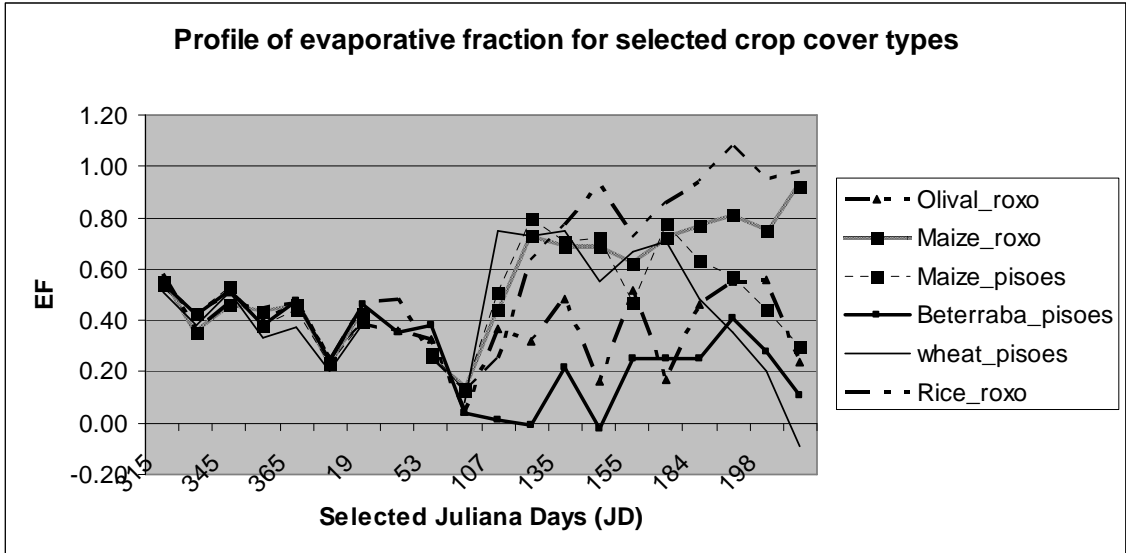
$$R_n = K_{net} + L_{net} \quad 9.J.E1$$

Appendix 10: Relationship between land surface temperature and albedo

10.1: Values of T_H and $T_{\lambda E}$ for different Julian Days as a function of albedo (α).

Julian Day	Date	T_H (K)	$T_{\lambda E}$ (K)
2006			
278	5 th October	-34.323 α +318.46	20.008 α +278.57
285	12 th October	-32.199 α +319.42	6.4776 α +289.41
315	11 th November	-67.685 α +315	21.286 α +281.26
334	30 th November	-11.973 α +296.51	2.1948 α +278.91
345	11 th December	-18.513 α +294.39	5.8986 α +276.44
358	24 th December	-27.037 α +295.42	1.5202 α +271.41
365	31 st December	-40.35 α +301.85	9.7423 α +278.43
2007			
8	8 th January	-12.861 α +294.3	7.0309 α +274.04
19	19 th January	-43.453 α +304.61	6.952 α +277.75
36	5 th February	-17.576 α +297.78	3.6406 α +275.85
53	22 nd February	-17.363 α +300.62	4.9001 α +275.27
68 ^{MODIS}	9 th March	-20.064 α +296.99	108.57 α +267.08
68 TM	9 th March	-49.06 α +309.34	18.797 α +282.54
107	17 th April	-27.29 α +303.96	0.0245 α +295.15
128	8 th May	-62.637 α +321.07	38.12 α +296.49
135	15 th May	-36.413 α +314.31	12.206 α +299.37
149	29 th May	-26.134 α +313.36	6.4121 α +301.25
155	4 th June	-28.128 α +318.35	7.248 α +305.96
163	12 th June	-48.352 α +324.08	6.0844 α +305.65
178	27 th June	-67.194 α +325.42	11.559 α +300.4
184	3 rd July	-86.846 α +328.76	45.812 α +299.84
191	10 th July	-105.6 α +338.11	18.66 α +310.07
198	17 th July	-72.856 α +326.52	32.059 α +302.45
205	24 th July	-36.779 α +321.07	12.622 α +307.75
244 ^{MODIS}	1 st September	-57.051 α +331.41	9.5774 α +290.83
244 TM	1 st July	-19.196 α +324.07	24.078 α +291.06

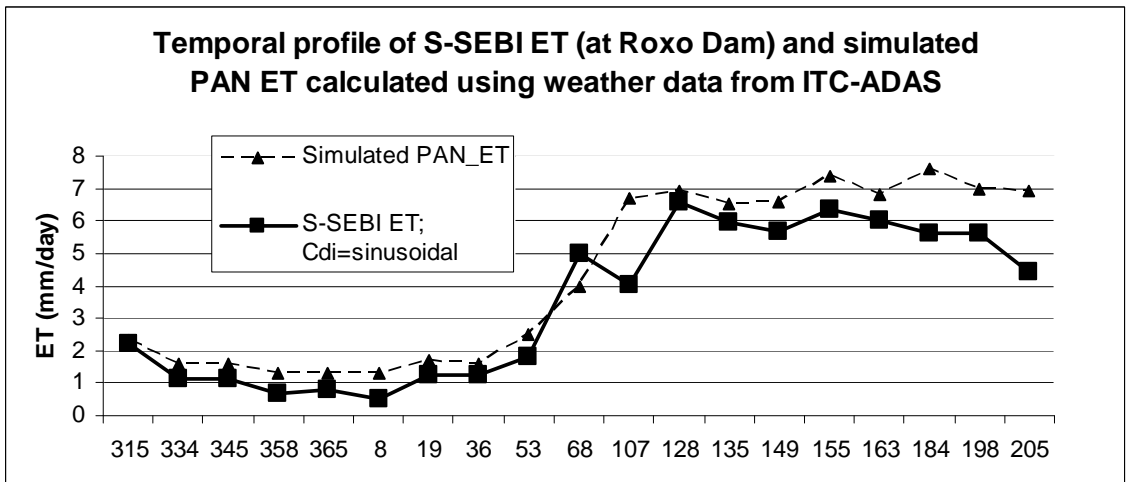
10.2: Profile of evaporative fraction (instantaneous) in Pisos and Roxo area, (Oct. 2006-Sep. 2007).



10.3: Relationship between Evaporative fraction and surface- and depth-averaged soil moisture in Beterraba and maize fields in Pisos.

	Beterraba field	Maize field
Surface layer	No correlation	No correlation
Depth-averaged	No correlation	No correlation

10.4: Linear correlation of S-SEBI ET (extracted at Roxo Dam) with simulated PAN ET calculated using weather data from ITC-ADAS station



Appendix 11: Instantaneous fluxes of soil heat, latent heat and sensible heat

11.1: Soil Heat Flux

The Soil heat flux (G_i) is the energy used for warming or cooling the subsurface soil volume. In (Sobrino, Gómez et al. 2005), soil heat flux was estimated from the net radiation and the Modified Soil Adjusted Vegetation Index (MSAVI) values, expressed as:

$$G_i = R_{ni} - 0.5 \exp(-2.13 \text{MSAVI}) \quad 11.1.1E$$

The soil heat flux profile was positive over the whole growing period, apparently lowest in winter (100 W/m^2) and gradually rising there after. Soil heat flux is positive when the soil is warming and negative when soil is cooling, (Allen and Fao 1998). The observed variation of soil heat flux relates well with the variation of fractional vegetation cover at the time of image acquisition as expressed by MSAVI (see Appendix 8.2). Low MSAVI means low vegetation cover and much exposed soil surface.

11.2: Instantaneous Latent Heat Flux

Instantaneous latent heat flux (λE_i) is the amount of energy used for the evaporation process of the soil and the transpiration process of the plants, (Roerink, Su et al. 2000). It was calculated from the net available energy, soil heat flux and the evaporative fraction as:

$$\lambda E_i = \lambda_i (R_{ni} - G_i) \quad 11.2.1E$$

Since it represents the energy used for evaporation process of the soil and transpiration process of the crops, it would be expected to be proportional to availability of moisture from the evaporative surface. This explains why rice and maize fields in Roxo, with high moisture, apparently had high latent energy, compared to maize and beterraba fields in Pisos that received less water supplement in that order.

11.3: Instantaneous Sensible Heat Flux

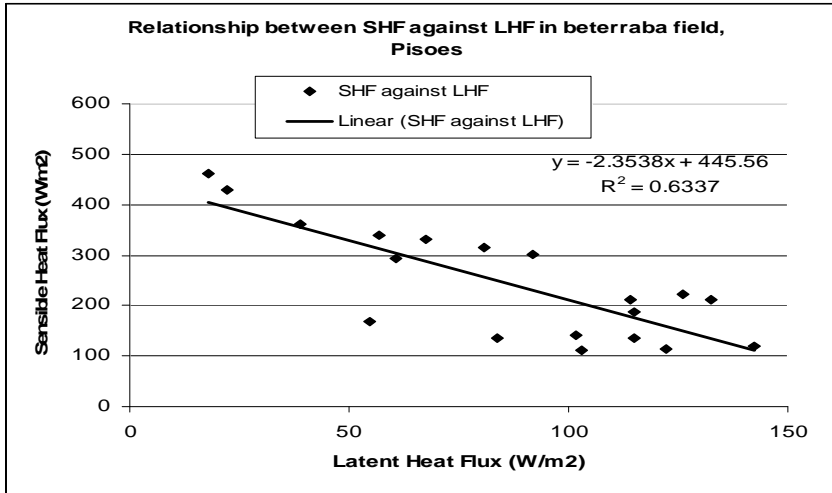
Sensible heat flux (H_i) is the heat transfer between the ground and the atmosphere, enhanced by forced or free convection, (Roerink, Su et al. 2000), being the balance of net radiation less soil heat flux and latent heat flux. Surfaces occasioned by less latent energy will tend to have high sensible heat flux and vice versa. It was calculated from the net available energy and the evaporative fraction as follows:

$$H_i = (1 - \lambda_i) (R_{ni} - G_i) \quad 11.3.1E$$

11.4: Relationship between Latent and Sensible heat flux

In all the selected crop fields, a negative correlation was obtained. In beterraba, rice, maize (Roxo), maize (Pisos), wheat fields and olive grooves, obtained $R^2 = 0.63, 0.46, 0.39, 0.17, 0.15$ and 0.10 respectively in decreasing order.

11.4.1: Relationship between LHF and SHF in beterraba field, Pisoes

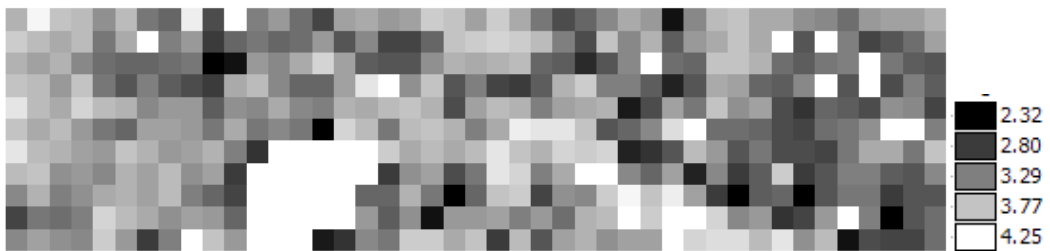


11.5: Dissaggregation of S-SEBI ET

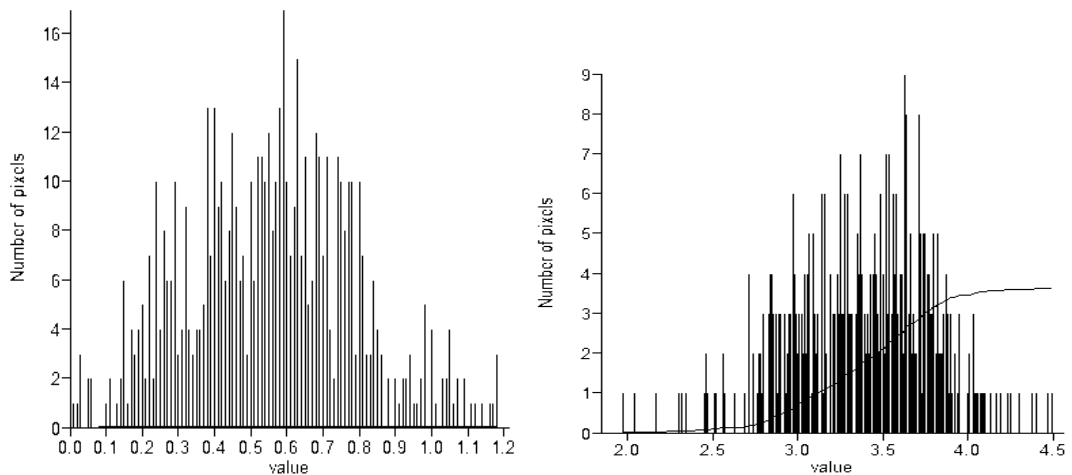
11.5.1: S-SEBI ET derived from original MODIS, JD 68



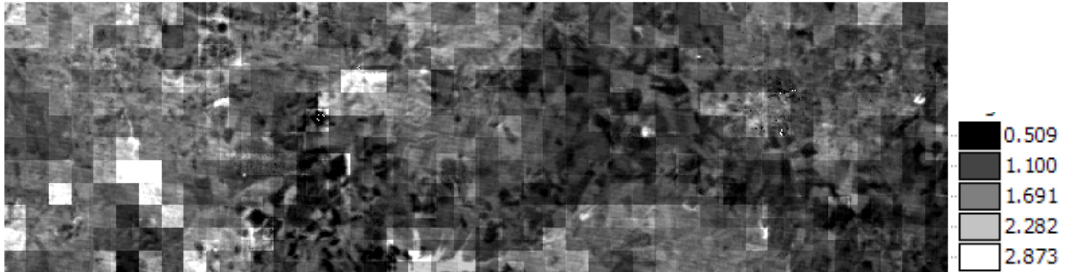
11.5.2: S-SEBI ET derived from aggregated Landsat TM (to MODIS resolution), JD 68



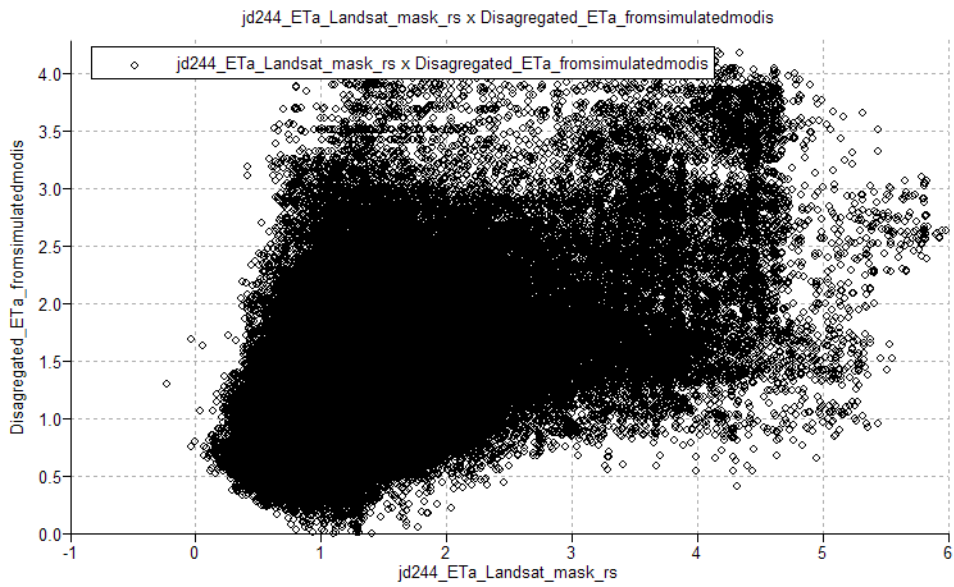
11.5.3: S-SEBI ET, original MODIS (left) and aggregated Landsat TM –MODIS resolution-(right), JD 68.



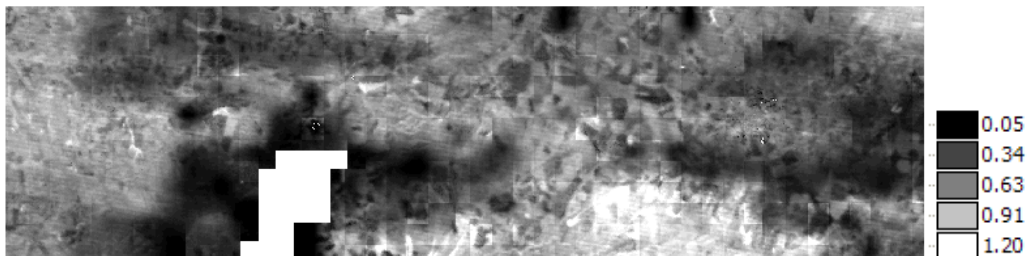
11.5.4: Disaggregated S-SEBI ET map (initially aggregated Landsat TM ET map of JD 244)



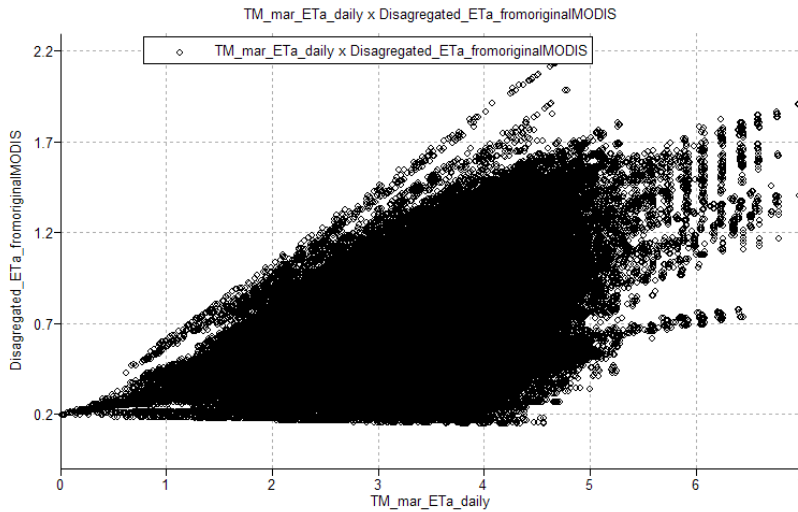
11.5.5: Scatter plot of ET derived from disaggregated Landsat TM S-SEBI ET map and its corresponding original ET map, JD 244



11.5.6: Disaggregated S-SEBI ET map from an original MODIS S-SEBI ET map, JD 68



11.5.7: Scatter plot of ET derived from disaggregated MODIS S-SEBI ET map and its corresponding original Landsat TM ET map, JD 68



**Appendix 12: Evaporative fraction estimated using ‘Universal Triangle’ model
Summary statistics and spatial variability in EF in selected wheat field (based on Universal Triangle model)**

Date	JD	Min	Max	Mean EF	Standard deviation	CV
30-Nov-06	334	0.41	0.47	0.45	0.03	6.67
09-Mar-07	68	0.53	0.57	0.55	0.02	3.64
03-Jul-07	184	0.4	0.44	0.42	0.02	4.76

Appendix 13: Depth averaged soil moisture estimated using statistical model defined in equation 29.

Summary statistics and spatial variability of depth-averaged soil moisture in selected wheat field (based on estimates of Universal Triangle model in JD 334, 68 AND 184).

Date	JD	Min	Max	Mean soil moisture content	Standard deviation	CV
30-Nov-06	334	175	196	186.7	10.7	5.73
09-Mar-07	68	231	252	240.33	10.69	4.45
03-Jul-07	184	166.31	182.33	176.31	7.08	4.02

Appendix 14: Available soil water storage capacity (ASWC) in Pisos catchment



Within the selected wheat area, minimum, maximum and mean AWSC level was respectively 174 mm, 418mm and 316 mm. Variation was substantial (CV=40%) and may be attributed to the variability of soil textural classes which differ in their water holding capacity.

The sites with lowest AWSC has soil texture class “Franco-Argiloso” that has lime and coarse sand content about 21 % and 36 %. Sites with high AWSC has soil class texture class “Argilo-Limoso” that has lime and coarse sand content about 25% and 17%. This proportional interaction of soil physical component bears implication to the process of surface tension, which acts to hold available soil water in the soil pores against gravity. Small pores in fine textured soil holds more water than large pores in sandy soils.

Appendix 15: Estimate of spatially distributed effective rooting depth

15.1: Spatial variation of root depth wheat area estimated based on FAO 56-Kc-NDVI time series approach in wheat field over time

Date	JD	Min	Max	Mean RD	Standard deviation	CV
30-Nov-06	334	0.2	1.29	0.66	0.26	39.39
09-Mar-07	68	0.96	1.8	1.44	0.25	17.36
03-Jul-07	184	0	0.46	0.2	0.12	60.00

15.2: Spatial variation of root depth wheat area estimated based on per image histogram approach in wheat field over time

Date	JD	Min	Max	Mean RD	Standard deviation	CV
30-Nov-06	334	-0.17	1.07	0.34	0.28	82.35
09-Mar-07	68	-0.25	1.8	0.96	0.6	62.50

15.3: Spatial variation of root depth wheat area estimated based on SSEBI Kc-NDVI model in wheat field over time

Estimation of effective rooting depth based on SSEBI Kc-NDVI model was only limited in the middle to end phase. Minimum, maximum and mean estimates were respectively 0.55 m, 1.8 m and 1.24 m. Spatial variability was moderate, (CV=31%).

Appendix 16: Estimation of spatially distributed Total Available Water (TAW)

16.1: Spatial variability of TAW estimates based on FAO 56 Kc-NDVI time series approach

Date	JD	Min	Max	Mean TAW	Standard deviation	CV
30-Nov-06	334	78.39	438.99	198.34	85.55	43
09-Mar-07	68	217.8	735	480.6	156	32
03-Jul-07	184	13.94	164.17	61.75	39.5	64

16.2: Spatial variability of TAW estimates based per image approach

Date	JD	Min	Max	Mean TAW	Standard deviation	CV
30-Nov-06	334	-35.7	360.5	101	85.3	84
09-Mar-07	68	-89.2	714.1	350.1	211.1	60

16.3: Spatial variability of TAW estimates based SSEBI-Kc-NDVI model

TAW estimates of JD 68 were generally high and variable (mean=432.4 mm and CV=39%).

Appendix 17: estimation of spatially distributed depletion fraction (p)

17.1: Spatial variability of Depletion factor estimated on the basis of FAO 56 Kc-NDVI time series

Date	JD	Min	Max	Mean DEPLETION-FACTOR	Standard deviation	CV
30-Nov-06	334	0.7	0.73	0.72	0.01	1.39
09-Mar-07	68	0.6	0.65	0.63	0.02	3.17
03-Jul-07	184	0.59	0.66	0.63	0.02	3.17

17.2: Spatial variability of Depletion factor estimated on the basis of per image approach

Date	JD	Min	Max	Mean DEPLETION-FACTOR	Standard deviation	CV
30-Nov-06	334	0.71	0.75	0.73	0.02	2.74
09-Mar-07	68	0.62	0.75	0.68	0.04	5.88
03-Jul-07	184	0.68	0.75	0.72	0.02	2.78

17.3: Spatial variability of Depletion factor estimated on the basis of S-SEBI Kc-NDVI model

Date	JD	Min	Max	Mean DEPLETION-FACTOR	Standard deviation	CV
09-Mar-07	68	0.65	0.68	0.67	0.01	1.49
03-Jul-07	184	0.62	0.65	0.64	0.01	1.56

Appendix 18: Estimation of unready available moisture (xp= {1-p} TAW)

18.1: Spatial variability of unready available water (xp) estimated based on FAO 56 Kc-NDVI time series approach.

Date	JD	Min	Max	Mean {1-p} TAW=xp	Standard deviation	CV
30-Nov-06	334	21.95	131.7	56.45	25.6	45.35
09-Mar-07	68	78.4	294	183.8	63.1	34.33
03-Jul-07	184	5.02	67.31	23.04	15.35	66.62

18.2: Spatial variability of unready available water (x_p) estimated based on per image histogram.

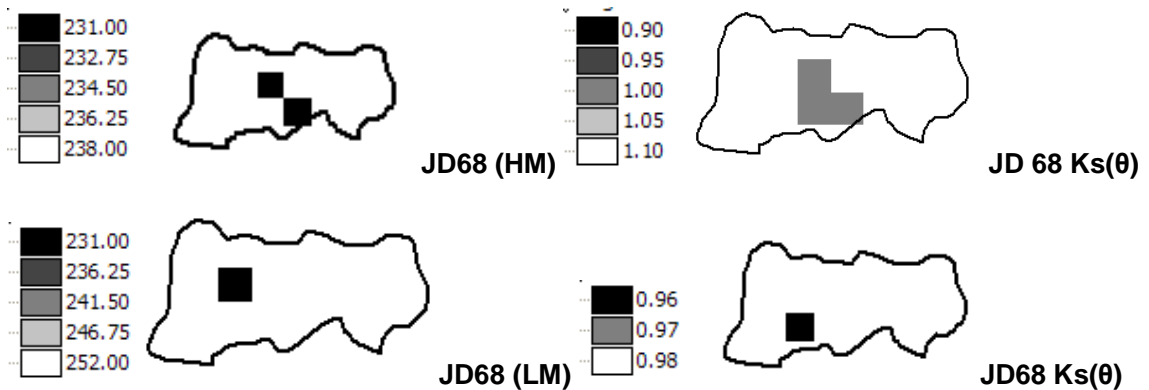
Date	JD	Min	Max	Mean $\{1-p\}$ TAW= x_p	Standard deviation	CV
30-Nov-06	334	-8.92	100.94	27.32	23.88	87.41
09-Mar-07	68	-22.3	271.36	124.57	79.32	63.68

18.3: Spatial variability of unready available water (x_p) estimated based on SSEBI Kc-NDVI model.

Estimated water held by soil matrix on JD 68 was generally high (mean=149 mm) and variable (CV=41%).

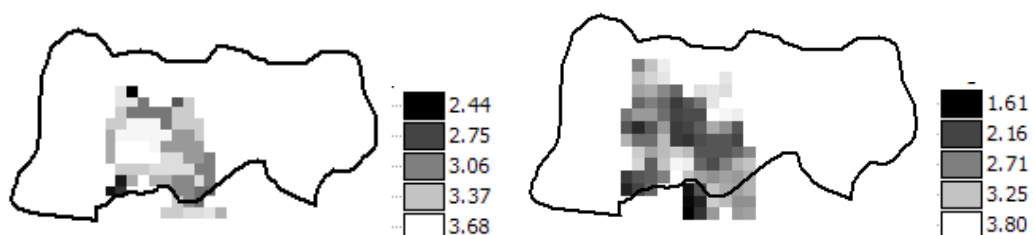
Observed spatial and temporal distribution of unready available soil water (x_p) may be attributed to weather condition that define the magnitude of crop evapotranspiration and but also variability of soil matrix potential which correspond to soil types with different soil water content. According to (Allen and Fao 1998), with high evapotranspiration associated with decreasing soil water content, water becomes more bound to the soil matrix and is more difficult to extract.

Appendix 19.1: Indicative binary maps of soil moisture status masked against threshold (fraction of TAW not readily available (x_p) (left) and corresponding soil moisture stress function, $K_s(x)$ (right); based on FAO 56 Kc-NDVI time series approach (Procedure 1). HM and LM refer to respectively high and low soil moisture status relative to the threshold.

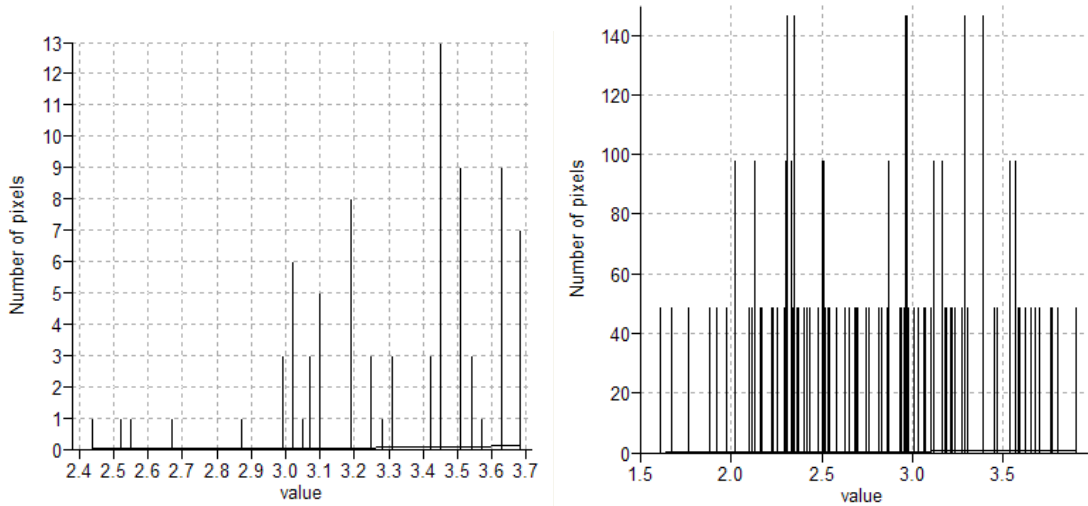


Appendix 19.2: Dissaggregation of ETc estimated by FAO 56 Kc-NDVI time series approach

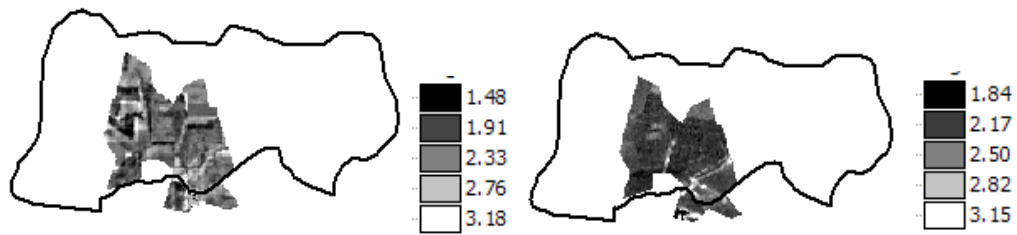
19.2.1: ETc estimates from MODIS (original) (left) and Aggregated Landsat TM (right) based FAO-56 Kc –NDVI time series approach, JD68.



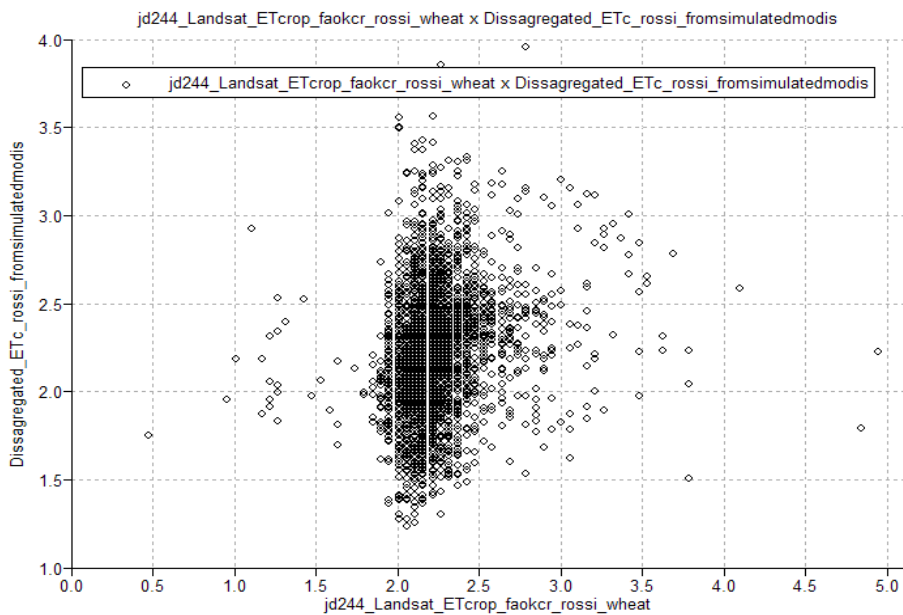
19.2.2: ET_c estimates based on FAO 56 Kc-NDVI time series, original MODIS (left) and aggregated Landsat TM –MODIS resolution-(right), JD 68.



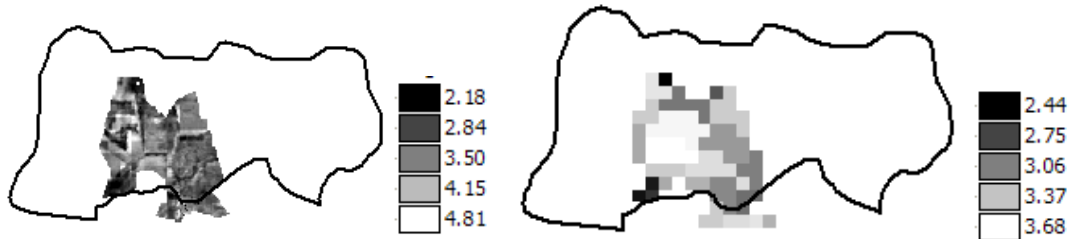
19.2.3: ET_c maps of JD 244 derived from FAO 56 Kc-NDVI time series approach: left is disaggregated (initially aggregated) and right is original Landsat TM ET_c map.



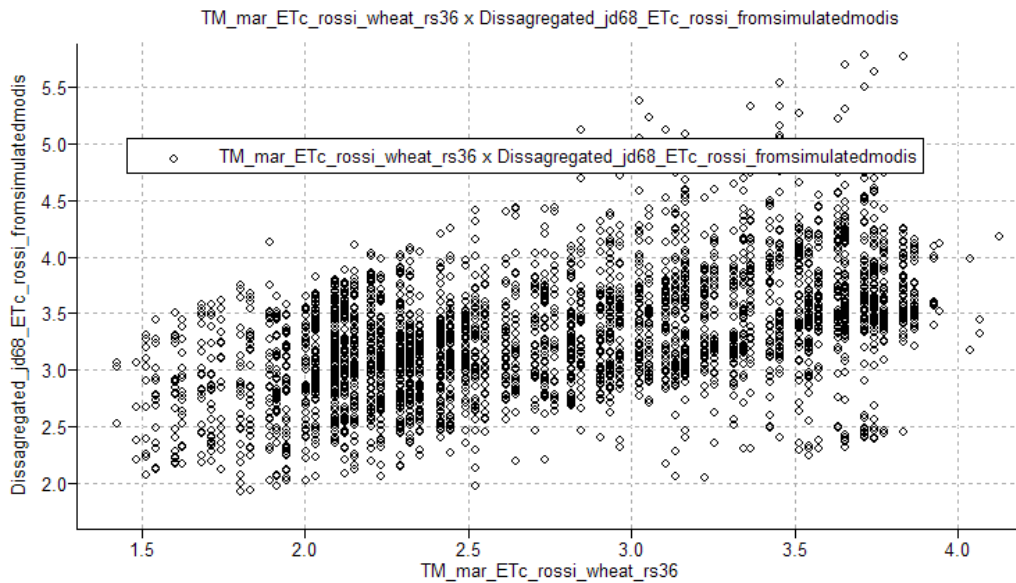
19.2.4: Scatter plot of ET_c derived from disaggregated Landsat TM (based on FAO 56 Kc-NDVI time series approach) and its corresponding original ET_c map, JD 244



19.2.5: MODIS ET_c estimates of JD 68 based on FAO 56 Kc-NDVI time series): left is disaggregated map (to Landsat TM 30 m resolution) and right is original MODIS ET_c.

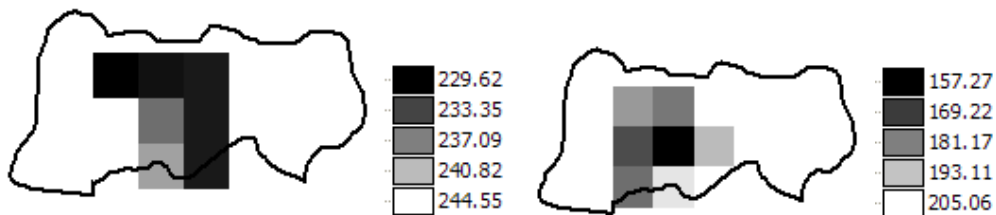


19.2.6: Scatter plot of ET_c derived from disaggregated MODIS (estimates based on FAO 56 Kc-NDVI time series) and its corresponding original Landsat TM ET_c map, JD 68



Appendix 20: Disaggregating depth-averaged soil moisture

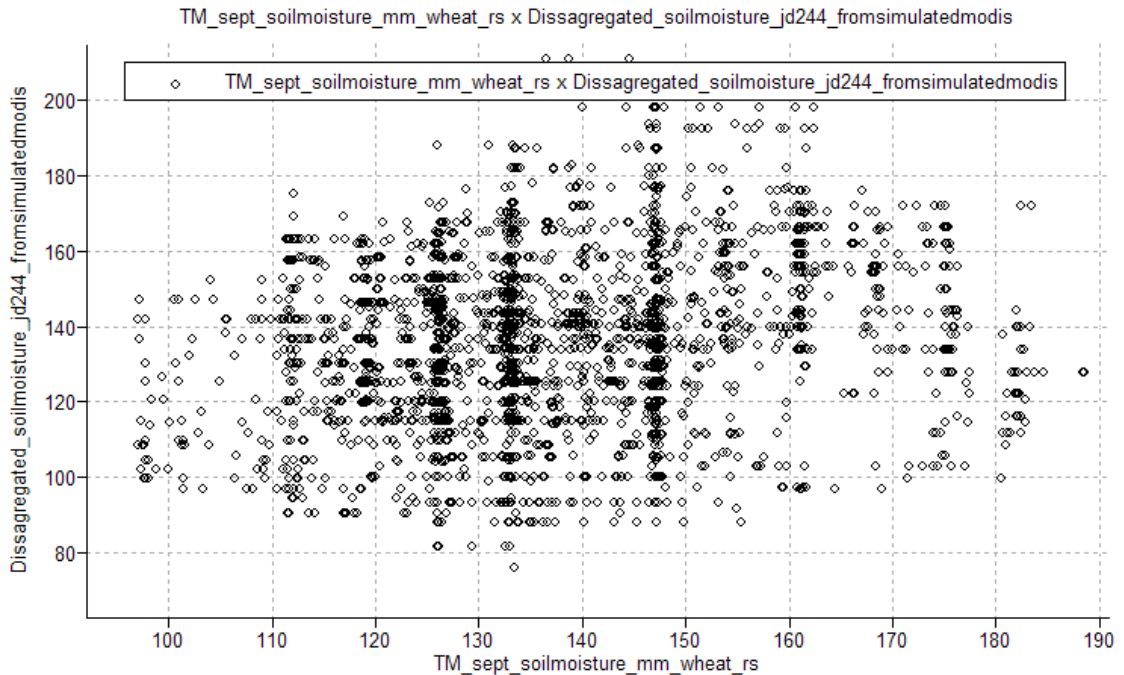
20.1: Comparison of estimates of soil moisture in the root zone derived from original MODIS (1000 m) (left) and aggregated (1000 m) Landsat TM (right).



From the maps, soil moisture estimates from MODIS were generally overestimated compared to estimates of (aggregated) Landsat TM, (mean=236.92 and 186.59 mm respectively), both in JD 68 and 244. Statistical comparison in terms of mean error/bias, MAB

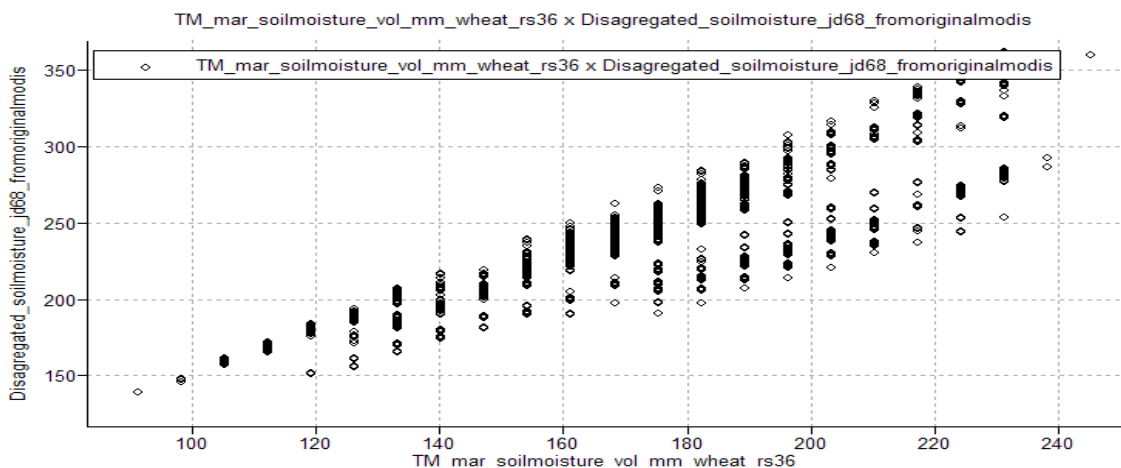
and RMSE showed a significant deviation between the two estimates, (-49.7 mm, 49.7 mm and 53.7 mm respectively for JD 68).

20.2: Evaluation of weighted ratio derived from Landsat TM estimates of depth-averaged soil moisture: Scatter plot of soil moisture derived from disaggregated Landsat TM of JD 244 (initially aggregated) and its corresponding original soil moisture map of JD 244.



Statistical comparison between the two (disaggregated Landsat TM of JD 244 (initially aggregated) and its corresponding original soil moisture map of JD 244) revealed minimal deviation, (ME/Bias=0.11, MAB=20.32, and RMSE=25.6mm), supporting good agreement between original and disaggregated Landsat TM estimates.

20.3: Evaluation of Dissaggregation of original MODIS estimate of depth-averaged soil moisture: Scatter plot of soil moisture derived from disaggregated MODIS against its corresponding original Landsat TM estimates, JD 68.



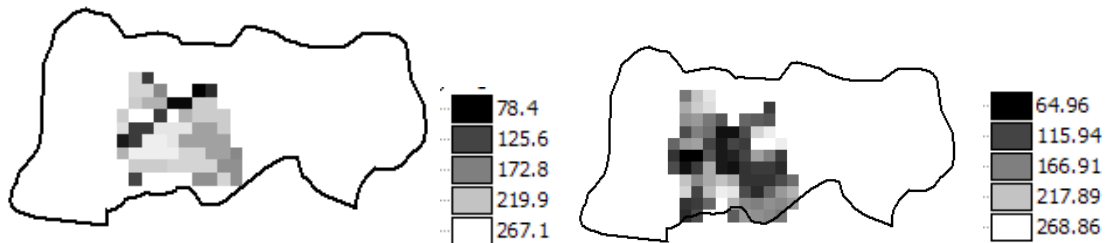
Scatter plot of disaggregated MODIS soil moisture estimate with corresponding original estimate of Landsat TM of JD 68 showed high correlation between the two. However, statistical comparison between the two revealed quite a big deviation, (ME/Bias=MAB=61 mm, and RMSE=65 mm).

20.4: Evaluation of spatial variability of depth-averaged soil moisture estimates for both original and disaggregated MODIS.

JD	ORIGINAL MODIS ETC			DISAGGREGATED MODIS ETC			Landsat TM		
	Mean	S	CV (%)	Mean	S	CV (%)	Mean	S	CV
334	186.7	10.7	5.73	186.29	33.27	17.9			
68	240.33	10.69	4.45	238.65	40.56	17.0	168	47.48	28.26
184	176.31	7.08	4.02	176.26	30.02	17.0			

Appendix 21: Disaggregating spatially distributed xp [unreadily available water (xp= (1-p)*TAW)]

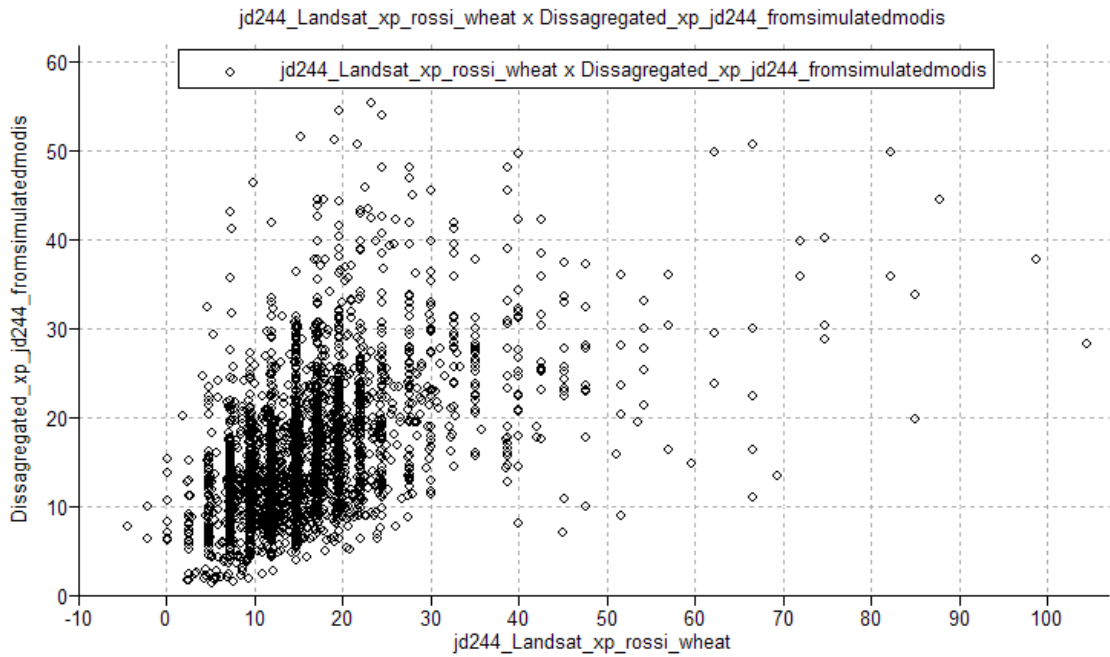
21.1: Comparison of estimates of unreadily available water (xp= (1-p)*TAW) derived from original MODIS (250 m) (left) and aggregated Landsat TM (250 m) (right), JD 68.



Estimates of spatial distribution of unreadily available water within the root zone (xp) in JD 68 and 244 apparently were quite different between the MODIS and aggregated Landsat TM. Generally, MODIS estimates were overestimated compared to (aggregated) Landsat TM, (mean=183.8 and 156.8 mm respectively in JD 68 and 63 and 17 mm respectively in JD 244).

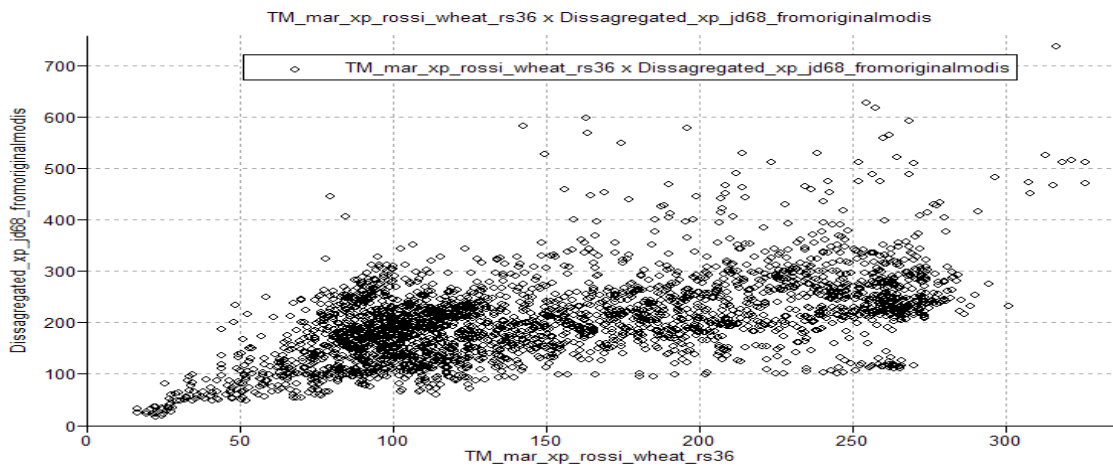
In JD 68, mean error/bias, MAB and RMSE showed a large inconsistency between the estimates of the two sensors, (-53.35 mm, 65.92 mm and 81.44 mm respectively) than in JD 244, (-46.6 mm, 46.6 mm and 48.8 mm respectively).

21.2: Evaluation of weighted ratio derived from Landsat TM estimates of xp (unreadily available water): Scatter plot of estimates of unreadily available water (xp) derived from disaggregated Landsat TM (initially aggregated) and its corresponding original Landsat TM map, JD 244



Statistical comparison between the two revealed marginal deviation, (ME/Bias=0.03, MAB=6.14, and RMSE=9 mm), supporting good agreement between original and disaggregated Landsat TM estimates.

21.3: Evaluation of Dissaggregation of original MODIS estimate of xp (unreadily available water): Scatter plot of estimates of unreadily available water (xp) derived from disaggregated MODIS against its corresponding original Landsat TM estimates, JD 68.



Statistical comparison between the two revealed quite a big deviation, (ME/Bias=55, MAB=67, and RMSE=91 mm).

21.4: Analysis of spatial variability of estimates of unready available water (xp) for both original and disaggregated MODIS.

JD	ORIGINAL MODIS xp			DISAGGREGATED MODIS xp			TM		
	Mean	S	CV (%)	Mean	S	CV (%)	Mean	S	CV
334	56.45	25.6	45.35	59.81	31.65	52.9			
68	183.8	63.1	34.33	208.93	83.27	39.9	146.21	71.98	49.23
184	23.04	15.35	66.62	24.46	16.42	67.1			

Appendix 22: Comparison of evapotranspiration (ET) estimates

MODELS/APPROACHES	DATE& Julian Day				
	30-Nov-06	09-Mar-07	03-Jul-07	09-Sep-07	Oct 06-Jul 07
	JD 334 (mm/day)	JD68 (mm/day)	JD184 (mm/day)	244_TM (mm/day)	Along temporal profile (mm/day)
FAO 56 Kc-NDVI time series approach vs S-SEBI Algorithm: ETC					
Bias or Mean Error (ME)	-0.15	1.08	1.32		
Mean Absolute Error	0.15	1.15	1.32		
RMSE	0.17	1.31	1.37		
FAO 56 Kc-NDVI time series approach vs S-SEBI Algorithm: ETa					
Bias or Mean Error (ME)		1.19			
Mean Absolute Error		1.19			
RMSE		1.34			
Per-image Histogram vs S-SEBI Algorithm					
Bias or Mean Error (ME)	-0.57	0.09	-0.96		
Mean Absolute Error	0.57	0.80	0.96		
RMSE	0.58	1.03	1.05		
S-SEBI Kc-NDVI model vs S-SEBI Algorithm					
Bias or Mean Error (ME)		0.1	1.07	-2.11	
Mean Absolute Error		0.53	1.07	2.48	
RMSE		0.69	1.11	1.08	
Phase-averaged SSEBI procedure vs S-SEBI Algorithm					
Bias or Mean Error (ME)					-0.39
Mean Absolute Error					0.76
RMSE					0.9
Traditional FAO-56 Traditional FAO-56 vs SSEBI ALGORITHM					
Bias or Mean Error (ME)					-0.02
Mean Absolute Error					1.09
RMSE					1.33

Appendix 23: Comparison of crop coefficient estimates

MODELS/APPROACHES	DATE/Julian Day				
	30-Nov-06	09-Mar-07	03-Jul-07	09-Sep-07	Oct 06-Jul 07
	JD 334	JD68	JD184	244_TM	Along temporal profile
FAO 56 Kc-NDVI time series approach vs S-SEBI Algorithm					
Bias or Mean Error (ME)	-0.07	0.37	0.18		
Mean Absolute Error	0.08	0.39	0.18		
RMSE	0.1	0.45	0.19		
Per-image Histogram vs S-SEBI Algorithm					
Bias or Mean Error (ME)	-0.28	0.03	-0.27		
Mean Absolute Error	0.28	0.28	0.27		
RMSE	0.36	0.36	0.28		
S-SEBI Kc-NDVI model vs S-SEBI Algorithm					
Bias or Mean Error (ME)		0.02	0.15	0.10	
Mean Absolute Error		0.18	0.15	0.19	
RMSE		0.23	0.15	0.24	
Phase-averaged SSEBI procedure vs S-SEBI Algorithm					
Bias or Mean Error (ME)					-0.19
Mean Absolute Error					0.37
RMSE					0.45
Traditional FAO-56 Traditional FAO-56 vs SSEBI ALGORITHM					
Bias or Mean Error (ME)					-0.13
Mean Absolute Error					0.39
RMSE					0.47

Appendix 24: Statistical analysis and elements of validation

Various statistical techniques were employed in the course of implementing the three approaches of estimating evapotranspiration. Comparison of the performance of processing formulae or alternatives was essential to allow decisions pertaining to the choice of one for subsequent processing. In some cases, graphical visualization gave tangible evidence of deviation. In other cases, differencing the two would yield measure of bias/ mean error to indicate the average deviation

Analysis of spatial distribution and temporal evolution of estimated were limited to selected zones over the study block (Fig.14), within which the disparity of the phenomenon under consideration would be spotted and changes tracked along time. Graphical illustrations of the temporal profile were used as well as comparative numerical description.

Detailed analysis of daily evapotranspiration and crop coefficient focused on a special selected zone (contiguous wheat area) shown in Fig. 9. In order to have a measure of

practical applicability of the model outputs, measures of central tendency (mean) and spread/dispersion/spatially variability (minimum, maximum, standard deviation and coefficient of variation (CV)) were determined. The larger the spread, the better the model in detecting spatial variability of crop water requirement. Particularly the standard deviation and CV (a dimensionless statistic), were used for comparing different kinds of measurements or to examine the amount of variation relative to the mean. CV does display clear trends that are directly related to measure of spatial variability relative to mean. In addition, CV was also used to relate the results of this study with results of other studies and variables.

$$CV = \frac{s}{MEAN} * 100 \quad 22.1$$

Three main statistical measures of fitness were employed including bias/mean error (ME); mean absolute bias (MAB) and root mean square (RMSE), (Er-Raki 2007). ME and MAB indicated the average deviation of the predicted values from the measured values. RMSE measures the variation of the predicted/modelled values around observed values. Low MAB and RMSE indicate good agreement between observed and modelled estimates. Measure of relative error (RE) was also evaluated. In the following expressions, $y_{i \text{ mod}}$ and $y_{i \text{ obs}}$ are individual values of modelled (option 1) and observed (option 2), respectively. The deviation was assumed negligible when the value of bias was low.

$$ME/BIAS = \frac{1}{N} \left[\sum_{i=1}^N (y_{i \text{ mod}} - y_{i \text{ obs}}) \right] \quad 22.2$$

$$MAE = \frac{1}{N} \left[\sum_{i=1}^N |y_{i \text{ mod}} - y_{i \text{ obs}}| \right] \quad 22.3$$

$$RMSE = \frac{1}{N} \sqrt{\sum_{i=1}^N (y_{i \text{ mod}} - y_{i \text{ obs}})^2} \quad 22.4$$

$$RE = \frac{y_{i \text{ mod}} - y_{i \text{ obs}}}{y_{i \text{ obs}}} * 100 \quad 22.5$$

Statistical expressions for evaluation of disaggregation procedure were formulated as:

$$BIAS/ME = \frac{1}{N} \left[\sum_{i=1}^N (TM5_{ORIGINALi} - TM5_{SIMULATEDi}) \right] \quad 22.6$$

$$MAE = \frac{1}{N} \left[\sum_{i=1}^N |TM5_{ORIGINALi} - TM5_{SIMULATEDi}| \right] \quad 22.7$$

$$RMSE = \sqrt{\frac{\sum_{i=1}^N (TM5_{ORIGINALi} - TM5_{SIMULATEDi})^2}{N}} \quad 22.8$$

$$RE = \frac{TM5_{ORIGINALi} - TM5_{SIMULATEDi}}{TM5_{ORIGINALi}} * 100 \quad 22.9$$

Appendix 25: Flow diagram of the disaggregation procedure using the weighted ET ratio approach, (Adapted from [35])

